Characterizing and Optimizing the TITAN facility from Energy Spread Determinations with a Retarding Energy Field Analyzer

Christian Champagne

Master of Science

Department of Physics

McGill University

Montreal, Quebec

November 9, 2009

A thesis submitted to McGill University in partial fulfillment of the requirements of the degree of Master of Science

ACKNOWLEDGEMENTS

Over the last three years, many people have assisted and supported my endeavor towards completing my Master's thesis. From the beginning, I would like to thank my trio of supervisors at McGill; Fritz Buchinger, John Crawford and Jonathan Lee for giving me the opportunity of pursuing my academic career in Physics, even if I barely saw them or kept them informed on my progress at TRIUMF.

On the other side of the country, I wouldn't be at TRIUMF if it wasn't for Jens Dilling, willing to accept me as one of his graduate students for the TITAN experiment. Even if I wasn't one of his best students, he still kept me in line and helped to motive me when I need it. Not far behind is Alain Lapierre, who taught me invaluable information about the inner workings of the EBIT and always kept an eye on my work.

Additionally, I would like to recognize Ryan Ringle, Thomas Brunner and Maxime Brodeur, not only for their inputs and numerous advices, but also to lighten up the atmosphere in the workplace everyday. My detector wouldn't have seen the light of day without the technical expertise and engineering knowledge of TITAN's technician and handyman Mel Good.

Many thanks go out to the numerous members of the TITAN group that I've spent quality time with during my stay at TRIUMF: Mathew Smith, Vladimir Ryjkov, Stephan Ettenauer, Paul Delheij, Michael Froese, Dave Lunney, Jochen Pfister, Mike Simon, Shavanna Shaw, Cecilia Leung, David Anderson, Erin O'Sullivan and Alexei Bylinskii.

Finally, thanks to my family in supporting me through all these years when I didn't call as much as you would have liked. I would also like to thank all my friends at the Varsity Outdoor Club at UBC for distracting me from my work when I should have been working.

ABSTRACT

The TITAN (TRIUMF's Ion Trap for Atomic and Nuclear science) experiment uses a Measurement Penning Trap (MPET) to perform high precision mass measurements ($\delta m/m \approx 10^{-8}$) on short-lived ($t_{1/2} \approx 10$ ms) isotopes. The ISAC (Isotope Separation and ACceleration) facility provides a 60 keV rare isotope beam to the experiments. A Radio-Frequency Quadrupole (RFQ) ion trap cools and bunches the incoming radioactive beam. An Electron Beam Ion Trap (EBIT) charge breeds the ions to a high charged state q. Since the MPET mass resolution is proportional to the charge state q, an improvement up to two orders of magnitude can be achieved. Further enhancements are obtained by the reduction of the uncertainty on the MPET measurements, such as from the ion bunch longitudinal kinetic energy spread. A Retarding Field energy Analyzer (RFA) was designed and constructed to measure this uncertainty.

An energy resolution $\Delta E/E \approx 10^{-3}$ was expected from to simulated RFQ ion extraction longitudinal energy spread measurements. An experimental energy resolution $\Delta E/E = 2.4 \times 10^{-3}$ was obtained. Suggestions to improve the energy resolution are provided.

Two testing sessions were undertaken using the RFQ and TITAN ion source to provide a singly charged pulsed ion beam. The first session used a ${}^{6}\mathrm{Li}^{+}$ beam with a 1 - 4 keV energy range. The RFA collimating slits were removed to insure the beam entered the RFA, increasing the energy resolution to $\Delta E/E = 5 \times 10^{-3}$. An energy resolution $\Delta E/E = (1.4 \pm 0.5) \times 10^{-2}$ was obtained from the longitudinal energy spread measurements as a function of the beam energy. No correlation between the RFQ buffer gas pressure and the longitudinal energy spread was observed.

The second session used ${}^{6,7}\mathrm{Li}$, ${}^{23}\mathrm{Na}$, ${}^{39,41}\mathrm{K}$ beams with a 1 - 5 keV energy range and the slits were reincorporated. A linear correlation with the RFQ extraction potentials magnitude is visible with both 2.5 keV ${}^{7}\mathrm{Li}^{+}$ and ${}^{23}\mathrm{Na}^{+}$ beams. No correlations between the RFQ buffer gas pressure, the space charge, beamgate size and beam composition with respect to the longitudinal

energy spread were otherwise found. Further reduction of the RFA energy resolution is necessary to resolve longitudinal energy spread variations under different RFQ parameter settings.

ABRÉGÉ

L'expérience TITAN (Piège ionique pour la science atomique et nucléaire de TRIUMF) utilise un piège Penning (MPET) pour effectuer des mesures de masse de haute précision ($\delta m/m \approx 10^{-8}$) sur des isotopes radioactifs de courte demi-vie ($t_{1/2} \approx 10$ ms). L'installation ISAC (Isotope Separation and Acceleration) à TRIUMF produit un 60 keV faisceau d'isotopes rares vers divers expériences. Un piège ionique quadrupôle linéaire à radio-fréquences (RFQ) refroidit et accumule le faisceau d'ions radioactifs. Un piège ionique à faisceau d'électrons (EBIT) augmente la charge ionique des ions simplement chargés à une haute charge q. Puisque la résolution de masse de MPET est proportionnelle à la charge ionique q, une augmentation de la résolution jusqu'à deux ordres de grandeur est possible. Des améliorations additionnelles sont fait par la réduction des sources d'erreurs sur les mesures du MPET, comme la dispersion longitudinale de l'énergie cinétique des ions pulsés. Un analyseur d'énergie cinétique á champ retardé (RFA) fut conųu et construit dans le but de mesurer cette erreur.

Une résolution énergétique $\Delta E/E < 10^{-3}$ fut visée à la suite des résultats obtenus de simulations numériques de l'extraction d'ions du RFQ. Une résolution énergétique expérimentale $\Delta E/E = 2.4 \times 10^{-3}$ a été obtenue. Des suggestions pour améliorer la résolution énergétique sont données.

Le RFA fut testé au cours de deux séances en utilisant le RFQ et la source d'ions de TITAN pour fournir un faisceau d'ions simplement chargés. Durant la première séance, un faisceau de $^{6}\mathrm{Li}^{+}$ avec énergies entre 1 et 4 keV fut utilisé. Les fentes du collimateur furent enlevées pour assurer que le faisceau pénètre dans le RFA, augmentant la résolution énergétique à $\Delta E/E = 5 \times 10^{-3}$. Une résolution énergétique $\Delta E/E = (1.4 \pm 0.5) \times 10^{-2}$ a été obtenue de la relation entre la dispersion longitudinale de l'énergie cinétique et de l'énergie cinétique du faisceau. Aucune corrélation entre la pression du gaz tampon du RFQ et la dispersion longitudinale de l'énergie cinétique a été observée.

La seconde séance utilisait des faisceaux de ^{6,7}Li, ^{23}Na, ^{39,41} K avec des énergies cinétiques entre 1 et 5 keV et les fentes du collimateur furent ré-incorporées. Une corrélation linéaire avec la grandeur des potentiels extraction du RFQ fut observée avec les deux faisceaux de ^{7}Li^{+} et ^{23}Na^{+} à 2.5 keV utilisés. Aucune corrélation entre la charge spatiale, pression du gaz tampon du RFQ, la durée du barrière d'ions et la composition du faisceau avec la dispersion longitudinale de l'énergie cinétique furent autrement notées. Des réduction supplémentaires à la résolution énergétique du RFA sont nécessaire pour observer des variations dans la dispersion longitudinale de l'énergie cinétique du faisceau sous différent paramètres du RFQ.

TABLE OF CONTENTS

LIST OF TABLES

LIST OF FIGURES

CHAPTER 1
Motivation for High Precision Mass Measurement

The TITAN (TRIUMF's Ion Trap for Atomic and Nuclear science) Experiment at TRIUMF (TRI-University Meson Facility) uses a Penning Trap mass spectrometer to determine the mass of unstable isotopes. In order to achieve high precision mass measurement ($\delta m/m \approx 10^{-8}$) of short-lived ($t_{1/2} = 10\,ms$) radio-isotopes, the ions charged state is boosted by an Electron Beam Ion Trap (EBIT). A Retarding Field energy Analyzer (RFA) was designed, constructed and used to measure the longitudinal energy spread of the extracted ion bunches from the EBIT and the Radio-Frequency Quadrupole (RFQ) ion trap. The RFA will be used to optimize both the EBIT and the RFQ by determining and minimizing the energy spread of the extracted ion bunches. This, in turn, will allow to reduce the uncertainty in the mass measurements performed with the Penning Trap.

The first chapter of this thesis motivates high precision mass measurements. An overview of nuclear and mass models, stellar nucleosynthesis and weak interactions studies to test the Standard Model is viewed. Chapter two covers the layout and each component of the TITAN experiment and the relevance of knowing the energy spread in high precision mass measurements. In chapter three, various experimental methods to measure the energy spread of an ion beam are presented and weighed against each other. Chapter four presents the theoretical principle of an RFA. The limitation in the energy resolution of the device and methods of improving it are explored. In chapter five, the TITAN RFA design, construction and properties are presented. Using theoretical predictions to determine the RFA energy resolution, a set of fundamental design requirements are given and further developments are based for optimal application within the TITAN beamlime. Chapter six covers the experimental setup used during two series of test measurements with the TITAN ion source and RFQ. The electronic components and data acquisition software are reviewed. Chapter seven shows measurements performed during the two series and presents the data analysis. The final chapter gives a summary and outlook of this study.

High precision mass spectroscopy has spurred many contributions in the fields of nuclear and particle physics. With the newly constructed TITAN experiment now online, significant advancements are expected in the near future in the following fields [6]:

- Nuclear theory and mass models far away from the valley of stability
- Halo Nuclei
- Changes in the locations of nucleon numbers
- Stellar processes and element nucleosynthesis
- Weak interaction studies in the Standard Model

These examples will be expanded in detail in the following chapter.

1.1 Nuclear Physics

The binding energy of nucleons within a nucleus constitutes an important property in the field of nuclear physics. Discoveries such as the existence of nuclear shell closures and the non-spherical shape of the nuclei where first uncovered using this property [7]. The nucleus binding energy $B(N,Z)$ is the mass difference between its mass $M(N,Z)$ and of the individual Z protons and N neutrons composing it [7].

$$B(N,Z) = (Nm_n + Zm_Z - M(N,Z))\,c^2 \tag{1.1}$$

Observations of significant differences in binding energy between adjoining nuclei can point towards new phenomena within the nuclei structure, as mentioned above [8]. For instance, nuclear shell closures are observed by measuring the two-neutron separation energy S_{2n} [7].

$$S_{2n}(N,Z) = (B(N,Z) - B(N-2,Z)) \tag{1.2}$$

where the shell closures appears as a sharp drop in S_{2n} as a function of N, independently of Z. Such transition are easily seen at $N = 2, 8, 20, 28, 50, 82, 126$ and are known as the magic numbers [7]. An identical trend is also seen with the two-proton separation energy S_{2p}. In addition, shell deformations from the typical nucleus spherical shape, to either a prolate or oblate shape, can be observed by sudden changes in S_{2n} along a series of N and limited within a few Z [9], as shown in Figure 1–1. These distortions become more prominent in the mass ranges $150 < A < 190$ and $A > 220$ [7].

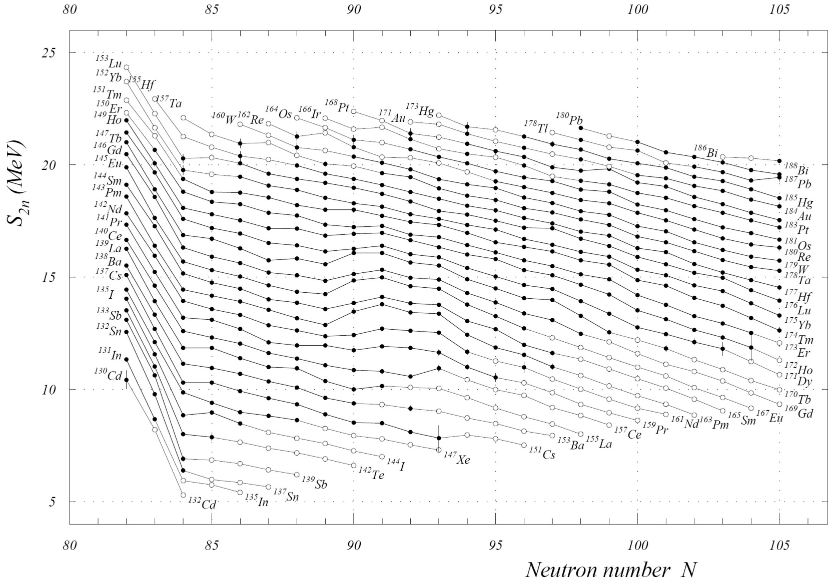

Figure 1–1: Two-neutron separation energy S_{2n} for various elements between $N = 82 - 105$. Notice the shell closure along $N = 82$ and shell deformations bounded by $N = 89 - 94$ and by ^{172}Ho and ^{157}Ce. Taken from [10]

One particularity of the binding energy is its quasi-constant value per nucleon ($B/A \sim 8$ MeV) along most of the periodic table ($20 \lesssim A \lesssim 250$). From this property, the maximum mass measurement resolution required to observed the effect of the binding energy is $\delta m/m \approx 10^{-5}$.

Using the law of conservation of total energy, the nuclear reaction energetics can be measured as the mass difference between the initial m_i and final m_f nucleus mass energy

$$Q = (m_i - m_f)\, c^2 \tag{1.3}$$

where Q is known as the Q-value [7]. This value has great importance in the weak interaction reaction rate, as it will be shown in section 1.2.1.

1.1.1 Nuclear Mass Models & Formulas

High precision mass measurements are currently able to resolve mass differences down to the 10^{-8} level. This level of precision allows for the fine-tuning of a number of nuclear masses models. However, when applying these models far away from the valley of stability, a region of stable nuclear species along the chart of elements (see Figure 1–4) with unstable species forming the valley 'walls' who posses either an overabundance of protons or neutrons, they diverge from experimental data and from each other (see Figure 1–2). Since both types of nuclei usually posses a short lifetime and exist only in minute amounts, the ability of producing statistically significant quantities is necessary to improve the nuclear models in these two regions. Radioactive ion beams facilities are able to provide short-lived nuclei approaching the drip lines.

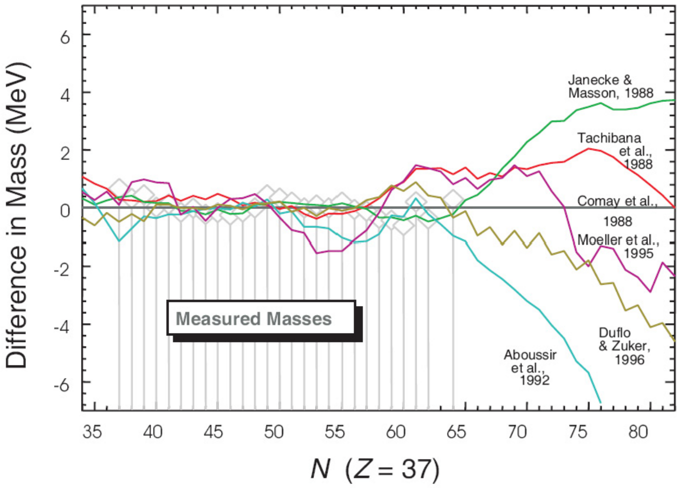

Figure 1–2: Mass difference between various theoretical models and experimental mass data obtained for rubidium isotopes. A modified ensemble averaging of the mass predictions from the theoretical models is used as the baseline [1]. Below N = 64, the models are in good agreement with the experimental masses whereas for N > 64, the models begin to diverge. Taken from [11]

A particular area of recent interest within the drip line regions is the study of halo nuclei [12], an atomic nucleus that has one or few extremely weakly bounded nucleons resulting in a nuclear radius appreciably larger than predicted from the mean nuclear radius R (Equation 1.4), derived from the near constant central nuclear density seen in all stable nuclei [7].

$$R = R_0 A^{1/3} \tag{1.4}$$

Here $R_0 = 1.2$ fm is a proportionality constant and A is the nuclei mass number (total number of nucleons).

A few well documented halo nuclei are ^{11}Li [11] (see Figure 1–3) and ^{11}Be [13] (see Figure 1–3), ^{6}He [14], ^{14}Be [15] and ^{8}He [16], with additional nuclei currently under investigation [17]. The binding energy of the outermost nucleons in these systems are typically below 1 MeV, compared to the usual 6-8 MeV for stable nuclei [17] due to a secondary effect of the Pauli exclusion principle, prohibiting fermions such as proton and neutrons from occupying an identical quantum state within a nucleus [18]. To illustrate this effect, consider a nucleus with a fixed number of protons. As neutrons are added to the nucleus, they occupy distinct energy levels defined by quantum mechanics. Due to the Pauli exclusion principle, the number of neutrons allowed for each level is limited by the quantum states available there. If a level is filled, subsequent neutrons are forced to occupy the next higher energy level, requiring more energy in the process and lowering the binding energy of these neutrons. No more neutrons can be added when the binding energy cannot compensate anymore for the raising energy levels. The same principle applies to protons for a fixed neutron number. A mass resolution of below $\delta m/m \approx 10^{-7}$ is required to observe these differences in the binding energy.

1.1.2 Stellar Processes & Element Nucleosynthesis

The field of nuclear astrophysics requires mass measurements of short-lived nuclei. The creation of all elements heavier that A $\geq$ 7 takes place in stars by nuclear reactions. Some of these reactions occur along a series of complex chains, named *s*- (slow neutron), *p*- (gamma) [19], *r*- (rapid neutron) and *rp*- (rapid proton) processes [20] as partly shown in Figure 1–4. In general, all nuclei masses are important in determining the reaction rates involved in these processes but a few crucial nuclei contribute significantly more than others. These include nuclei with closed neutron shells and proton-rich nuclei which contribute in *r*- and *p*-processes in supernovae respectively and nuclei near the $N = Z$ waiting points used for *rp*-process calculations

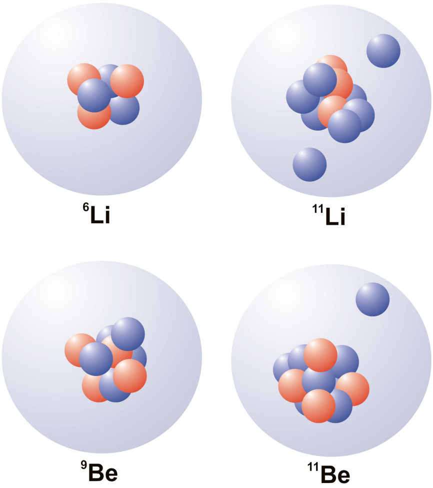

Figure 1–3: Top: A stable ^{6}Li nucleus (left) and a two-neutron ^{11}Li halo (right), consisting of a ^{9}Li-like core and two weakly bound neutrons. Bottom: A stable ^{9}Be nucleus (left) and an one-neutron ^{11}Be halo (right), consisting of a ^{10}Be-like core and a weakly bound neutron.

in X-ray bursts, a sudden and powerful surge of X-rays originating from a binary star system composed of a compact object (such as a white dwarf or neutron star) and a normal star, are of great interest [20]. More often, these chains lie on the fringes of either the neutron or proton drip lines.

1.2 Particle Physics

1.2.1 Weak Interaction Studies as a Test of the Standard Model

In particle physics, the Standard Model is currently the most successful model describing the interaction between fundamental particles. Experiments are performed with increasing precision and complexity to uncover the slight discrepancies within the model. If such a disagreement would be discovered, the possibility of new physics beyond the Standard Model would arise. One such test is the predicted unitary of the Cabibbo-Kobayashi-Maskawa (CKM) quark-mixing matrix which couples the strong and weak quark eigenstates, enabling quark decay from one family into a quark of a second family through the weak interaction [22, 23]:

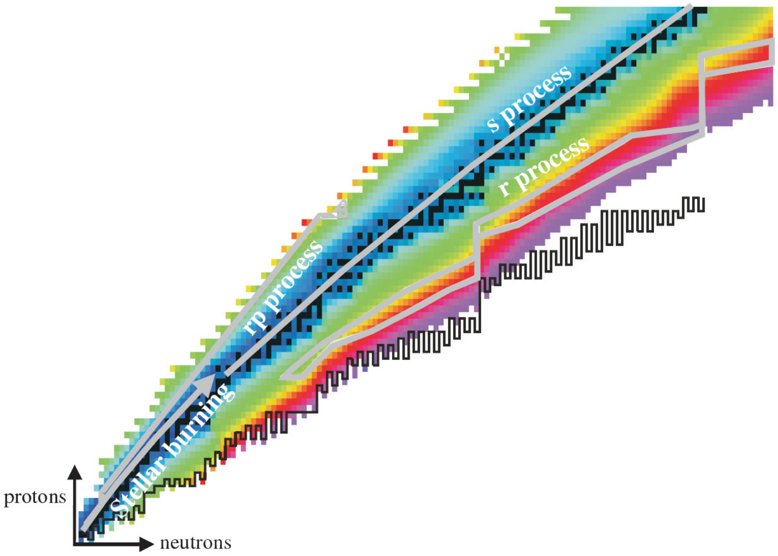

Figure 1–4: The chart of elements with paths of the different stellar processes (rp, s and r). Taken from [21].

$$\begin{pmatrix} d_w \\ s_w \\ b_w \end{pmatrix} = \begin{pmatrix} V_{ud} & V_{us} & V_{ub} \\ V_{cd} & V_{cs} & V_{cb} \\ V_{td} & V_{ts} & V_{tb} \end{pmatrix} \begin{pmatrix} d_s \\ s_s \\ b_s \end{pmatrix}$$

where V_{ij}^2 represents the transition probability from an i quark to a j quark. In the Standard Model, the CKM matrix must be an unitary matrix, with the property that the elements squared sum of any given row or column must be equal to unity.

$$\sum_j V_{ij}^2 = V_{i1}^2 + V_{i2}^2 + V_{i3}^2 = 1. \tag{1.5}$$

The physical interpretation for this property can be understood as the sum of all probabilities of one quark to decay into some other quark must add up to one. By measuring each element along one row or column, it is possible to determine if the CKM matrix unitary is violated. Until very recently [24], the latest experimental data for elements along the top row, $V_{ud} = 0.9738 \pm 0.0005$, $V_{us} = 0.2200 \pm 0.0026$ and $V_{ub} = 0.0037 \pm 0.0005$ yielded a non-unitary squared sum $\sum_i V_{ui}^2 = 0.9967 \pm 0.0014$, deviating from unity by more than two standard deviations [25]. The values of V_{ud}, V_{us} and V_{ub} are obtained from nuclear beta, Kaon and B meson decays respectively. Comparing the magnitude of these elements, V_{ud} and V_{us} weigh more in the uncertainty of the sum than does V_{ub}. Even though the error on V_{ud} is approximately five times smaller that the error on V_{us}, its reciprocal fivefold larger value results in an equivalent error magnitude of the squared values V_{ud}^2 and V_{us}^2. Whereas the uncertainty in both values could explain the deviation from unity, the uncertainty of V_{ud} can be reduce using high precision mass measurements.

The element V_{ud} can be measured from studies of super-allowed $0^+ \rightarrow 0^+$ β-decay. From Fermi's theory of β-decay, it is shown that the half-life of any element decaying through the weak force can be expressed as [7]

$$ft = \frac{K}{g^2|M_{if}|^2} \tag{1.6}$$

where f is the dimensionless Fermi integral, t is the decay half-life, K is a numeric constant, g is the weak coupling constant and M_{if} is the matrix element of the overlap between the initial and final nuclear wavefunctions. The comparative half-life or ft-value can be obtained by measurements of the Q-value of the decay, the branching ratio (ratio between individual decay rates of a specific mode and the total decay rate) and the lifetime of the nuclei under observation.

In the case of superallowed $0^+ \rightarrow 0^+$ β-decays and between isospin $T = 1$ analog states, the transitions are pure Fermi decays; the axial vector contribution to the matrix element M_{if} vanishes, leaving only pure vector interactions. As consequence, the overlap between the wavefunctions is assumed to be perfect, resulting in that the matrix element $|M_{if}|$ can be reduced to $\sqrt{2}$ and that only the vector component of the weak coupling constant G_V contributes. In addition, the Conserved Vector Current (CVC) hypothesis, which assumes no influence between the vector part of the strong and weak interactions, predicts that G_V should remain constant, regardlessly of the element chosen [26]. As such, Equation 1.6 can be simplified to

$$ft = \frac{K}{2G_V^2} = constant \tag{1.7}$$

In practice, slight corrections are added to the ft-value since the theory does not take into account some electromagnetic and nuclear interactions. Such examples include radiative corrections from an undetected emission of a bremsstrahlung photon from the outgoing electron or the non-symmetry of the nuclei [27], resulting in a slight reduced nuclear matrix element M_{if}.

$$|M_{if}|^2 = |M_0|^2(1 - \delta_C) \tag{1.8}$$

where M_0 is the symmetric nuclear matrix component, which is equal to $\sqrt{2}$ and δ_C is the isospin-symmetry-breaking correction. These corrections will define a new "corrected" comparative half-life, Ft-value, which is expressed as [26]

$$Ft = ft(1 + \delta_R)(1 - \delta_C) = \frac{K}{2G_V^2(1 + \Delta_R^v)} = \text{constant} \tag{1.9}$$

where δ_R and Δ_R^v are respectively the radiative correction nucleus-dependent and nucleus-independent parts.

The CVC hypothesis validity can be verified by comparing the different β-decays Ft-values. The average corrected $\overline{Ft}$-values for the 13 best known super-allowed decays (see Figure 1–5) has been calculated as [27]

$$\overline{Ft} = 3071.4 \pm 0.8\, s \tag{1.10}$$

The CVC hypothesis is valid down to the 3×10^{-4} level. The value of V_{ud} is obtained from the ratio between G_V and the Fermi coupling constant G_F measured from purely leptonic muon decays [28]. Re-arranging Equation (1.9), V_{ud} can be expressed as a function of $\overline{Ft}$-value

$$V_{ud}^2 = \frac{K}{2G_F^2(1 + \Delta_R^v)\overline{Ft}}, \tag{1.11}$$

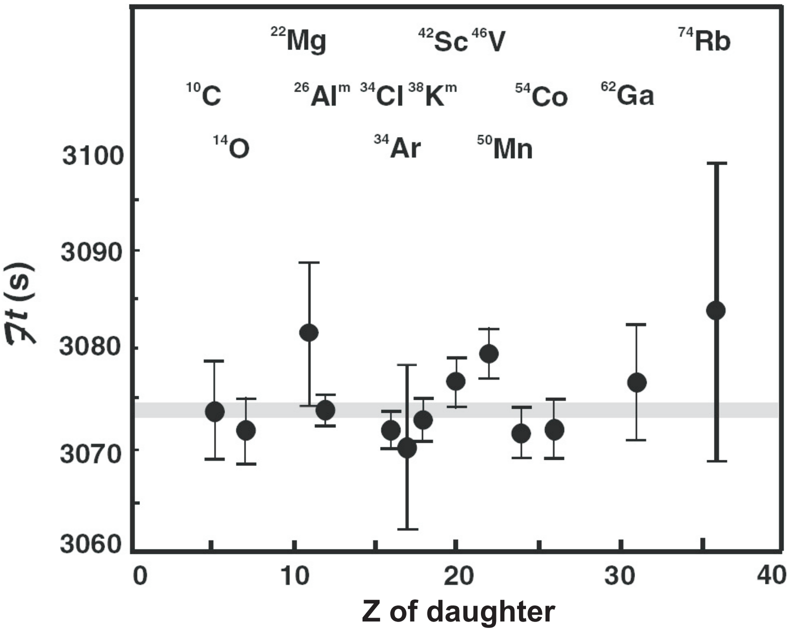

Figure 1–5: Ft values for the 13 best known superallowed transitions. The average $\overline{Ft}$ value is shown as a horizontal grey band with its uncertainty. Taken from [27]

The precision of the value of V_{ud} can directly be linked to high precision mass measurement by the calculation of the Fermi integral f, which depends of the Q-value to the 5^{th} power [26]. Since the Ft-value uncertainty is of the order of 10^{-3}, this places an upper limit on the Q-value uncertainty measurements at 0.02 %. By considering the average mass of the 13 most precise measured super-allowed $0^+ \rightarrow 0^+$ β-decays to be $A \sim 40$ u, the minimum precision of their masses will need to be $\delta m/m \approx 10^{-8}$.

More recently, Q-value measurement of ^{46}V performed by the Canadian Penning Trap [29] showed a Ft-value more that two standard deviations away from the average value of the previous 12 most well-known Ft-values [30]. In light of this, a complete reevaluation of the isospin-symmetry breaking corrections of all Ft-values obtained for superallowed $0^+ \rightarrow 0^+$ β decay was performed [27]. A discrepancy varying from 0.03% for elements $A \leq 38$ up to 0.3% for heavier elements was noted. After incorporating these newly corrected values, the Ft-value of ^{46}V was within a standard deviation of the average $\overline{Ft}$ value (see Equation 1.10). The updated value for V_{ud} was then

$$V_{ud} = 0.97418 \pm 0.00026 \tag{1.12}$$

and in combination with V_{us} and V_{ub} values from the 2006 Particle Data Group review [28], the CKM matrix top row squared sum is then

$$|V_{ud}|^2 + |V_{us}|^2 + |V_{ub}|^2 = 1.0000 \pm 0.0011 \tag{1.13}$$

1.3 Summary

Even though one of the TITAN's initial experimental goals, solving the CKM matrix unitary problem, seems to have be resolved before its commissioning, it is expected that the TITAN experiment will still deliver new insights into the field of nuclear physics, with emphasis on the underlining nuclear structure of halo nuclei and further improvements on high precision mass measurements of short-lived isotopes. A detailed overview of the TITAN experiment is described in Chapter 2.

CHAPTER 2
TITAN Experiment

The TITAN (TRIUMF's Ion Trap for Atomic and Nuclear science) experiment at TRIUMF is an ion trap experiment designed for high precision mass measurements $\delta m/m \approx 10^{-8}$ on short-lived $t_{1/2} \approx 10$ ms radio-isotopes [31]. The experiment currently consists of three interlinked ion traps; a Radio-Frequency Quadrupole (RFQ) ion trap, an Electron Beam Ion Trap (EBIT) and an Measurement Penning Trap (MPET) [6]. A fourth trap, a Cooler Penning Trap (CPT) will be added in the near future. To achieve the high level of precision in the ion mass determination, TITAN utilizes an EBIT to increase the ions charged state. The highly charged ions (HCI) mass is measured with the MPET. The ion mass inside a Penning trap can be derived from its cyclotron frequency ω_c [32]:

$$m = \frac{qB}{\omega_c} \tag{2.1}$$

where B is the Penning trap's magnetic field strength, q and m are the ion's charge and mass respectively. The mass measurement uncertainty can be derived as [6]:

$$\frac{\delta m}{m} \approx \frac{m}{TqB\sqrt{N}} \tag{2.2}$$

where N is the number of mass measurements and T is the excitation time in the Penning trap.

From Equation (2.2), the uncertainty is inversely proportional to T, B, q and $\sqrt{N}$. Since T is limited in the age of radioactive ions by their half-life and B cannot be significantly increased beyond 10T due to technical difficulties, the mass uncertainty can be greatly reduced by increasing the ion's charge. By utilizing HCI produced by the EBIT, the TITAN experiment mass measurement resolution can be increased by almost two order of magnitude [33], as for example, He-like Francium (Fr^{85+}) (see Figure 2–1). In combination with the wide range of short-lived isotopes provided by the ISAC facility at TRIUMF, the TITAN experiment will reach new levels of high precision mass measurements. This chapter will cover the TITAN experiment, its components at the ISAC facility and the motivation for the use of an RFA for TITAN.

2.1 Overview of the TITAN Experiment

The TITAN experiment is composed of four main components:

- Radio-Frequency Quadrupole (RFQ) ion trap for capturing, bunching and cooling the continuous ISAC ion beam.
- Electron Beam Ion Trap (EBIT) for charge breeding the ions from the RFQ
- Cooler Penning Trap (CPT) for cooling the ions extracted from the EBIT
- Measurement Penning Trap (MPET) for performing high precision mass measurement.

A schematic view of the TITAN platform with the listed components can be seen in Figure 2–2. A step-by-step description of each component during the flight path taken by the ions from its creation in the ISAC facility to the final measurements with the MPET is given in this chapter.

2.2 ISAC Facility

Since 1998, the Isotope Separator ACcelerator (ISAC) facility at TRIUMF produces radioactive ion beams by using the Isotope Separation OnLine (ISOL) technique. An intense 500 MeV proton beam with $\sim 100\,\mu A$ from the TRIUMF cyclotron bombards one of two thick ($\lesssim$ 20 g / cm^2) production targets, creating a wide variety of isotopes by fission, spallation or fragmentation reactions. By maintaining a high temperature on the targets, the created short-lived isotopes diffuse out of the target and can be ionized by an ion source [34]. The extracted ions are then funnelled into a continuous beam and mass analyzed using a tandem of mass separators with a total resolving power of $R \sim 3,000$. The mass separated beam is then directed into the ISAC experiment hall and from there, to the various experiments (see Figure 2–3).

Some experiments, such as DRAGON [35] and TUDA [36], require a more energetic ion beam than the 2 keV/u initially supplied from the ion source [34]. The nuclear radioactive beam can be post-accelerated up to 1.5 MeV/u for ions with A/q $\leq$ 30 using in series a RFQ linear accelerator (LINAC) and a drift-tube linear accelerator (DTL). Recently, the ISAC-II extension was build [37] with a super-conducting LINAC to further boost the beam energy to $\gtrsim 6.5$ MeV/u for ions with $A/q \leq 150$, which the EMMA [38] and TIGRESS [39] experiments will be using.

2.3 Radio-Frequency Quadrupole Trap

The ISAC facility produces a continuous radioactive ion beam with a kinetic energy between 30-60 keV and a maximum transverse emittance of $\varepsilon_{99\%} = 50\pi \, mm \, mrad$ [40] before post-acceleration with the LINAC and DTL. To perform high precision mass measurements with the MPET and, in particular, to achieve a good transmission efficiency into the EBIT or MPET, a pulsed ion beam of low energy spread and emittance is required. In addition, the beam emittance must be reduce to match the EBIT and MPET acceptances. The TITAN RFQ role is to receive the ISAC beam, decelerate, cool and bunch the ions for the use of the EBIT and MPET.

The ISAC beam is electrostatically decelerated by a series of biased electrodes to an energy $\sim$ 10-40 eV before entering the RFQ. The ions are centred by RF fields and then interactions with a buffer gas leads to ion cooling. For effective cooling, the interaction time between the ion and the bath must be sufficient long for the ions to reach a thermal equilibrium. In most situations, the thermal bath will be composed of helium gas as an inert noble gas. This property minimizes chemical reactivity and diffusion of the incoming ion beam. Computational simulations were perform [41] to determine the RFQ optimal interaction length, cooling process, injection and extraction optics.

The RFQ employs four equally spaced semi-cylindrical electrodes with squared-rf oscillations to radially focus the beam along the RFQ length (see Figure 2–4). To transform the continuous ISAC beam into a pulsed beam, the electrodes are segmented lengthwise with decreasing stepwise applied potentials, cumulating with a high potential at the end. This creates a three dimensional trap (see Figure 2–5) and allows to accumulate the ions in the potential minimum. The RFQ structure is floated to the beam potential V_{DC} to facilitate ion capture (see Figure 2–4). The bunched ions are extracted by lowering the trapping potentials on the last electrodes. After subsequently passing through the RFQ extraction optics, the well-defined bunched ion beam enters a drift tube, which is switched from a matching potential down to a pre-defined voltage

V_{drift}. The cooled pulsed ion beam is guided towards the MPET or EBIT with a potential energy V_{drift}, typically set between 1 - 2 keV.

2.4 Electron Beam Ion Trap

The TITAN Electron Beam Ion Trap (EBIT) is used to increase the singly charged ions from the RFQ to a higher charged state [43]. The EBIT uses a series of drift tubes in a longitudinal potential well configuration to capture and trap the ions. A 6 T magnetic field produced by a pair of superconducting Helmholtz coils confines the ions in the radial direction (see Figure 2–6). Charge breeding is accomplished with an electron beam projected along the trap center in the axial direction, resulting in a stepwise ionization of the trapped ions to higher charge states.

The ions' final charged state is limited by the electron beam kinetic energy, as the ionization energy increases as progressively deeper bound electrons are removed and by recombination from charge exchanges between HCI, neutral background gas or free electrons. The TITAN EBIT design allows electron beam energies up to 60 keV, sufficient to produce He-like Uranium.

During the collisional process between the electron beam and the trapped ions, part of the electron beam kinetic energy is converted into thermal motion of the ions and increasing its axial energy. Moreover, the e-beam space charge potential can be filled with the HCI, which leads to a rather large energy uncertainty for the extracted beam. To prevent HCI from eventually gaining sufficient axial energy to overcome the longitudinal potential well barrier and escape, evaporative cooling is employed (see Figure 2–7) [44]. The HCI are cooled by injecting a steady stream of atoms with a mass and proton number Z lower than the HCI via a side-port in the trap. As the cooling atoms enters the trap, they are quickly ionized by the electron beam and by charge exchange with HCI. These cooling ions will reach a lower charge states than the HCI and will not be as tightly bound since the trapping is directly proportional to the charge state q. As such, the cooling ions will have a larger escape rate than the HCI and will export with them some thermal energy from the HCI due to Coulomb interactions, effectively cooling the HCI [45]. A constant replenishing of the cooling gas is done to offset the continual lost from the trap. Once the desired charge state is attained, the HCI are extracted from the EBIT by changing the applied potentials to the trap's drift tubes and subsequently guided back into the TITAN beamline and towards the CPT/MPET.

2.5 Cooler Penning Trap

As the HCI are extracted from the EBIT, they will have a significantly large energy spread $\Delta E \approx 10$ eV/q due to the constant thermal heating from the electron beam [46]. This spread will limit the attainable resolution of the mass measurements performed with the MPET. A cooled pulsed ion beam with low energy spread (≤ 1 eV/q) is generally required to perform high precision mass measurements at the 10^{-8} level [6]. The HCI will need to be cooled down further before they can be injected into the MPET.

The use of a neutral gas thermal bath, as seen in the RFQ, cannot be used due to the large charge exchange cross-section between the HCI and the gas. Along similar lines, using electrons as a cooling agent has been investigated and performed [47]. However, this method is limited to HCI with energies higher that 100 eV/q due to the high recombination rate at lower energies [48]. A variation of this concept using cooled protons will be used [49], thus avoiding the recombination problem (see Figure 2–8).

Located before the MPET, the Cooler Penning Trap (CPT) (see Figure 2–9) receives cooled protons from an ion source situated upstream along the TITAN beamline. As the protons enter the trap, they are trapped axially via a series of drift tubes and radially by a 6T magnetic field produced by the CPT. Once the trap is filled with cooled protons, an extracted pulse of hot HCI from the EBIT is injected into the CPT and captured. The HCI will then start to thermalize with the cooled protons via Coulomb interactions as they slowly drift towards the center of the trap due to the trapping potential being proportional to the ions charged states. Once a thermal equilibrium is reached, the rear trapping potential is slowly lowered and the most energetic protons will trickle out of the trap. As the lowering process continues, lesser hot protons will escape, lowering the remaining ions average temperature inside the trap until only the cooled HCI remain. The rear trapping potential is then lowered, allowing the cooled HCI to escape towards the MPET. The CPT is currently undergoing testing at TRIUMF and should be installed in 2009.

2.6 Measurement Penning Trap

The TITAN Measurement Penning Trap (MPET) is of similar basic design to the CPT but replaces the drift tube trapping electrodes by a specially designed hyperbolic trap (see Figure 2–10) and incorporates a Time Of Flight (TOF) measurement system for high precision mass measurements of ions. The ejected HCI from the CPT are first focused and decelerated before entering the trap, increasing the capture efficiency. As the HCI enter the Penning trap, the presence of an intense homogeneous magnetic field B will cause the HCI to undergo cyclotron oscillations at the frequency ω_c [51]

$$\omega_c = \frac{qB}{m} \tag{2.3}$$

where m and q is respectively the HCI mass and charged state.

This magnetic field confines the HCI in the two-dimensional x-y plane, perpendicular to the field lines (z-direction). A quadrupole electrostatic trapping potential is then superimposed on the magnetic field files to complete the three-dimensional confinement of the HCI. The quadrupole potential is chosen since it offers a harmonic confinement. The electric potential is given as

$$\Phi = \frac{V_0}{d^2}(x^2 + y^2 - 2z^2) \tag{2.4}$$

where V_0 is the applied potential to the electrodes and d is half the distance between the endcaps of the trap. From this trapping geometry, the HCI motion can be analytically determined as a superposition of three harmonic oscillations (see Figure 2–11). From Equation (2.4), the HCI harmonic frequency ω_z along the axial direction can be expressed as

$$\omega_z = \sqrt{\frac{qV_0}{md^2}} \tag{2.5}$$

Along the x-y plane, the remaining two independent harmonic oscillations are superposed as different convolutions of ω_c and ω_z

$$\omega_\pm = \frac{\omega_c}{2} \pm \frac{\omega_c}{2}\sqrt{1 - \frac{2\omega_z^2}{\omega_c^2}} \tag{2.6}$$

The cyclotron frequency ω_+ results from a slight perturbation of the true ω_c by the presence of the quadrupole potential whereas the magnetron frequency ω_- is created by the slow drift of the ions in the $\boldsymbol{E} \times \boldsymbol{B}$ field. As long as the analytical solution of both ω_+ and ω_- are real, the HCI will remain confined within the trap.

Once the HCI trapping is achieved, a selective elimination of individual HCI from the trap is undertaken by dipole excitation at the harmonic frequencies ω_- and ω_+. The presence of many HCI in the trap can cause shifts of the HCI's motion from the harmonic oscillations due to Coulomb ion-ion interactions. This leads to systematic errors in the extracted HCI TOF spectra from the Penning trap and affecting the mass measurement. Since $\omega_z \ll \omega_c$ in Penning traps, including the MPET, Equation 2.6 can be Taylor expanded to show that the magnetron ω_- and cyclotron ω_+ frequencies are mass-independent and mass-dependent respectively to a very good approximation [42]. These properties are subsequently used to enlarge the magnetron radius of all ions and the cyclotron radius of one specific species respectively. This latter property is deployed to remove unwanted species, such as isobaric contaminants, from the trap.

A quadrupole radio-frequency ω_{rf} excitation is applied to the HCI by the trap segmented guard electrodes. The rf-excitation is applied for a time duration T_{rf} to complete at least one full conversion of the HCI's magnetron motion into a single pure cyclotron motion.

$$T_{rf} = \frac{2a^2}{V_{rf}}\frac{m}{q}\left(\omega_+ - \omega_-\right) \tag{2.7}$$

where V_{rf} is the quadrupole rf-excitation ω_{rf} voltage amplitude at a radial distance a from the trap axis, m and q are the HCI mass and charge states respectively.

After completing the excitation, the electrostatic potential on the trap rear end cap is lowered, enabling the HCI to escape axially towards a microchannel plate (MCP) detector [52] for a TOF measurement (see Figure 2–12). While confined inside the Penning trap, the magnetic field will induce a magnetic moment $\boldsymbol{\mu}(\omega_{rf})$ on the HCI

$$\boldsymbol{\mu}(\omega_{rf}) = \frac{E_r(\omega_{rf})}{B}\hat{\boldsymbol{z}} \tag{2.8}$$

During the HCI's flight out from the Penning trap, the HCI will experience an axial force $\vec{F}$ resulting from the interaction between the HCI's magnetic moment $\boldsymbol{\mu}(\omega_{rf})$ and the magnetic field gradient of the fringe field from the Penning trap [42].

$$\boldsymbol{F} = -\boldsymbol{\nabla}(\boldsymbol{\mu}(\omega_{rf}, z)) \cdot \boldsymbol{B}(z)) = -\mu(\omega_{rf})\frac{\partial B(z)}{\partial z}\hat{\boldsymbol{z}} \tag{2.9}$$

In the process, the HCI radial kinetic energy $E_r(\omega_{rf})$ is transformed into axial kinetic energy $E_p(\omega_{rf})$. Since the axial force $\boldsymbol{F}$ is proportional to the HCI radial kinetic energy $E_r(\omega_{rf})$, the HCI excited at the frequency $\omega_{rf} = \omega_c$ will gain the most axial energy, resulting in the shortest TOF (see Figure 2–13).

The cyclotron frequency ω_c is determined by performing a frequency scan in the vicinity of the expected cyclotron frequency. The resulting TOF spectra as a function of the scanning frequency is fitted against a function curve that describes the expected TOF profile, as shown in Figure 2–14 [54]. The minimum of the fit will correspond to the cyclotron frequency ω_c and is subsequently used to calculate the HCI mass (Equation 2.3).

2.7 Motivation for this Thesis

To achieve the goal of high precision mass measurements of the order of 10^{-8} or lower, all possible contributing systematic error sources in this precision range must be investigated, evaluated and minimized. One such source of error is the ion bunch energy spread after extraction from an ion trap.

In the current MPET trapping process, the entrance trapping potential is first lowered to allow for an ion pulse to enter in the trap (see Figure 2–15). After a short time interval T_{open}, the entrance potential is raised back, trapping the ions inside a trap. The time window must be shorter than one ion axial oscillation ω_z inside the trap or some ions will be able to escape through the entrance after reflecting back from the rear potential wall. This time restriction can be expressed as

$$T_{open} \leq \frac{2\pi}{\omega_z} = 2\pi\sqrt{\frac{md^2}{qV_0}} \tag{2.10}$$

For an ion bunch with a longitudinal kinetic energy spread $\Delta E_{\parallel}$, the different ion longitudinal velocities will cause a pulse stretching along its flight path around the ion bunch average longitudinal kinetic energy $E_{\parallel}$. The most energetic ions will propagate towards the pulse front while the slowest to the rear. Equivalently, the pulse will spread in time since $v \propto 1/t$. If the time spread Δt is bigger than T_{open}, then some ions will escape during the capturing process. Since the TITAN experiment will be trapping HCI in the CPET and MPET, the time window will be even shorter since $T_{open} \propto 1/\sqrt{q}$.

Secondly, a small energy spread allows for the trapping potential V_0 to be lowered and the ions are confined to a smaller spatial region around the trap centre. This prevents the ions from nearing regions where the electrostatic and magnetic fields deviate from the theoretical values determined by the trap design. These include field misalignments and truncation of the trap electrodes, resulting in anharmonicities in the trapping field away from the harmonic oscillations ω_+, ω_- and ω_z [55].

A third benefit is a better extracted HCI TOF spectra resolution from the MPET. After the ion radial kinetic energy $E_r(\omega_{rf})$ is converted to axial kinetic energy $E_p(\omega_{rf})$ due to the axial force $\boldsymbol{F}$ (see Equation (2.9)), the resulting axial kinetic energy is added to the HCI initial longitudinal kinetic energy $E_{0\parallel}$, resulting in a TOF change (see Figure 2–16). Due to the longitudinal energy spread $\Delta E_{\parallel}$, the extracted HCI initial total energy E_0 will have a range of different values between $E_0 - \Delta E_{\parallel} < E_0 < E_0 + \Delta E_{\parallel}$, causing the final kinetic energy E_f and TOF profiles (see Figure 2–13) to lose their symmetries by having small vertical fluctuations across the scanned frequency spectrum. The subsequent function curve fit onto the experimental data will result in an error width increase on the calculated cyclotron frequency ω_c and in turn, on the mass measurement.

The extracted ion pulse longitudinal energy spread from the ion traps can be measured by, for example, a Retarding Energy Field Analyzer (RFA). This would permit to fine tune the cooling and extraction processes, which would eventually lead to minimizing the energy spread.

This is vital for the EBIT since the expected longitudinal energy spread $\Delta E_{\parallel} \sim 10$ eV/q will be significant. As such, the RFA will be primarily used for measuring the extracted ion pulse energy spread from the EBIT.

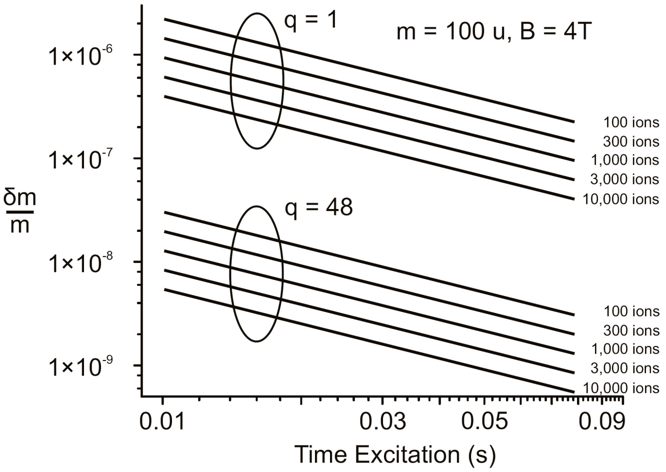

Figure 2–1: Variations in mass measurement error for singly and highly charged ions of mass 100 u inside a 4T Penning trap as a function of the number of trapped ions.

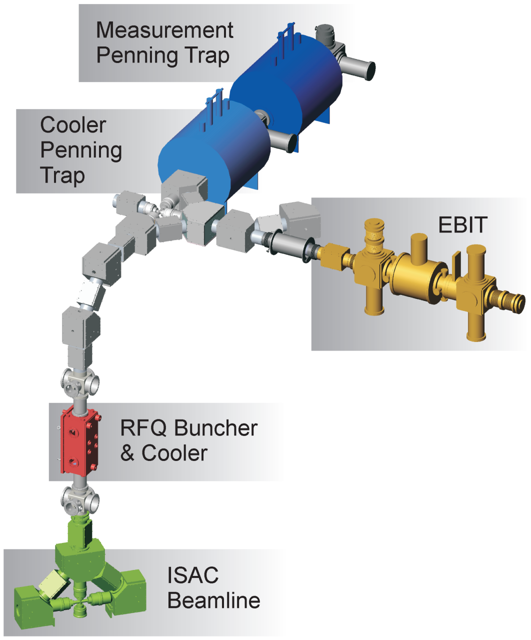

Figure 2–2: Schematic view of the TITAN experiment. The principal components shown are the ISAC beamline, RFQ, EBIT, Cooler Penning trap and Penning trap. The Cooler Penning trap is currently not installed. Taken from [2].

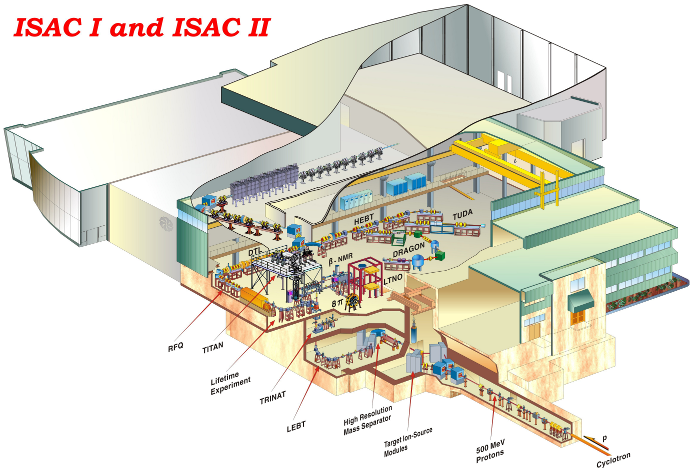

Figure 2–3: Schematic view of the ISAC I & II experimental halls at TRIUMF. The TITAN experiment is situated in ISAC I. Taken from [3]

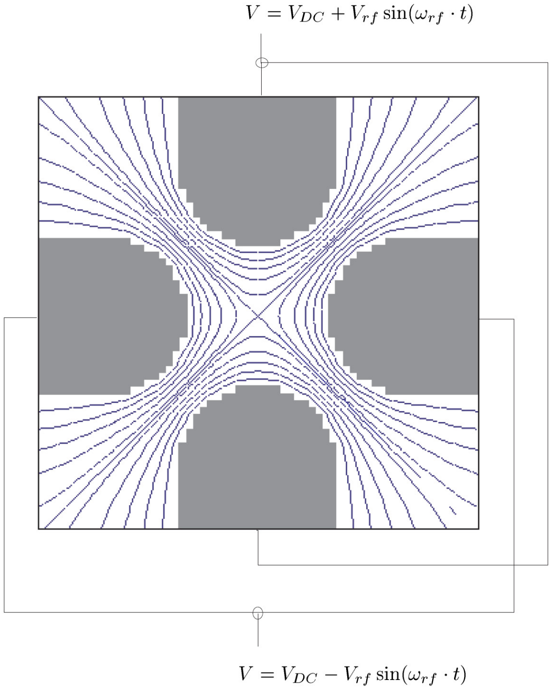

Figure 2–4: Schematic cross-section view of the RFQ electrodes with lines of equipotential resulting from the applied squared-rf potentials on the electrodes. Taken from [42].

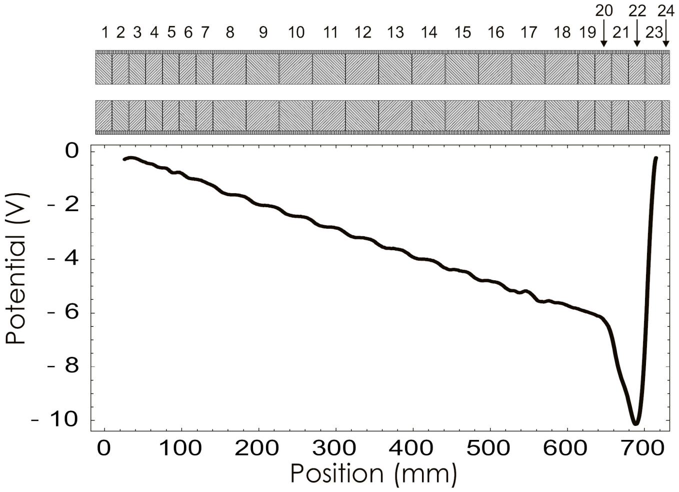

Figure 2–5: Top: Segmented electrodes of the RFQ as function of axial position. Bottom: Corresponding simulated RFQ longitudinal trapping potential. Taken from [41].

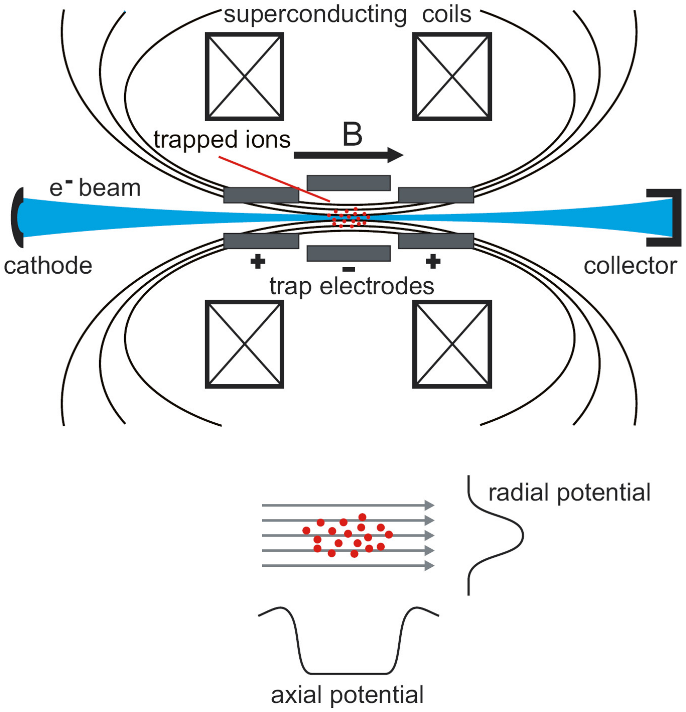

Figure 2–6: Schematic view of the TITAN EBIT, together with the longitudinal and radial trapping potentials. The longitudinal trapping is performed by the trap electrodes and the radial trapping is done by the negative space charge potential of the electron beam and magnetic field. Taken from [4].

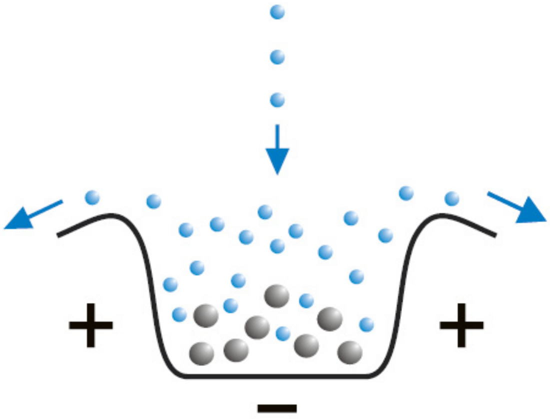

Figure 2–7: Schematic of EBIT evaporative cooling technique. Low Z atoms (blue) are injected into the trap where they gain thermal energy from the hot HCI (grey) by Coulomb interactions. Since the cooling ions have a lower charge state, they will not be as tightly bounded in the potential well. The most energetic cooling ions will overcome the barrier and escape axially from the trap, removing excess energy from the HCI in the process.

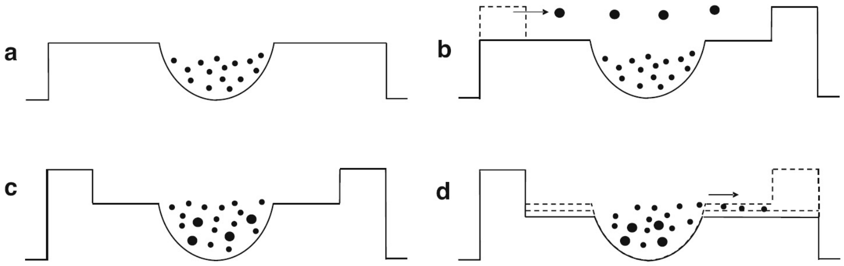

Figure 2–8: Proposed cooling procedure for trapped HCI in the TITAN CPT. a) Cooled protons are injected and trapped by lowering the central trapping electrode potentials. b) A hot HCI bunch is injected into the trap and the rear electrode potential is raised to stop the HCI. After entering the trap, the front electrode potential is also raised, trapping the HCI. c) The HCI and proton interact by Coulomb collisions and thermalize. The now cooled HCI segregates to the bottom of the trapping potential. d) The rear and middle electrode potentials are slowly lowered, allowing the warm protons to escape. This process continues until only the HCI remain in the trap. The rear-half electrodes are then lowered and the cooled HCI can proceed to the Penning Trap. Taken from [49].

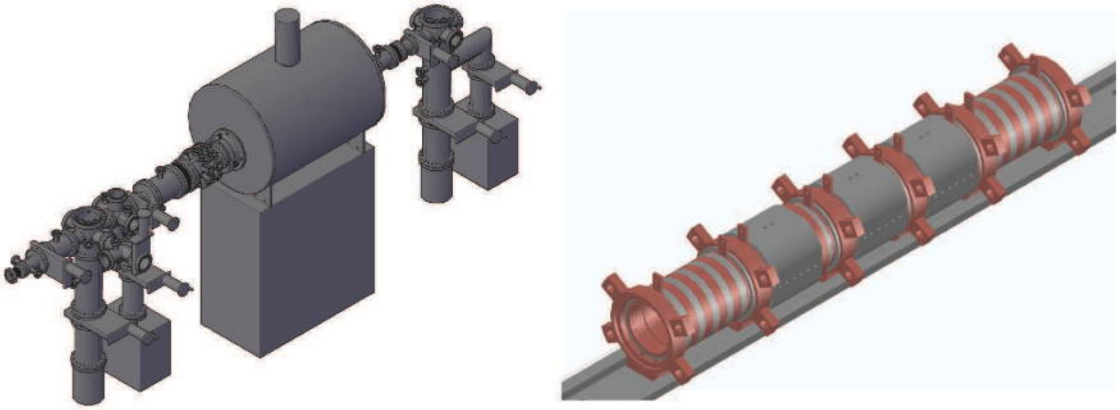

Figure 2–9: Left: Cooler Penning Trap setup designed at University of Manitoba. The trap has a length of 120 cm. Right: Main trapping electrode structure for the Cooler Penning Trap. The structure is composed of 28 electrodes, permitting for time-dependent trapping potentials. Additional internal electrodes are quad-split and used for rf-excitation. Taken from [50].

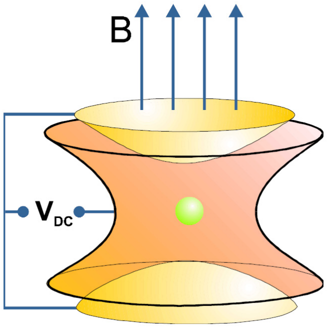

Figure 2–10: Schematic view of the structure of a Penning trap. Taken from [5].

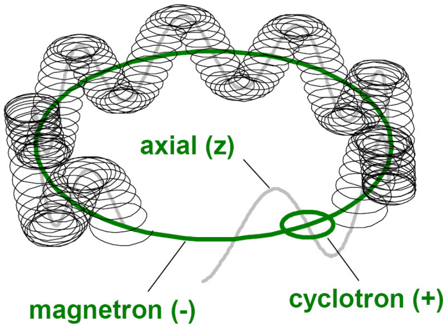

Figure 2–11: Ion motion inside a Penning Trap. The motion can be separated in three distinct harmonic oscillations: axial (z), magnetron (-) and cyclotron (+), described by Equations (2.5) and (2.6). Taken from [5].

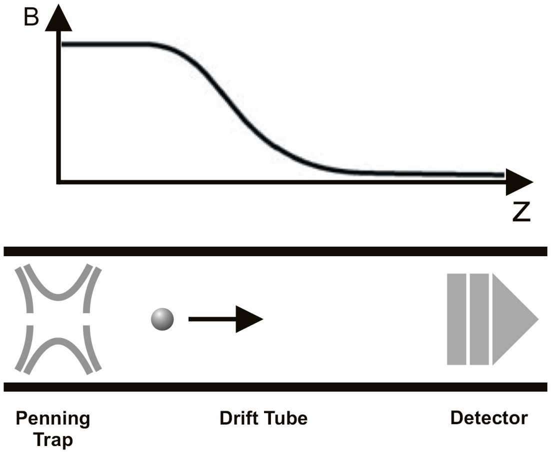

Figure 2–12: Time of flight detection system employed with a Penning trap for mass measurements. Top graph represents the magnetic field strength along the length of the drift tube. The magnetic field is along the axial direction.

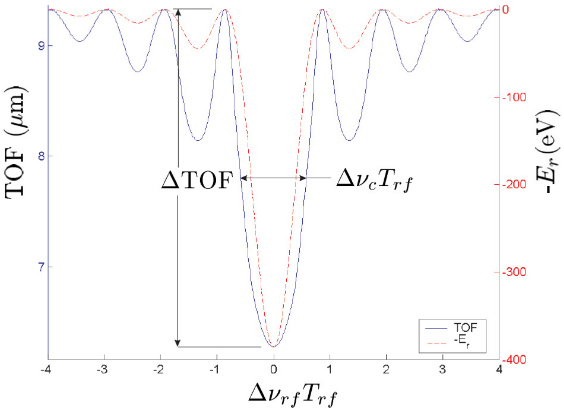

Figure 2–13: Time of Flight and radial kinetic energy spectra as a function of the rf-excitation frequency ν_{rf}. Taken from [42].

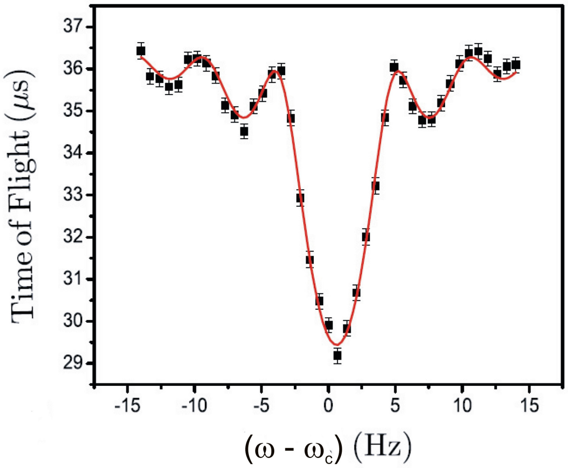

Figure 2–14: Example of a time of flight spectrum with ${}^6Li$. The overlapping red line is the theoretical line shape with ω_c = 9 450 927 Hz. Taken from [53].

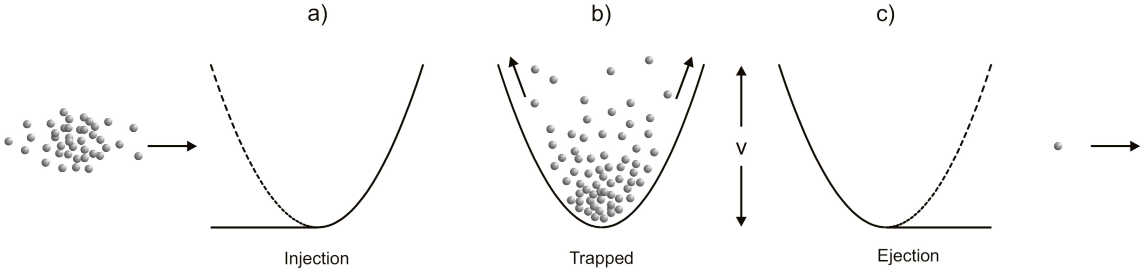

Figure 2–15: MPET ion injection and extraction process. a) The front potential is lowered for injecting ions inside the trap. b) The front potential is quickly raised before the ions are able to escape axially after reflecting back from the rear potential. The trap depth is determined by the incoming ion beam energy, preventing ions from overcoming the potential well. Ions are slowly removed radially using cyclotron ω_+ excitation. c) Once only 1-2 ions remain, the rear potential is lowered and the ions are extracted from the Penning trap for a TOF measurement.

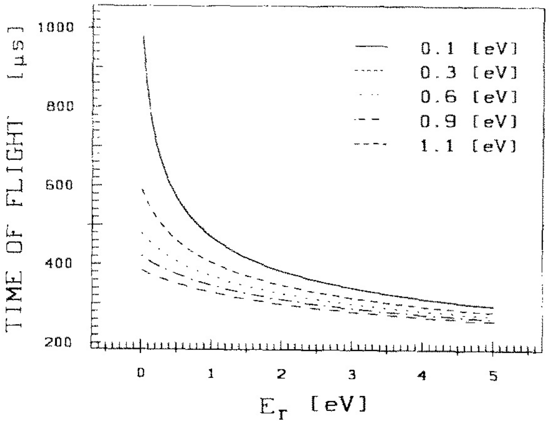

Figure 2–16: Calculated Time of Flight from a Penning trap to a detector along the fringe field as a function of the ions' radial kinetic energy E_r for difference initial axial kinetic energies $E_{0||}$ between 0.1 - 1.1 eV. Reducing the initial axial kinetic energy $E_{0||}$ significantly increases the time of flight for small radial kinetic energy values and the amplitude of the TOF spectra in Figure 2–13. Taken from [56].

CHAPTER 3
Experimental Methods to measure the Energy Spread of Ion Beams

The ion beam longitudinal energy spread plays an significant role in the attainable resolution of numerous experiments. By measuring its contribution, experimentalists can determine the extent the energy spread affects the error in their final measurement. Various methods have been previously developed and put into practical use. Four different methods that can be adapted for the TITAN experiment are investigated. A detailed description of each is presented and considered for their practicability with the current TITAN setup.

3.1 Time of Flight (TOF)

The kinetic energy E_k of a non-relativistic particle can be calculated from its mass m and velocity v as $E_k = \frac{1}{2}mv^2$. If no external forces are applied on the particle then, by the law of inertia, its velocity v must be conserved. A particle moving at a constant velocity v through a linear displacement Δx in a time interval Δt is expressed as

$$v = \frac{\Delta x}{\Delta t} = \frac{x_f - x_i}{t_f - t_i} \tag{3.1}$$

where (x_i, t_i) and (x_f, t_f) are respectively the particle initial and final position-time coordinates, as shown in Figure 3–1.

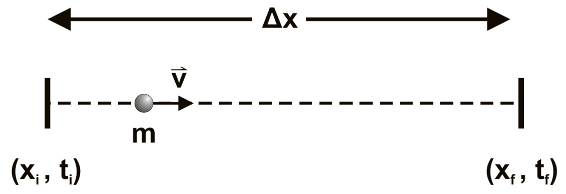

Figure 3–1: Schematic diagram of the Time of Flight process. The ion kinetic energy is determined by the time required to travel at a constant velocity the distance between two known points along its direction of travel in a field-free region.

By measuring the time Δt required for the particle to travel a distance Δx between two known fixed points (x_i, x_f) along a free field region, the velocity can be calculated which, with the particle's mass, allows to calculate its kinetic energy. This is the principle behind the TOF method.

In a pulsed ion beam, individual pulses have an longitudinal kinetic energy spread $\Delta E_{\|}$ centred around an average longitudinal beam energy $E_{\|}$. By letting the pulses drift through a field free region along a beamline section and assuming that the Coulomb ion-ion interactions are negligible within this time frame, the TOF method can be implemented. The energy spread is observable in the ion pulse TOF spectrum as a time spread δt since $E_k \propto 1/t^2$. From Equation (3.1) and the kinetic energy E_k equation, it can be shown that the time and energy spreads are related as

$$\frac{\Delta E_{\|}}{E_{\|}} = 2\frac{\delta t}{\Delta t} \tag{3.2}$$

For the implementation of this technique, a free field drift region must be present where a time sensitive ion detection system can be placed. The nature of the detection system will dependent on the experiment requirements and constraints. Most often, multichannel Plate (MCP) detectors are preferred due to their good time resolution ($<$ 100 ps) and sensitivity to individual ions. Two different TOF techniques using one and two MCPs respectively that can be implemented in the TITAN experiment will be described.

3.1.1 Energy Spread Measurements using 1 MCP

During the extraction phase of the TITAN ion traps, an external trigger signal is sent to change the applied potentials on the axial trapping electrodes, releasing the trapped ions. This trigger signal can be used as the initial timing reference for a TOF measurement. By placing an MCP at some known distance downstream from the ion trap, along the ion flight path and synchronizing the MCP detection system's reference clock with the extraction trigger signal, a TOF spectrum can be measured for the outgoing pulse (see Figure 3–2). An advantage of this technique is its simplicity by only requiring the installation of a retractable MCP detector at any suitable beamline access point past the ion trap.

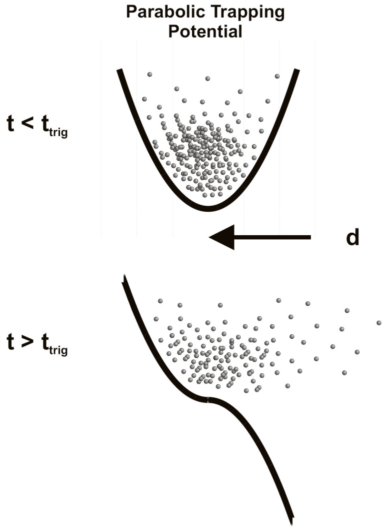

Figure 3–2: Time of Flight using a trapping potential and one MCP. From an external time trigger, the ions are released from the trapping potential towards a MCP and the timing clock is started on the MCP detection system. A time stamp is allocated for each ion detected by the MCP. The energy of the ions are obtained from the travel distance between the MCP and trapping potential, the time stamp and the mass of the ion.

However, this method has some drawbacks. Foremost, the region between the trap and the MCP must be field free. The intense magnetic fields of the EBIT and CPET would inevitably affect the motion of the extracted ions as seen in Section 2.6, resulting in perturbed TOF spectra.

A second consideration is the ion pulse random velocity direction distribution after reaching thermal equilibrium in the trap. When the longitudinal potential barrier is lowered, approximately half of the ions have some rearward velocity component with respect to the downstream current. These ions will escape after reflecting off the rear potential. The escaping ions will have an approximate time spread

$$\Delta t = 2\frac{\sqrt{2mV}}{qE} \tag{3.3}$$

where qV is the ion kinetic energy and E is the extraction electric field due to the additional distance the ions must travel before reaching the MCP. This extraction time spread will be convoluted with the time spread originating from the ion pulse longitudinal energy spread, resulting in a larger overall time spread error in the measured TOF spectra and in turn, to the calculated energy spread.

3.1.2 Energy Spread Measurements using 2 MCP

The 2 MCP technique employs a pair of MCPs positioned at different locations along the ion's flight path to measure the time difference Δt from the TOF spectra of each MCP (see Figure 3–3). A common external time trigger is used to synchronize MCPs reference clocks. Compared to the 1 MCP method, this eliminates the problem associated with the extraction time spread (Equation(3.3)) and allows to place the MCPs in any available free field region downstream from the trap.

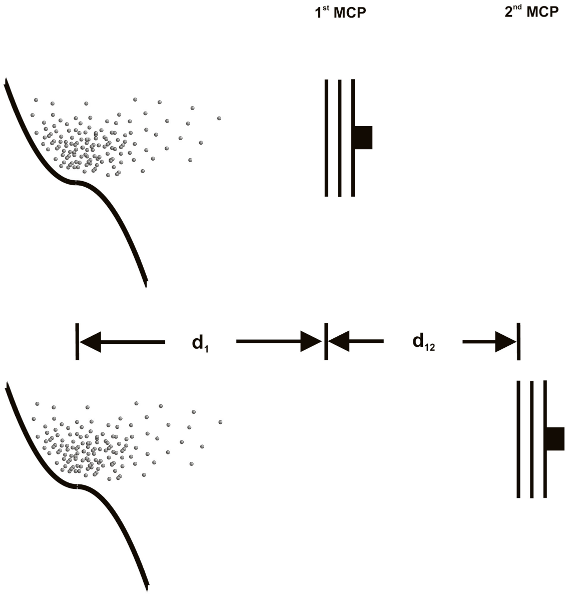

Figure 3–3: Time of Flight using two MCPs. Similar technique as used for the one MCP and trapping potential but uses the distance and time difference between the two MCPs. Each measurement can only be performed with one MCP at any given time.

However, a fundamental disadvantage arises from the MCP's destructive measurements of the ion pulses; any TOF measurement is limited to one MCP at any given moment. Since a TOF spectrum from each MCP originates from an unique pulse, beam stability is absolutely essential to ensure accurate TOF difference calculations.

3.2 Collinear Laser Spectroscopy

In laser spectroscopy, a laser beam is guided towards a sample group of ions or atoms. By selecting the appropriate frequency ν, the laser excites an ion atomic electron from an atomic orbital with energy E_i to a higher atomic orbital with energy E_f. After a short time delay, the excited electron decays back to its initial state and emits a photon of frequency ν_0 defined by the energy difference $E_f - E_i = h\nu_0$ where h is Planck's constant. Due to the ions' relative motion with respect to the laboratory (rest) frame, the observed frequency of the emitted photon will have a Doppler shift $\Delta\nu_D$ [57]

$$\Delta\nu_D = \nu_0 \left(\frac{2k_BT}{mc^2}\right)^{1/2} \tag{3.4}$$

where T and m are respectively the ion's temperature and mass and k_B is the Boltzmann constant. The ion pulse longitudinal energy spread $\Delta E_{\parallel}$ will translate to a longitudinal velocity spread δv_z. As such, the different Doppler shifts from each individual ion creates a Doppler width $\delta\nu_D$ for the bunch expressed has [58]

$$\delta\nu_D = \nu \frac{\delta v_z}{c} \tag{3.5}$$

To improve the fluorescence photon emission rate from the ion bunches, collinear laser spectroscopy is instead employed. The laser beam is guided towards a mass-separated ion beam along its direction of travel, where both beams are subsequently overlapped [57]. Using the property of conservation of energy spread ΔE under electrostatic acceleration, the energy spread can be calculated from the Doppler width $\delta\nu_D$ and the Doppler shift $\Delta\nu_D$ [59, 60].

$$\Delta E = m v_z \delta v_z = \frac{mc^2}{\nu^2}\Delta\nu_D \delta\nu_D = const. \tag{3.6}$$

where v_z is the ion beam average longitudinal velocity. Whereas the ion beam velocity v_z increasing during acceleration, the Doppler width $\delta\nu_D$ reciprocally decreases since the longitudinal velocity spread δv_z shrinks. The Doppler width can be rewritten as a function of the acceleration voltage change ΔV_{acc} [58]

$$\delta\nu_D = \nu\frac{\delta v_z}{c} = \frac{\nu}{c}\frac{e}{mv_z}\Delta V_{acc} = \nu\sqrt{\frac{eV_{acc}}{mc^2}}\frac{\Delta V_{acc}}{V_{acc}} \tag{3.7}$$

From Equations (3.4), (3.6) and (3.7), the longitudinal energy spread $\Delta E_{\parallel}$ is then

$$\Delta E_{\parallel} = \frac{\nu_0}{\nu}(2k_B TeV_{acc})^{1/2}\frac{\Delta V_{acc}}{V_{acc}} \tag{3.8}$$

From Equation (3.8), there is a few properties that are experimentally advantageous: the resonance frequency ν_0 of atoms are well known, calibration of the laser frequency ν is non-essential but must only remain fix during the voltage scan and the change in the acceleration voltage ΔV_{acc} is the only independent variable.

However, the benefits are outweighed by the technical requirements and costs of incorporating the necessary instruments to the TITAN beamline. These include a laser and guiding system, a photomultiplier tube and a lightpipe to guide the emitted photons from the beamline to the photomultiplier tube (see Figure 3–4). In addition, the resonance frequency ν_0 of most ions lies in the ultraviolet to X-ray (for HCI) regions, well outside the excitation range of available lasers and the detection efficiency of photomultiplier tubes within this range is typically low [61]. To increase the detection efficiency, a charge-exchange cell is employed to neutralize the ions and shift the resonance frequency into the optical range. As a result, this approach for measuring the energy spread of highly ionized atoms proves to be impractical in practice.

3.3 Retarding Field Energy Analyzer

In a basic three mesh RFA design, three equally spaced finely woven metallic meshes with distinct applied potentials, as shown in Figure 3–5 are used to filter the ion beam longitudinal kinetic energy profile. A high positive potential V is applied to the central mesh to act as a longitudinal kinetic energy high-pass filter (see Figure 3–6) and the outer meshes have a small

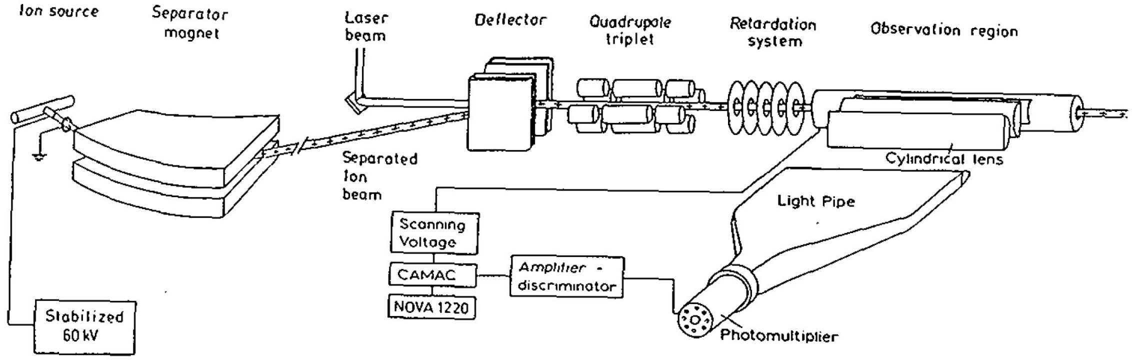

Figure 3–4: Schematic diagram of Collinear Laser Spectroscopy installation employed at the ISOLDE facility at CERN. Taken from [57]

negative potential (< 100 V) to minimize interference from secondary electron emissions, due to ion surface impacts on the meshes and collector, in the ion count. Ions will pass through the filter if their longitudinal kinetic energy is larger than the potential barrier ($qV_0 > qV$) where q is the ion charged state. The ions that survive the trip through the three meshes are counted using a collector, either a Faraday cup or a MCP. By scanning through the central mesh applied voltage V, an ion count profile as a function of the applied voltage is taken. The ion pulse longitudinal energy spread is obtained from the first derivative of the plot as a function of the applied voltage V (see Figure 3–7). The full width at half maximum (FWHM) from the derivative curve then represents the ion pulse longitudinal energy spread $\Delta E_{\|}$.

This technique has a few benefits. It is a simple concept which can be modelled and optimized using computational simulations, allowing for the theoretical determination of the RFA energy resolution error $\Delta E/E$. The apparatus can be compactly designed to allow installation in a single access port along a field free region of the beamline. The RFA can be used with either a pulsed or continuous beam configuration and the applied filtering voltage V is the only independent variable.

However, there are also a series of drawbacks. Foremost is the non-uniformity of the electric field in the vicinity of the mesh surfaces, which creates two sources of errors in the RFA energy resolution. First, the potential strength is inversely proportional to the distance from the

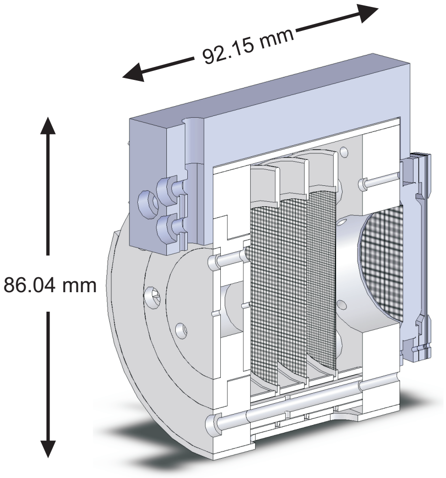

Figure 3–5: Section view of the TITAN RFA. The RFA has three meshes; a central retarding mesh and two outer meshes. The retarding mesh filters the longitudinal kinetic energy component of the incoming ions. The outer meshes provides two homogeneous electric field regions between them and the retarding mesh and minimizes secondary electrons, due to ion impacts on meshes and collector, from reaching the retarding mesh.

wire surface, resulting in a lower electric potential within the mesh openings than the applied potential on the mesh. Ions with slightly lower kinetic energy than the applied potential ($qV_0 \lessapprox qV$) can pass through these depressions, inflating the ion counts for ions with kinetic energies above the potential barrier. Secondly, the non-linearity of the electric field creates a transversal component $\boldsymbol{E}_\perp$, resulting in a transversal force $\boldsymbol{F}_\perp$ which deflects ions around the mesh wires. An ion count enhancement above the theoretical maximum obtained from the mesh effective transparency can then be seen when $qV_0 \approx qV$.

A mesh with smaller wire spacing would increase the energy resolution by reducing the magnitude of both these errors [62, 63] but would also decrease the mesh effective transparency (see Table 3–1). Consequently, a compromise between resolution and transparency must be decided from the requirements for the TITAN experiment. These errors will be described in detail in section 4.2.1 and 4.2.2, with the final mesh dimension selected in section 5.3.1.

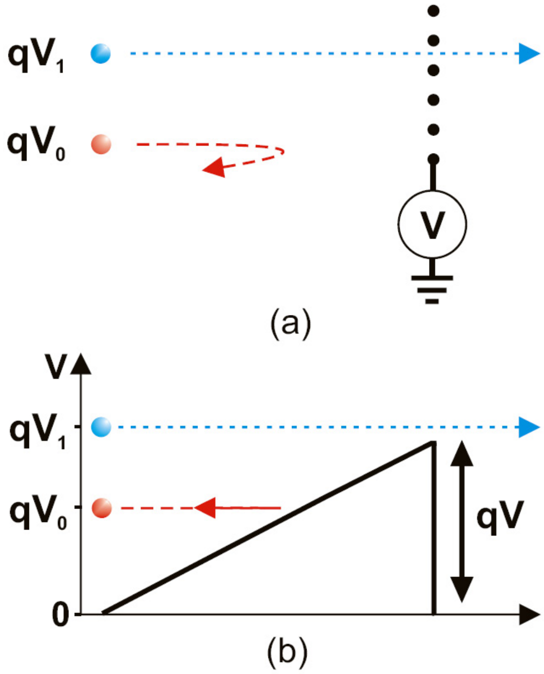

Figure 3–6: Schematic diagram of a perfect infinite mesh with zero thickness (a) with equivalent potential barrier (b) where V is the mesh applied retarding voltage. For two ions with equivalent charged state q and different potential energies $qV_0 < qV < qV_1$ starting in a grounded potential field, the latter is able to climb up the potential ramp and pass through the mesh's potential barrier whereas the former is reflected back.

Finally, since the electric field vectorial direction inside the RFA is parallel to the beamline axis, the RFA only filters the normal component of the ion kinetic energy $E_{\|}$ with respect to the meshes. The ion beam must be collimated using a pair of slits to minimize any transversal kinetic energy component $E_{\perp}$ of the ions.

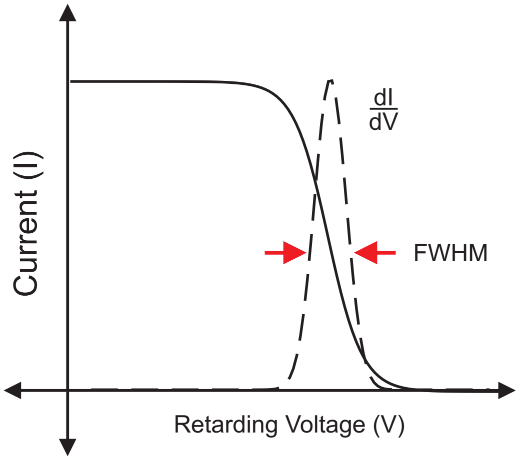

Figure 3–7: Plot of the ion current as a function of the retarding voltage applied on the mesh. The energy spread ΔE is obtained from the FWHM of derivative $\frac{dI}{dV}$.

Table 3–1: Effective transparencies of one and three mesh configurations composed of 25 μm diameter wires as a function of the wire spacing d

d (μm)	30	50	75	100	250	500	1000
One mesh (%)	0.028	0.250	0.444	0.563	0.810	0.903	0.951
Three meshes (%)	2×10^{-4}	0.016	0.088	0.178	0.531	0.735	0.859

CHAPTER 4
Working Principle of a RFA

In this chapter, an in-depth analysis of the working principle laying behind the TITAN RFA's three meshes design will be presented, accompanied with the sources of errors and resulting energy resolution errors. The source of secondary electron emission and its effect on the RFA ion count will be explored. Ion counting technique used and the determination of the energy spread are then discussed.

4.1 Basic Principles of a RFA

The RFA utilizes the principle of electrostatic repulsion to passively filter ions with kinetic energy above a certain threshold. For an ion with charge q interacting with an electric field $\boldsymbol{E}$, the force $\boldsymbol{F}$ felt by the ion, derived from the Lorentz law, is expressed as

$$\boldsymbol{F} = q\boldsymbol{E} \tag{4.1}$$

Since this force is parallel to the electric field vectorial direction, the field must be aligned anti-parallel to the ion longitudinal kinetic energy component $E_{\|}$. Three identical meshes are used to create a homogenous longitudinal electric field configuration with minimal transversal contribution. The meshes are parallel to each other with a regular spacing l and normal to the ion beam. Small negative potentials are applied on the outer meshes to minimize secondary electron emissions from ion surface impacts from interfering with the ion counts. A variable high positive potential is applied to the central retarding mesh to filter the ion longitudinal kinetic energy. Sufficiently away from the mesh surface, each mesh can be approximated to a high degree of accuracy by a conducting plate. Under this assumption, the electric field $\boldsymbol{E}$ created between two conducting plates with different applied voltage potentials is

$$\boldsymbol{E} = \frac{\boldsymbol{\Delta V}}{l} \tag{4.2}$$

where ΔV is the potential difference between two consecutive meshes and the electric field vectorial direction is from the highest to lowest voltage potential. From the central mesh positive potential and outer meshes negative potentials, the electric field vectorial direction between the two first meshes encountered by an incoming ion is anti-parallel and parallel between the last two meshes. As the ion travels through the first electric field region, the Coulomb force $\boldsymbol{F}$ will reduce the ion longitudinal kinetic energy. If the ion longitudinal kinetic energy $E_{\|} = qV_0$ is larger than the central mesh applied potential V, it will overcome the barrier and enter the second electric field region (see Figure 3–5). In the second region, the ion will regain almost all the lost longitudinal kinetic energy due to the quasi symmetric parallel Coulomb force. For ions that pass unimpeded through the three meshes, they eventually impact against a collector and are subsequently counted.

Various sources of errors caused by the geometry of the meshes, the beam quality and secondary electron emissions will create an energy resolution error $\Delta E/E$ on the RFA. These have been previously determined theoretically as a function of the mesh properties and the RFA design.

4.2 Source of Errors

4.2.1 Potential Depression in Mesh Openings

As the ions approaches the mesh surface, the electric equipotential lines will diverge from a linear homogeneous structure to a periodic wavy pattern (see Figure 4–1), consequence of the mesh interlaced wire design. Since the electric potential decreases with distance from the wire surface, the mesh openings have a lower electric potential than the applied potential on the wires. The magnitude of the drop is a function of the mesh geometry; the wire diameter d, the separation between the wire surfaces s and the applied voltage V.

An ion with longitudinal kinetic energy qV_0 which would have been reflected by a charged plate with applied voltage V where $V_0 \lessapprox V$ can pass through the mesh openings. This augments

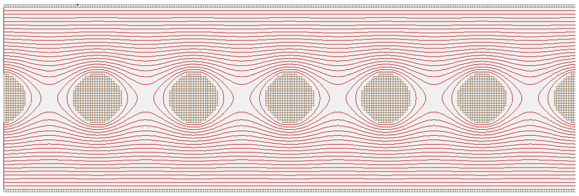

Figure 4–1: Simulated cross-sectional view of a simple mesh with equipotential lines. As one approaches the mesh surface, the equipotential lines transforms from a linear shape to a sinusoidal pattern. The magnitude of this error on the measured energy spread is determined by the wire spacing s and diameter d.

the measured ions counts for a specific longitudinal kinetic energy qV and increases the observed beam average longitudinal kinetic energy. From the mesh d/s ratio, the error magnitude in the ranges $0.03 \lesssim d/s \lesssim 0.1$ [62] and $0.1 \lesssim d/s \lesssim 1$ [63] can be expressed as

$$\left.\frac{\Delta E}{E}\right|_{open} = \begin{cases} \frac{s}{\pi^{3/2} l} \left[1 + \frac{\sqrt{\pi} d}{s} tan^{-1}\left(\frac{\sqrt{\pi} d}{2s}\right) - \frac{\sqrt{\pi} d}{s} tan^{-1}\left(\frac{\sqrt{\pi} d}{s}\right)\right] & 0.1 \lesssim \frac{d}{s} \lesssim 1 \\ \frac{\delta + d/2\pi}{(d/2+\delta)(1-d/0.58s)} & 0.03 \lesssim \frac{d}{s} \lesssim 0.1 \end{cases} \tag{4.3}$$

where

$$\delta = \frac{0.58}{4\pi}\left[-\ln\left(2 - 2\cos\left(\frac{\pi}{0.58}\frac{d}{s}\right)\right) - 4\cos\left(\frac{\pi}{0.58}\frac{d}{s}\right)\exp\left(\frac{-4\pi l}{0.58 s}\right)\right] \tag{4.4}$$

4.2.2 Ion Focusing in Mesh Openings

The equipotential lines dimpled structure across the mesh surface results in a perpendicular component of the electric field $\boldsymbol{E}_{\perp}$, creating a perpendicular force $\boldsymbol{F}_{\perp}$ to the ions' travel direction. As the retarding mesh potential becomes bigger than the ion kinetic energy ($V \gtrsim V_0$), the ions will deflect around the mesh wires and into the openings. This results in an enhancement in the number of ions passing through the mesh, above the theoretical calculated value from the three meshes total effective transparency. The focusing continues until the central mesh opening electric potential approaches the critical value V_0 (see Figure 4–2). The magnitude of the error has been theoretically determined for the same two ranges as described in section 4.2.1 and are expressed as

$$\left.\frac{\Delta E}{E}\right|_f = \begin{cases} \frac{\sqrt{\pi}d}{2s}\left(1+\frac{\sqrt{\pi}d}{4s}\right)\frac{\Delta E}{E}|_{open} & 0.1 \lesssim \frac{d}{s} \lesssim 1 \\ \frac{1.16}{\frac{l}{s}+2\delta}\left(\frac{0.58-0.783\frac{d}{s}}{2.223+22.09\frac{d}{s}}\right) & 0.03 \lesssim \frac{d}{s} \lesssim 0.1 \end{cases} \tag{4.5}$$

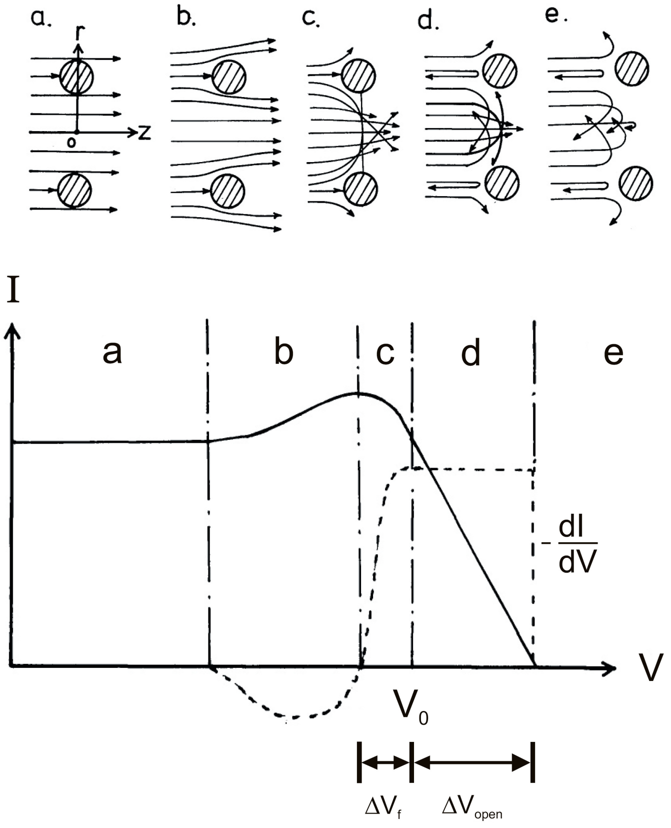

Figure 4–2: Top: Schematic views of ion trajectories with longitudinal kinetic energy qV_0 for different applied potential V on mesh. Bottom: Complementary plot of the current I as function of the applied voltage V on mesh with corresponding regions. a) $V \ll V_0$: Ion trajectories are unaffected by the applied potential of the mesh. b) $V < V_0$: Electrostatic ion focusing around wires of mesh starts to be noticeable as the radial component of the electric field increases. c) $V \lesssim V_0$: Further focusing with increase deflections. d) $V_0 < V < V_0 + \Delta V_{open}$: Partial reflection of ions with decreasing equipotential surface V_0 within the mesh opening. e) $V > V_0 + \Delta V_{open}$: All ions are reflected. Taken from [63].

4.2.3 Transverse Kinetic Energy

The electric field vectorial direction must be anti-parallel with the incoming ions to retard its longitudinal kinetic energy component $E_{\|}$. Whereas the electric field direction is controlled using the meshes, the incoming ions possess some transverse kinetic energy $E_{\perp}$ with respect to their direction of travel due to various electrostatic interactions via steerers and Einzel lenses along the beamline and Coulomb ion-ion interaction inside an ion bunch. The magnitude of this error is [64]

$$\left.\frac{\Delta E}{E}\right|_{\perp} = \sin^2(\theta) \tag{4.6}$$

where θ is the angle between the mesh normal and the ion direction of travel.

To reduce the error, two slits are normally placed ahead of the RFA to collimate the beam before reaching the meshes (see Figure 4–3). For two axially aligned circular slits of radius r with the outer faces separated by a distance d, the maximum beam divergence with respect to the axial direction is

$$\theta = \tan^{-1}\left(\frac{2r}{d}\right) \tag{4.7}$$

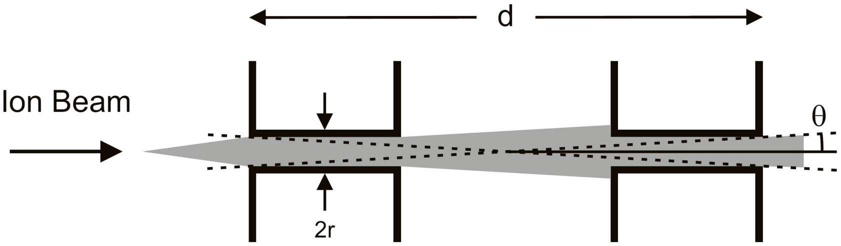

Figure 4–3: Schematic diagram of an ion beam profile passing through two collimating slits. The maximum beam divergence θ is determine by the slit radius r and the distance d between the outer faces of the slits.

4.2.4 Lensing Effect

Due to the electric fields created from the meshes, the circular openings nearest the outer meshes along the ion travel path produces an small lensing effect, which alters an ion's direction of travel (see Figure 4–4). From electron optics, a difference in electric field strengths $\boldsymbol{E_1}$ and $\boldsymbol{E_3}$ on the left and right sides of a circular aperture will create a electrostatic lens near the plane axis with a focal power [65]

$$\frac{1}{f} = \frac{\boldsymbol{E_1} - \boldsymbol{E_3}}{4V_0} \tag{4.8}$$

where f is the focal length and qV_0 is the ion longitudinal kinetic energy.

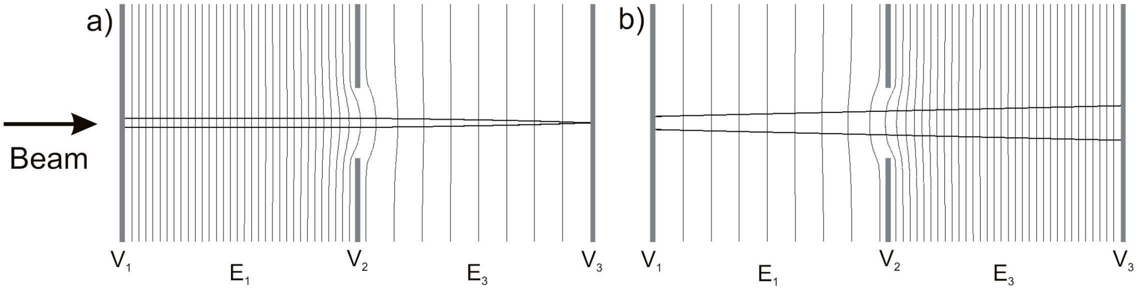

Figure 4–4: Schematics view of aperture focusing for different electric field regions ($\boldsymbol{E_1}$&$\boldsymbol{E_3}$) on either side of the aperture with equipotential lines. A strong electric field will bulge through the aperture towards the weak field. This introduces a radial component in the electric field $\boldsymbol{E_\perp}$, causing either a focusing or defocusing effect depending on the direction of travel of the ion beam. a) An ion beam passing from a region of strong to weak field will focus the beam. b) An ion beam passing from a region of weak to strong field will defocus the beam. Taken from [66].

Consequently, a parallel beam passing through the circular slit of radius r will have a divergence angle

$$\theta = \frac{r}{f} \tag{4.9}$$

Combining with Equations (4.6) and (4.8), the lensing effect error is

$$\left.\frac{\Delta E}{E}\right|_{lens} = \sin^2\left(\frac{r(\boldsymbol{E_1} - \boldsymbol{E_3})}{4V_0}\right) \tag{4.10}$$

4.3 Secondary Electron Emission

The primary role of the two outer meshes is to reduce secondary electron emission interference on the total ion count measured by the RFA. Since the ions will collide either against the slits, meshes or the collector, a shower of electrons can be emitted from their respective surfaces for each impact under certain conditions [67] (see Figure 4–5). These unbounded electrons can subsequently interact with ions or neutrals within the RFA and hinder the ion count in the following ways: ion-electron recombination, neutral ionization or secondary electron false ion counts.

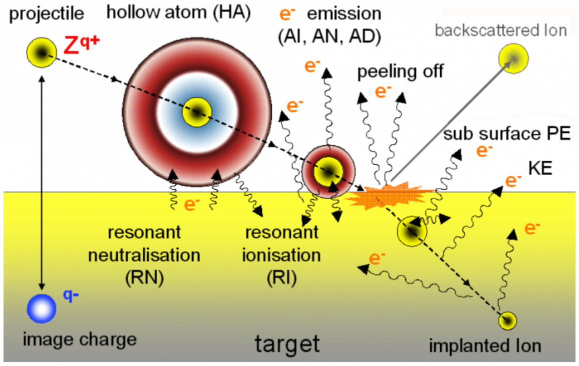

Figure 4–5: Multiply charged ion (MCI) - surface interaction on a clean metal surface. Numerous processes participate in the ejection of bound electrons from the surface [68, 69]. Above the surface, the processes are dominated by the ion potential energy with the creation of a hollow atom and its subsequent decay. At the surface and below, the potential and kinetic energies conjointly cooperate in liberating further electrons until the ion is neutralized. Taken from [70]

4.3.1 Ion-Electron Recombination

If an incoming ion with initial charge q_i recombines with one or many unbound secondary electrons, the ion final charged state $q_f < q_i$ will enable it to pass through the RFA applied retarding potential V since the latter can only filter an unique charged state q for a beam energy qV_0 at any given moment. This inflexibility requires that ion-electron recombinations must be minimized while the ion beam travels inside the RFA, as a consequence that the lower charged ions will reach the collector and result in a false ion count.

Since the TITAN beamline operates in the ultra high vacuum (UHV) regime (P $\approx 10^{-9}$ torr), the low vacuum residual gas density ($\rho_{vac} \approx 3 \times 10^{13}$ molecules cm^{-3}) limits the ion-electron recombination paths to two modes [71]:

(a) Radiative Recombination (RR)

$$e^- + A^+(i) \rightarrow A(f) + h\nu \tag{4.11}$$

(b) Dielectronic Recombination (DR)

$$e^- + A^{Z+}(i) \rightleftharpoons \left[A^{(Z-1)+}(k)\right] \rightarrow A^{(Z-1)+}(f) + h\nu \tag{4.12}$$

where $h\nu$ is the emitted photon energy, Z is the ion charged state and i, k, f are the ion A initial, intermediate and final states. A detailed description of each process can be found in Ref. [72].

For the RFA experimental testing using a singly charged ion beam provided by the RFQ and TITAN ion source 6.1, the total electronic recombination rate α_t of Li$^+$ and Na$^+$ are dominated by RR since they do not possess low-lying autoionization states and thus are not subject to low temperature DR [73]. Furthermore, the low ion temperature T = 400 K resulting from the RFQ buffer gas cooling [41] dramatically decreases the DR rate α_{DR} of K$^+$ below measurable levels [74]. Consequently, DR is not excepted to be observed within the RFA.

Considering only the RR contribution, the radiative recombination rate α_{RR} for Li$^+$, Na$^+$ and K$^+$ are shown in Table 4–1. Since all three rates are of the same magnitude, let us focus on Li$^+$. Let a 1 nA Li$^+$ beam with 1 keV energy enter the RFA with approximately half colliding between the entrance aperture and first mesh, yielding one electron per collision ($\gamma_e = 1$) in the process. The radiative recombination events per second cm^3 is $n_e n_{ion} \alpha_{RR}$ where n_e and n_i are the secondary electron and ion densities respectively, giving 123 cm^{-3}s^{-1} in this scenario. Due to small beam cross-section ($\sim$ 1 mm^2), the cylindrical interaction volume within the RFA between the entrance aperture and the retarding mesh (l $\sim$ 20 mm) reduces the interaction rate by two orders of magnitude. As a result, RR is also not expected to hinder the RFA ion counting capabilities.

Table 4–1: Radiative Recombination rate α_{RR} of Li^+, Na^+ and K^+ for an ion temperature T_{ion} = 400 K.

Element	α_{RR} ($\times 10^{-12}$ cm^3 s^{-1})
Li^+	4.01 [75]
Na^+	2.35 [75]
K^+	3.37 [76]

4.3.2 Neutral Ionization

Unbounded electrons can ionize neutral atoms by collision if their kinetic energies E_e are larger than the ionization potential E_i of the neutral weakest bound electron. Neutrals originate from the vacuum residual. Additional neutrals can be created from electron-ion recombinations but as mentioned above, they can be effectively neglected under the present experimental conditions. If neutral ionization occurs between the central mesh and the collector, the electric field in this region pushes the newly created ions towards the collector and will produce false ion counts.

The TITAN beamline residual gas is principally composed of H_2, H_2O, CO, CO_2 CH_4 (methane), $OC(CH_3)_2$ (acetone) and CH_3OH (methanol) (the last two byproducts of the TITAN UHV cleaning process). Assuming that half of an 1 nA singly charged ion beam collides with the RFA entrance aperture and meshes with an average secondary electron yield $\gamma_e = 1$ and for simplicity assuming a diatomic H_2 residual gas with maximum total ionization cross-section $\sigma_{HI} = 1 \times 10^{-16}$ cm^2 at an electron kinetic energy $E_e = 70$ eV [77], the total hydrogen ionization rate over a 20 mm span is 260 events s^{-1}. The Maxwell-Boltzmann electron energy distribution dependence of the total ionization cross-section [77], the low secondary electron kinetic energy (< 20 eV) [78] and the normally sub-nA beam current for most short-lived isotopes will quickly reduce the ionization rate to undetectable levels.

4.3.3 Secondary Electrons False Ion Counts

Due to the low ion-electron recombination and neutral ionization rates as shown above, the quasi totality of secondary electrons will terminate their lives by colliding with a RFA internal structure, including the collector. If secondary electrons penetrate the region between the outer meshes, the retarding mesh positive potential well V will accelerate them towards it with an quasi equivalent kinetic energy eV. From the retarding mesh effective transparency, some electrons inevitably collide with the grid resulting in further secondary electron emissions via Auger processes [79]. Since the newly acquired kinetic energy of the second generation of secondary electrons is insufficient to escape the retarding mesh positive potential well, they will oscillate within it until eventually being reabsorbed or liberate further electrons due to the mesh effective transparency during each passage. During this oscillatory period, the electrons can interact with incoming ions or neutral as mentioned above but as suggested by the expected low electron densities, no detrimental effects in the ion count are to be expected.

For secondary electrons created from the slits and first mesh, their initial kinetic energy may suffice to overcome the retarding mesh positive potential well, reach the collector and be counted as ion impacts. Even for a low secondary electron emission yield γ_e combined to the three mesh total effective transparency, a sub-nA beam current can produce a sufficient quantity of secondary electrons that can reach the collector and significantly hinder the RFA ion counting capability.

Resulting from all the effects mentioned above, a negative potential is applied to the two outer meshes to minimize unbound electrons coming from either sides from reaching the retarding mesh and for the rear mesh, force secondary electrons emission from the collector back into its surface (see Figure 4–6). The rear outer mesh has a lower potential than the front outer mesh to subdue trapped electron oscillations between the outer meshes, which raises their interaction probability with ions and neutral and prevent secondary electron emissions from the first mesh reaching the collector [80].

The applied potential magnitude of both meshes is determined from the maximum kinetic energy gained during the initial collisional process. Secondary electrons are released through many mechanisms (see Figure 4–5) but can be classified into two categories: the potential electron emission (PEE) and the kinetic electron emission (KEE) [81]. A comprehensive overview

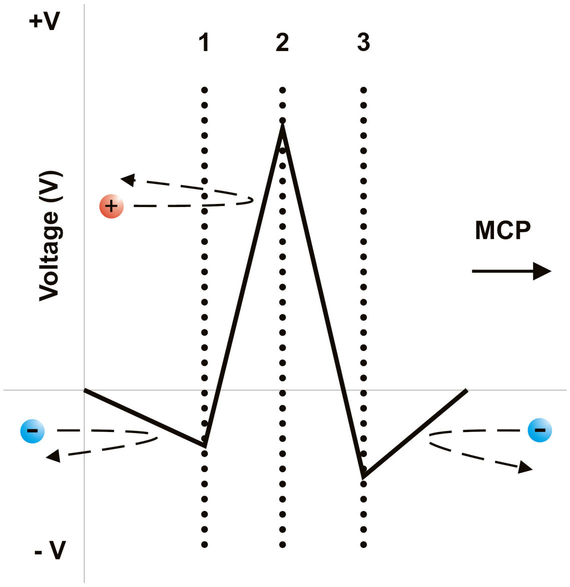

Figure 4–6: Electric potential created by the three mesh configuration. The two outer meshes (1,3) are negatively biased to reflect any secondary electrons away from the central retarding mesh (2), minimizing the chances of neutral ionizations and electron-ion recombination. The rear mesh (3) also reflect any secondary electrons emitted from the collector (MCP) surface caused by ion and neutral impacts. The potential is lower than the front mesh (1) to prevent electrons from oscillating between the outer meshes.

of electron emission can be view in Ref. [68]. From the low beam energetics employed by the TITAN experiment, only a small number of interactions are expected to occur.

4.3.4 Potential Electron Emission

Potential electron emission involves the transfer of the ion potential energy E_i to the valence electrons of the target, resulting in the neutralization of the former with a possible electron emission of the latter. The PEE regime is predominant over KEE for low ion velocities $v_{ion} \leq v_F \approx 25$ keV/amu where v_F is the Fermi velocity in the target or if the ion potential energy exceeds its kinetic energy [68]. The electron emission yield γ_e is independent of the ion velocities under 5×10^5 m/s with respect to the target [81]. Experiments have shown that the electron emission yield γ_e is at most $\sim 2 - 3$ with an average energy of less than 20 eV, usually peaking at a few eV [78]. For the RFA experimental testing, the TITAN experiment provides a singly charged ion beam with a maximum 5 keV beam energy output. Under these constrains, PEE can occur by one of three processes: Auger neutralization (AN), resonance neutralization (RN) and Auger de-excitation (AD) or plasmon-assisted electron emission (PAE) [79].

In Auger neutralization, the ion potential energy E_i excites the target valence electrons, leading one valence electron to tunnel through into the ion atomic ground state. The energy released in the transfer is given to a second valence electron, which if sufficiently energetic can overcome the target surface potential barrier and be ejected into the continuum. AN occurs only if the potential energy E_i is at least twice as large as the target work function ϕ.

$$E_{AN} = E_i - 2\phi \tag{4.13}$$

where the excess energy E_{AN} is converted into the ejected secondary electron kinetic energy.

If the target work function is sufficiently low, the resonance neutralization and Auger de-excitation process can occur. The ion is again neutralized by a target valence electron but occupies an excited state, with the excited state energy larger that the target work function ϕ. The excited electron interacts with a second valence electron, leading either (1) the latter to be ejected from the surface and the former demoted to a lower bound state or (2) the latter is captured to a ground state and the former ejected [82]. The maximum secondary electron kinetic energy from RN-AD process is [83]

$$E_{RN-AD} = [E_i(nl) - E_f(nl)] - \phi \tag{4.14}$$

where $E_i(nl)$ and $E_f(nl)$ are the neutralizing electron initial (excited) and final (ground) energy with principal quantum number n and azimuthal quantum number l.

The third mechanism is the plasmon-assisted electron emission . In a quasi-free electron metal, upon ion neutralization, its liberated potential energy E_i can excite a plasmon, a quantum of the free gas electron density oscillations, if $E_i > E_p = \hbar\omega = \hbar \left(\frac{ne^2}{\varepsilon_0 m}\right)^{1/2}$ where $\hbar$ is the reduced Planck constant, e and m are the electron charge and mass respectively, ε_0 is the permittivity of free space and n is the free-electron density [84]. The plasmon subsequently decays via the mechanism of interband transition, which can lead to electron ejections. The maximum secondary electron kinetic energy is [78]

$$E_{PAE} = \hbar\omega - \phi \tag{4.15}$$

4.3.5 Kinetic Electron Emission

Kinetic Electron Emission (KEE) is the transfer of the ion kinetic energy to the target valence electrons by binary collision. The excited electrons proceed to migrate towards the target surface before escaping into the vacuum. To occur, a minimum kinetic energy transfer is necessary to overcome the target work function ϕ. From the free electron gas model, the maximum energy transfer T_M during a binary collision is [82]

$$T_M = 2m_e v_{ion}(v_{ion} + v_F) \tag{4.16}$$

where v_F is the Fermi velocity in the target, v_{ion} is the ion velocity and m_e is the electron mass. By equating the maximum energy transfer T_M to the target work function ϕ, the ion threshold velocity v_{ion}^{th} is extracted as [68]

$$v_{ion}^{th} = \frac{v_F}{2}\left[\sqrt{1 + \frac{2\phi}{m_e v_F^2}} - 1\right] \tag{4.17}$$

Since the efficiency of electron-electron interactions is higher for heavy ions due to the electron cloud's compression during the collision, the maximum energy transfer T_M will be higher than calculated in Equation (4.16), cumulating in a lower ion threshold velocity v_{ion}^{th} [81].

For ions exceeding the velocity threshold and assuming that the target electronic stopping power $\frac{dE_e}{dx}$ is quasi-constant along its surface electron escape layer $\delta \sim 2nm$, the electron yield γ_e can be given by [81]

$$\gamma_e = C\frac{\delta}{J}\frac{P}{\cos(\theta)}\left(\frac{dE_e}{dx}\right) \tag{4.18}$$

where P is the fraction of electrons moving towards the surface of the target, J is the average required energy to create an electron, θ is the ion incident angle to the target surface normal and C is an ion species-dependent constant. By definition, $C = 1$ for protons whereas $C \approx 0.5$ for He and $C \approx 0.3$ for heavy ions [85].

4.4 Ion Counting

Ions that pass through the three meshes subsequently collide with a collector to be counted. Due to the low current density for most short-lived isotope beams in the TITAN experiment, a MCP was selected as the collector due to it sensitivity at low counts and signal amplification. Each impact releases a cascading electron avalanche, amplifying the single charge into a current pulse. The pulse is sent to an preamplifier for further amplification before reaching a multi-channel scaler (MCS) to be counted. Due to the limited active detection area inside the MCP acceptance area, some ions will collide with the MCP surface instead of the multiplier tubes. Secondary electron emission from the surface is thus expected but the negative potential gradient between the MCP surface and the rear mesh inhibit this by forcing them back into the surface.

An automated software program was developed to enable a smooth stepwise control of the applied voltage on the central meshes while counting ion impacts during a predetermined finite time length. The ion counts are plotted on a graph as a function of the central mesh voltage and the data are saved for later offline data analysis. A detailed overview of the RFA program can be found in Appendix .

4.5 Determination of Energy Spread

For an ion beam energy distribution $N(E)$ with kinetic energy E, the ion counts for a pulse beam or the current I for a continuous beam at an applied retarding voltage V is given by

$$I(V) = \int_{qV}^{E_{max}} N(E)dE \tag{4.19}$$

where E_{max} is the maximum beam energy and q is the ion charge state. The energy distribution $N(E)$ is extracted by differentiating Equation (4.19) with respect to E

$$\frac{dI}{dE} = -N(E) \tag{4.20}$$

The ion beam longitudinal kinetic energy spread is obtained from the full width at half maximum (FWHM) of the derivative curve distribution $\frac{dI}{dE}$. During confinement inside the ion traps in the TITAN experiment, the bunched charged particle energy distribution will relax towards a Maxwell-Boltzmann energy distribution if given sufficient time. For calculation simplicity, a Gaussian energy distribution profile is otherwise assumed to a good approximation.

$$N(E = qV_0) = A \exp\left(-\frac{(V - V_0)^2}{2\sigma^2}\right) \tag{4.21}$$

where qV_0 is the average beam longitudinal kinetic energy, σ is the standard deviation and A is the maximum ion count. This allows for a Gaussian fit to be performed on the data to obtain both the FWHM and the average beam energy. The FWHM and σ are related as

$$FWHM = 2\sqrt{2\ln 2}\sigma \tag{4.22}$$

The RFA experimental energy resolution is obtain by dividing the FWHM by the beam energy.

$$\frac{\Delta E}{E} = \frac{FWHM}{qV_0} \tag{4.23}$$

To avoid introducing a non-essential step in determining FWHM from the energy distribution $N(E)$ and consequently enlarging the energy resolution error, a modified cumulative Gaussian distribution function was determined by deriving the Gaussian energy distribution profile (Eq. (4.21)) by Equation (4.20) to fit directly onto the observed ion count curve I.

$$I(V) = A\left(1 - erf\left(\frac{V - V_0}{\sigma\sqrt{2}}\right)\right) \tag{4.24}$$

where $erf(z) = \frac{2}{\sqrt{\pi}}\int_0^z e^{-t^2}dt$ is the error function. This step is vital due to the low ion count expected for some short-lived isotope beams. For each voltage step scan of the RFA, the uncertainty for N counts is $\sqrt{N}$, resulting in large random fluctuations at low ion counts. Consequently, extracting the FWHM from the first derivative of the ion count curve is next to impossible due to the rapidly fluctuating curve profile even when using smoothing techniques.

Better statistics can be acquired by using a longer time interval per voltage step but at the cost of greatly increasing the scanning time.

The RFA measured energy spread will be larger than the actual beam energy spread due to the various errors presented in section 4.2. These errors must be taken into account when designing a RFA where the energy resolution error should be smaller than the expected ion beam longitudinal energy spread. Additionally, the voltage steps performed by the program should be small enough to allow sufficient data points along the cumulative Gaussian curve to allow proper fitting of the data but not at the cost of significantly increasing the required time to perform a scan. This is also increases the sensitivity to changes in the energy spread at difference beam parameter settings.

Numerical simulations software such as SIMION [86] can predict the RFA energy resolution for comparison with the theoretically determined errors. In addition, it can simulate various beam properties that the RFA could encounter during its runs.

CHAPTER 5
TITAN RFA Design, Construction and Expected Energy Resolution

The TITAN RFA development follows a set of design requirements imposed by the TITAN experiment. A computational model was created to aid during the RFA assembling and installation in the TITAN beamline. Computational simulations were performed to compare the RFA energy resolution with the theoretical energy resolution obtained from the various errors described in section 4.2. After completing a first series of measurements, minor modifications were done to the RFA to improve its energy resolution and structural integrity.

5.1 Design Requirements for the TITAN RFA

The TITAN RFA principal requirement calls for an energy resolution error $\Delta E/E \approx 10^{-3}$ or equivalently, an energy spread error less that 1 eV for a 1 keV beam energy. This restriction results from an RFQ computational simulation previously performed with SIMION [86] where the extracted ions energy spread is approximately 2 eV for a 2.5 keV beam [41] and from the theoretically calculated CPET extracted ions energy spread ($\sim$ 1 eV/q) [49]. Because both the RFQ and CPET energy spreads are smaller than the EBIT energy spread ($\lesssim$ 50 eV/q) [48], this requirement will permit the TITAN RFA to measure the energy spread for any ion traps.

The TITAN RFA installation into the beamline places a second design restriction. The beamline entry ports are mainly a series of four-way 8 inch diameter crosses (see Figure 6–2). These ports enable the installation of various instrumentations, in addition to beam steering electrodes and turbopumps, to perform a variety of beam parameter measurements. Since the ports lie either along the vertical or horizontal axis with respect to the TITAN platform, the TITAN RFA must function in any given orientation. Furthermore, due to the MCP measurements' destructive nature, the TITAN RFA must be retractable from the beam when offline, allowing an uninterrupted beam to pass through.

With four ion traps in the TITAN experiment, the TITAN RFA must be easily transferable to any available beamline port, without compromising any installed devices within the vicinity, during removal and installation.

Finally, because both the RFQ and EBIT can be operated in either a pulsed or continuous beam mode, the TITAN RFA will need to function independently of the beam type selected.

5.2 RFA Design & Construction

Side and front cut view drawings of the TITAN RFA are shown in Figures 5–1 and 5–2 respectively. Machining of all parts was performed by the TRIUMF machine shop and assembly of the RFA was done by myself. The main body is composed of a thin cylindrical stainless steel shell which supports all the RFA internal components (see Figure C–1 in Appendix C).

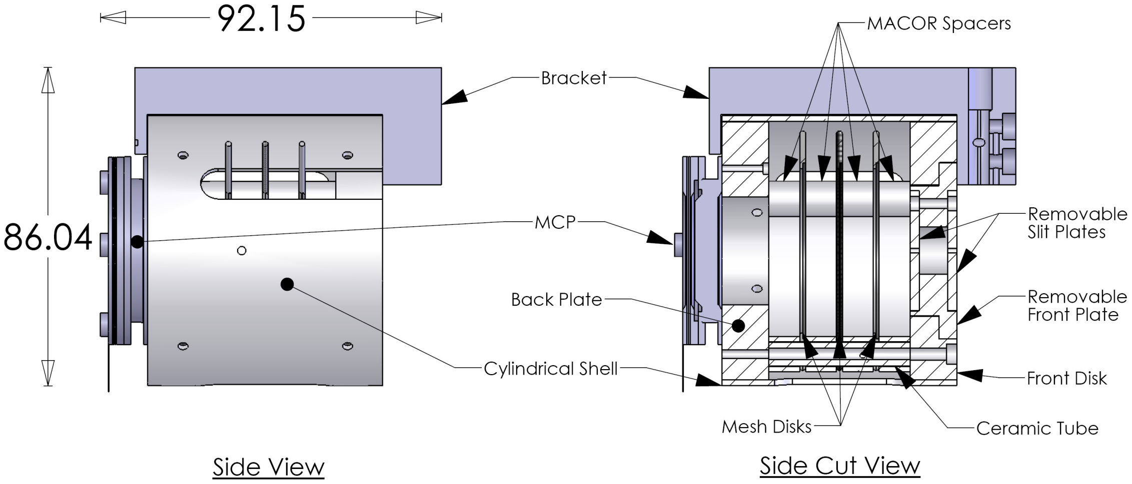

Figure 5–1: Side view (Left) and side cut view (Right) drawings of the TITAN RFA. The incoming ions enter from the right and first pass through two slits to limit the beam divergence. The beam proceeds through the three meshes where their longitudinal energy profile is filtered. Ions that successfully pass through then reach the MCP where they are converted into an electrical pulse, which is sent to an electronic counting device.

Inside and at opposite ends of the cylinder are two thick stainless steel disks. The front disk (see Figure C–2), exposed to the incoming beam, is designed to allow the installation and removal of a small face plate (see Figure C–8), to which different size circular slits (see Figure C–9) can be installed. The rear disk (see Figure C–3) is used as a mounting point for the MCP. The rear central opening diameter matches the MCP acceptance area diameter. The disks are also used as mounting points for a stainless steel bracket (see Figure C–4), which attaches the RFA body to a retractable linear manipulator rod (see Figure 6–3).

In between the two disks, three long ceramic tubes (see Figure C–5) with either end resting on the disks' inner faces, are each secured in place with a long screw slid through a series of holes in the front disk and into the ceramic tubes, reaching the back plate. The ceramic tubes are equally spaced by 120° along a circle of radius 27.9 mm centred along the cylinder axis. These ceramic tubes support both three thin disks with a mesh, which are used to create the potential barrier for the incoming ions and twelve MACOR spacers (see Figure C–6), which are placed between each disk and the end plates. The MACOR spacers are composed of a proprietary machinable glass-ceramic compound and are designed to slide on the ceramic tubes. They are kept in place by the clamping force between the disks and end plates. The high dielectric strength of MACOR (40 kV/mm) avoids any possible electrical discharge between the disks through the spacers. Similarly, the ceramic tubes electrically insulate ($\sim$ 10 kV/mm) the high voltage disks from the internal support screws.

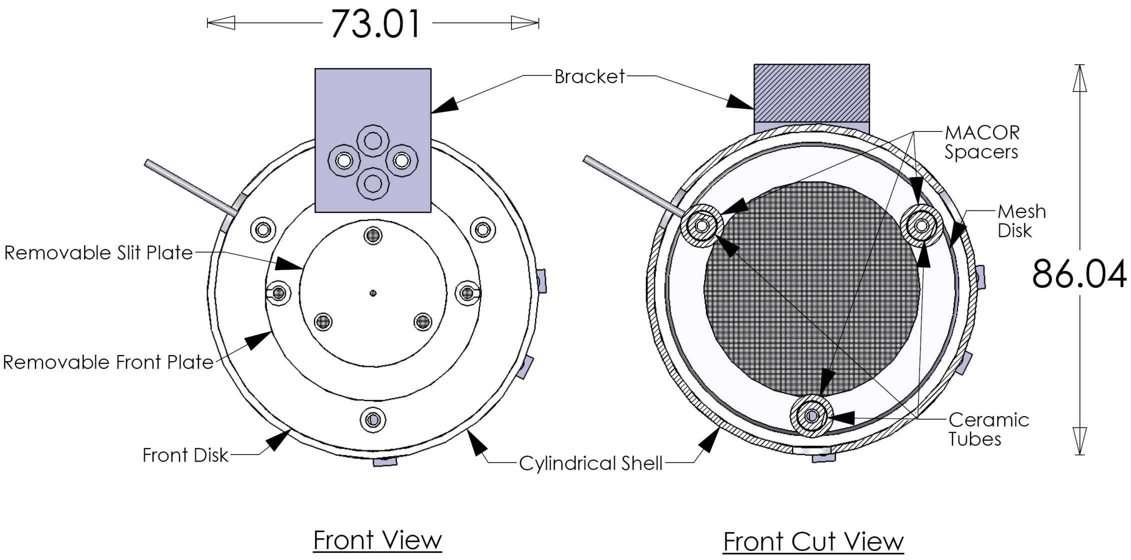

Figure 5–2: Front view (Left) and front cut view (Right) drawings of the TITAN RFA.

The three identical thin disks are subdivided into three parts; a thin stainless steel ring, a very fine mesh across the inner opening and a short electrode stub (see Figure C–7). The ring's outer edge is rounded to remove any sharp burs that may induce electrical discharges. Three holes are machined through the ring and separated by 120°. The hole locations match the ceramic tube positions and the hole diameter is slightly larger than the ceramic tube diameter. This enables the disks to be slid onto the ceramic tubes and kept in place by the clamping force between the MACOR spacers and the disks. The stubs' axis of symmetry are aligned with the normal of one of the rectangular vents to insure the stubs exits the cylindrical shell through the vents. Push-on connectors are slid onto the end of the stubs and a Kapton wire is screwed to the connectors. The Kapton wire consist of a thin silver plated copper wire inside an insulated Kapton layer with a 10 kV breakdown DC voltage and outgassing rate of 1×10^{-10} Torr. The Kapton wires are connected to SHV electrical feedthroughs on a 2.75 inch flange, allowing for an electrical connection between the RFA and the beamline exterior (see Figure 5–3)

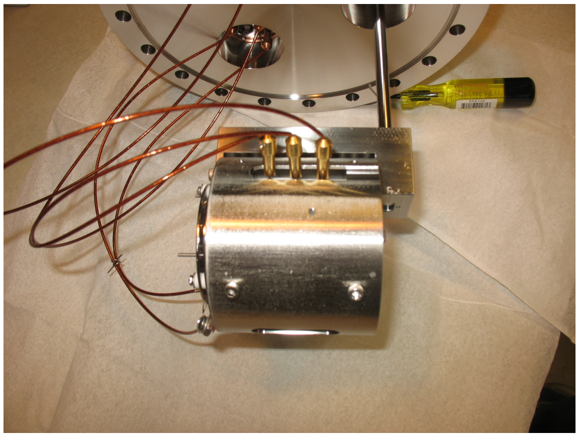

Figure 5–3: Electrical connections between the SHV feedthrough connectors flanges and the RFA's mesh disks are done using Kapton wires with push-on connectors. Uninsulated ring terminals are used to connect the Kapton wires to the MCP electrodes.

The mesh is positioned across the ring main opening and secured by clamping it between a circular inner step along the ring inner radius and a smaller ring designed to fit into it. After carefully stretching the mesh to insure a smooth flat surface, the smaller ring is spot-welded to the main ring and the excess mesh is removed. The mesh is composed of stainless steel, insuring a good electrical connection with the stainless steel ring.

5.3 Analytical Energy Resolution

The maximum allowable energy resolution is determined by the mesh energy resolution errors, the beam transverse kinetic energy and the lensing effect near apertures. After selecting a suitable mesh, the beam properties must be verified to ensure a proper operation with the mesh. This includes particle charge suppression, determined by the Debye length λ_D and the beam space-charge limit.

5.3.1 Energy Resolution of Mesh

In section 4.2, the mesh's contribution to the RFA energy resolution was discussed. Both the focusing effect ($\Delta E/E|_f$) and the non-uniformity of the electric field across the mesh ($\Delta E/E|_{open}$) are dependent on the wire diameter d, the spacing s between them and the mesh separation l. By selecting the appropriate values for d, s and l, the mesh energy resolution can be minimized.

A series of experiments were previously conducted by Sakai [63] comparing the three mesh RFA energy resolution as a function of d, s and l for $0.1 \lesssim d/s \lesssim 1$. In his paper, both the theoretical energy resolutions from Hanson [62] for $0.03 \lesssim d/s \lesssim 0.1$ and Sakai were normalized by $s/2\pi l$ and compared. In both cases, the normalized energy resolution covers the same range of values between 1 - 1.5. From Equations (4.3) and (4.8), the energy resolutions are proportional to s/l. Since the maximum size in l is physically limited by the vacuum chamber dimensions, the resolution can only be greatly reduced by decreasing s. For meshes with small s values, d is appropriately of the same magnitude. As a result, the ratio $d/s \sim 1$ falls within the boundary of Sakai's formulas. From his results, the lowest energy resolution is achieved by using a mesh with $d/s \lesssim 1$ and largest mesh spacing l.

Because of the limited cross-sectional area inside an 8 inch cross, a mesh spacing of $l = 10$ mm was selected. This allows for sufficient spacing between the disks without the risk of electrical sparking between them while minimizing a compromising of the RFA energy resolution [64]. Furthermore, the spacing l can be increased at any future point in time, if deemed necessary, by replacing the MACOR spacers by longer versions between the mesh disks and shorter versions between the mesh disks and the end disks.

A 635 wires per inch (wpi) square mesh wire cloth was chosen. The mesh possesses the smallest wire spacing $s = 0.01651$ mm (0.0065 in.) available with a wire diameter $d = 0.02169$ mm (0.0085 in.), while preserving an acceptable 38.0% effective transparency. The three meshes total effective transparency is 5.5%. However, the mesh ratio $d/s \cong 1.3$ exceeds the theoretical formulas range described by Sakai. The results obtained from this ratio cannot be guaranteed to be very precise. Only through the use of computational simulations can the mesh energy resolution be confirmed. Using these values, the mesh theoretical energy resolutions (Equations (4.3) and (4.5)) are

$$\left.\frac{\Delta E}{E}\right|_{open} = 8.7 \times 10^{-5} \tag{5.1}$$

$$\left.\frac{\Delta E}{E}\right|_{f} = 1.6 \times 10^{-4} \tag{5.2}$$

5.3.2 Transverse Kinetic Energy Resolution

For the TITAN RFA, limited spacing inside the vacuum chamber limits the slit separation d. A distance $d = 12.7$ mm was selected early on in the design process as a consequence. The divergence can thus only be decreased by reducing the aperture radius r

From initial requirement in section 5.1 and from Equations (4.3), (4.5), (4.6) and (4.7), the radius must be smaller than $r < 0.2$ mm. This solution is not deemed acceptable since it would significantly reduce the beam current entering the RFA, requiring a dramatic increase in data acquisition time necessary to obtain sufficient ion counts for analysis. A value of $r = 0.635$ mm was selected, which results in a energy resolution of

$$\left.\frac{\Delta E}{E}\right|_{\perp}^{slits} = 10^{-2} \tag{5.3}$$

During the two test runs, the TITAN beamline imposes some geometric constrains on the beam, resulting in a tighter maximum beam divergence upper bound than provided from the

RFA collimating slits (Equation (5.3)). An Einzel lens with inner radius $r = 34.29$ mm is situated a distance $d = 766.4$ mm in front of the RFA front slit (see Figure 5–4). In conjunction, the Einzel lens and front slit act as a crude double slit. In this scenario, the beam divergence energy resolution error is

$$\left.\frac{\Delta E}{E}\right|_{\perp}^{Einzel} = 2 \times 10^{-3} \tag{5.4}$$

In practice, the beam divergence is not expected to approach the Einzel lens' inner surface but remains confined within a beam radius of $\lesssim 7$ mm [87], resulting in a smaller beam divergence than imposed by Einzel lens slit geometry. For future operations, a slit system with smaller divergence, independent of the beamline inner geometry, will be required.

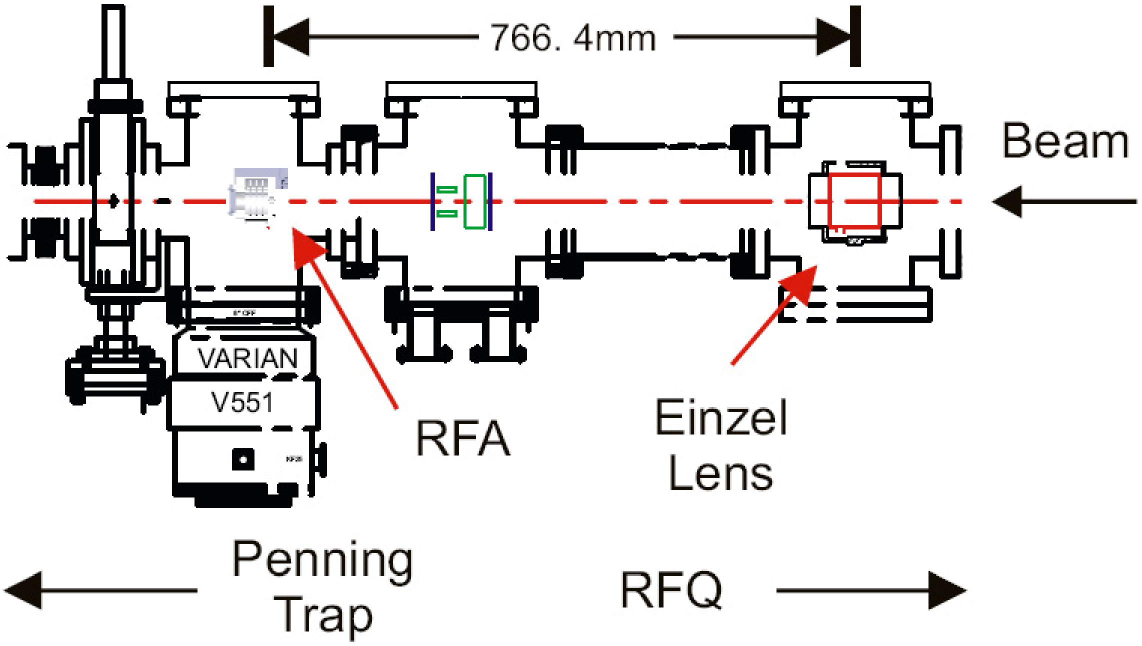

Figure 5–4: Section of TITAN beamline where the TITAN RFA was installed for experimental testing. The Einzel lens situated upstream from the RFA places an upper limit on the maximum beam divergence.

5.3.3 Total Energy Resolution

The RFA total energy resolution is the summation of the mesh energy resolution errors (Equation (5.1) and (5.2)), the beam divergence beam error (Equation (5.4)) and the lensing effect error (Equation (4.10)). The last is a function of the beam energy V_0 and the electric field $\boldsymbol{E}$ created from the front mesh potential. For the beam energy used in the TITAN experiment, the lensing effect will be negligible smaller in relation to the other errors, even for large negative potential and thus can be neglected.

$$\begin{aligned} \left.\frac{\Delta E}{E}\right|_{total} &= \left.\frac{\Delta E}{E}\right|_{\perp} + \left.\frac{\Delta E}{E}\right|_{open} + \left.\frac{\Delta E}{E}\right|_{f} + \left.\frac{\Delta E}{E}\right|_{lens} \\ &= 2.2 \times 10^{-3} \end{aligned} \tag{5.5}$$

The resulting RFA total energy resolution is larger than stipulated by the initial design ($< 10^{-3}$) due mainly to the beam divergence. Reduction of its contribution would require increasing the slit separation. For example, preserving both r and the mesh dimensions, the slit separation d would need to be a minimum 46.3 mm in order to satisfy $\Delta E/E < 10^{-3}$.

5.4 Numerical Energy Resolution

Two numerical simulations were performed for the TITAN RFA; one to evaluate the mesh energy resolution errors due to its large d/s mesh ratio outside the boundaries analyzed by Sakai [63] for a three grid RFA and a second to observe ion trajectories inside the TITAN RFA under various experimental conditions expected in the TITAN experiment. The computer program SIMION 8 [86] was employed in both cases.

5.4.1 Energy Resolution of Mesh

A parallel three-meshes simulation using the TITAN RFA physical dimensions was created. The two outer meshes were grounded and all three meshes had perfect transparency. Variations in the electric field near the mesh surfaces between the physical grounded outer meshes and the simulations are negligible within the experiment energy sensitivity whereas a second instance was created to duplicate the non-homogenous retarding mesh electric field with a high fidelity. The second instance consists of a small three wire sided cross-section of the 635 wpi mesh to permit a factual mesh simulation with minimal computational memory. As incoming ions were within a preselected distance normal to the retarding mesh surface, they are transferred to the second instance and promptly interact with the mesh cross-section before being returned back to the initial instance. The electric potentials at the instances edges were matched to insure electric field continuity. All ions passing through the retarding mesh were counted and plotted as a function of the retarding potential V.

The ion focusing-induced energy resolution error $\Delta E/E|_f$ was measured as the retarding voltage difference at peak ion count and when the ion counts decreases back to the ion count expected from the grounded mesh effective transparency, divided by the beam energy qV_0. The mesh openings-induced energy resolution error $\Delta E/E|_{open}$ was measured as the retarding voltage difference between the second point mentioned above and when the ion count reaches zero, divided by the beam energy.

Two simulations using a 1 mm radius beam composed of 10,000 ^{6}Li$^+$ ions with energies of 1 and 4 keV were performed. The beam energies selected represent the extrema that the TITAN RFA will be exposed to during experimental testing. No other element available from the TITAN ion source was simulated due to the mass independence of the energy spread measurements with the RFA. The results for 1 and 4 keV beam can be viewed in Figures 5–5(a) and 5–5(b) respectively.

Both Figure 5–5(a) and 5–5(b) show that the mesh introduces an energy resolution error in the RFA as mentioned in section 4.2. The focusing effect is very noticeable as a sharp count increase, peaking around $\sim$ 4,600, above the average ion count of 2,800, a 64% increase. The average ion count observed is below expected ($\sim$ 3,800) from the grounded mesh effective transparency (38.0%). This is due to the small sampling area performed in the simulation, in addition to the simulation resolution limitations. From rounding, the wire diameter d and wire spacing s in the simulation were changed from 0.02169 to 0.02146 mm and 0.01651 to 0.01684 mm, a difference of 1.1% and 2% respectively. From the relative uncertainty errors on both

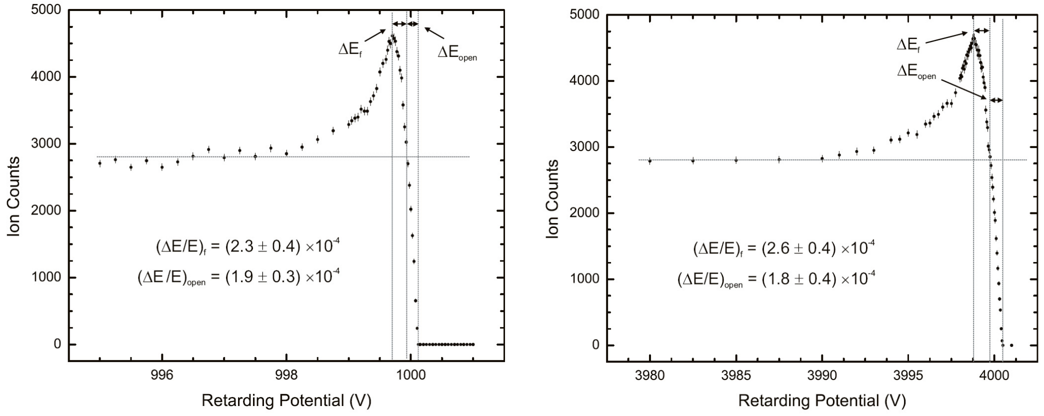

(a) 1 keV ^{6}Li$^+$ (b) 4 keV ^{6}Li$^+$

Figure 5–5: 635 wpi mesh simulation of the ion counts as a function of the retarding voltage for a monoenergetic ^{6}Li$^+$ beam of (a) 1 keV and (b) 4 keV. The energy resolution errors introduced by the ion focusing ($\Delta E/E|_f$) and mesh openings ($\Delta E/E|_{open}$) are easily noticeable.

$\Delta E/E|_f$ and $\Delta E/E|_{open}$, the effect of these deviations can be assumed to be contained within the errors.

The energy resolution errors show no discernible relationship with the beam energies employed outside of the error bars (see Table 5–1), as assumed by the beam energy independence of the energy resolution formulas (see Equations (4.3), (4.4) and (4.5)) derived by Sakai [63] and Hanson [62].

Table 5–1: Energy resolution errors from the ion focusing effect $\Delta E/E|_f$, the mesh openings $\Delta E/E|_{open}$ with total $\Delta E/E|_{total}$ using a simulated 635 wpi mesh with 1 keV and 4 keV ^{6}Li$^+$ beams.

Beam Energy (kV)	$\Delta E/E\|_f$ $\times 10^{-4}$	$\Delta E/E\|_{open}$ $\times 10^{-4}$	$\Delta E/E\|_{total}$ $\times 10^{-4}$
1	2.3 ± 0.4	1.9 ± 0.3	4.2 ± 0.4
4	2.6 ± 0.4	1.8 ± 0.4	4.4 ± 0.4

Comparing the simulated energy resolution error values to the theoretical values in Section 5.3.1, the simulated $\Delta E/E|_f$ and $\Delta E/E|_{open}$ values are approximately 30 to 43% and more than 100% larger than the theoretical values respectively. The total simulated energy resolution error from both effects is approximately 70 to 78% larger than the theoretical sum. Whereas these increased values would normally result in a diminished RFA energy resolution, the transverse energy resolution error contribution from the TITAN RFA still remains significantly larger, yielding a minute total RFA energy resolution increase from 2.2 to 2.4 $\times 10^{-3}$

5.5 Particle Suppression

As the ions travel along the beamline, each ion electric charge will screen out the electric fields from other sources within a small radius around itself. As the ion-ion distance decreases, the screening effect starts to overlap and mask any ions located in this region. This effect would partly negate the electrostatic potential barrier created by the RFA retarding mesh, allowing ions with normally insufficient kinetic energy to pass through and be recorded with a high kinetic energy value than it would have be otherwise. This critical length is the Debye length λ_D and is given by [88]

$$\lambda_D = \left[\frac{\epsilon_0 k_B T}{q} \frac{a^2}{I} \left(\frac{2E}{m} \right)^{1/2} \right]^{1/2} \tag{5.6}$$

where m and q are the ion mass and charged states respectively and I, a and E are the beam current, radius and energy respectively.

For proper operation, the Debye length must be larger than the "mesh hole radius" $s/2 < \lambda_D$ [80]. In the worst-case scenario, the TITAN RFA with mesh openings $s = 0.01651$ mm measuring a 1 keV $^{239}\mathrm{U}^{92+}$ beam of $I = 1$ μA current, radius $a = 1$ mm and ion temperature $k_B T = 10$ eV will have a Debye length of 0.9 μm. Clearly, this suppression effect will not occur in the RFA under any expected experimental condition that the TITAN experiment will experience for the foreseeable future.

5.6 Space Charge Limit

For proper RFA operations, the ion beam cannot exceed the Child-Langmuir current density to avoid being space-charge current limited. At current densities above this limit, the ion bunch space charge start to affect the ion beam kinetic energy distribution by Coulomb ion-ion repulsion. This result in instability growth and beam quality degradation. The Child-Langmuir law [89] is expressed as

$$J = \frac{\epsilon_0}{9\pi}\left(\frac{2q}{m}\right)^{1/2}\frac{V^{3/2}}{d^2} \tag{5.7}$$

where q and m are the ion charged state and mass, V is the potential difference between two parallel meshes and d is the mesh separation. In the worst case scenario, the TITAN EBIT is able to produce He-like Uranium ($^{92}U^{+90}$) [46]. For a 5 keV U^{+90} beam entering the TITAN RFA, the Child-Langmuir law gives $\sim$ 7.82 nA/mm^2. After considering current density losses due to the first outer mesh effective transparency, the upper bound increases to $\sim$ 20.6 nA/mm^2. This value is not attainable due to the low production rate for U^{+90}, caused by charge-exchange, dielectronic and radiative recombinations with surrounding ions of lesser changes and stray electrons inside the EBIT.

The short-lived isotope low production rates and transmission losses from each ion trap will decrease the ion beam current. Whereas a 1 nA current is $\sim 6 \times 10^9$ ions s^{-1}, ISAC yields of less than $\sim 10^5$ ions s^{-1} are often observed [90], which preclude transmission losses to and in the TITAN experiment. In addition, for any ion trap off-line testing, the TITAN ion source, the EBIT gas injection system and RFQ can be controlled to give a reduced ion beam current if necessary.

CHAPTER 6
Experimental Setup

The TITAN RFA was tested on two separate occasions using the TITAN ion source, the RFQ and the main TITAN beamline. The RFA was installed by substituting a steerer electrode assembly inside a four-way cross located in front of the Penning trap. A program was written for the electronic automated control system used by the RFA setup. From the user's initial scanning parameters, the program performs automated scans with the RFA by progressively varying the retarding mesh potential, acquiring the resulting ion counts and saving the data for later offline analysis. Data analysis software was employed to extract the ion beam longitudinal energy spread and observe behavioural variations under different beam parameters.

6.1 TITAN Ion Source

A HeatWave Labs Aluminosilicate ion source model 101142 [91] is employed as the TITAN principal ion source (see Figure 6–1). The source consists of a thin cylindrical molybdenum shell with three rhenium support struts equidistantly separated by 120° along the outer shell and extending 12.7 mm below the edge. Inside, a non-inductive molybdenum coil potted in an alumina ceramic (Al_2O_3) occupies most of the lower body. In thermal contact above the alumina, an extremely porous tungsten disk with a thin deposited β-Eucryptite ($LiAlSiO_4$) layer acts as the ion emitter. The β-Eucryptite is partly melted to allow the tungsten disk to absorb it. The ceramic acts as an indirect heater element for the ion emitter. As a current flows through the molybdenum wire, the ceramic and subsequently the ion emitter heats up. This process leads to ionic thermionic emission [92] embedded within the ion emitter matrix. The ion source emits mainly ^{6}Li and ^{7}Li, with lesser quantities of ^{23}Na, ^{39}K and ^{41}K. The source has current densities of 1-10 mA/cm^2 for operating temperatures between 950 °C and 1,100 °C. The ion current density is controlled by varying the heating element temperature via the applied electric current. The ion temperature at the ion emitter surface is $k_B T_s \sim 0.1$ eV.

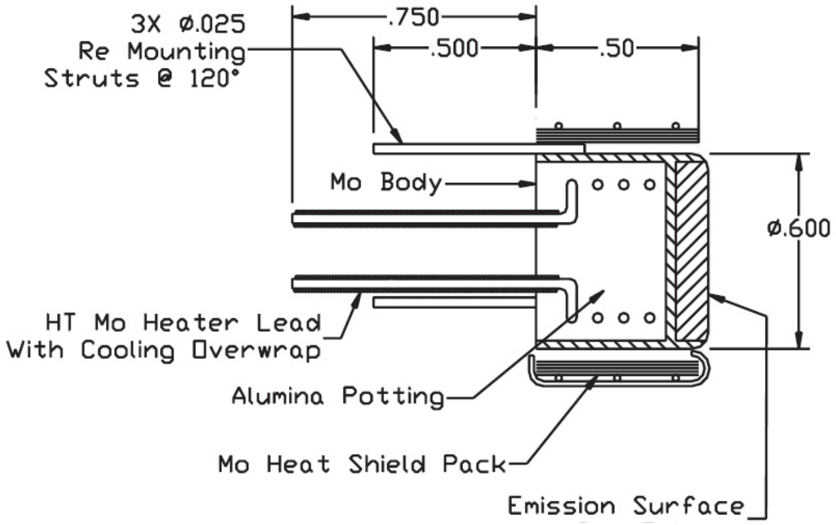

Figure 6–1: Schematic of HeatWave Labs Model 101142 Alkali Ion Source. Taken from [91]

6.2 TITAN Beamline

The beamline is composed of short 8 inch diameter tubes sections interconnected at irregular intervals by four-way crosses. Each cross contains either two 8 inch or 10 inch diameter access ports with either a beam profile monitor, a beam steerer elements or a Varian Turbo-V 551 Navigator turbomolecular pump (see Figure 6–2). The beamline provides a continuous vacuum between the TITAN ion source, RFQ and the Penning trap. From the TITAN ion source, a steady current ion beam is extracted and directed into the RFQ for cooling, bunching and trapping. A periodic trigger signal releases the trapped ions by lowering the rear trapping potential where they proceed down the main beamline until encountering the RFA. The trigger frequency, electrodes and vacuum system along the TITAN beamline, ion source and RFQ, are controlled via a software environment called EPICS (Experimental Physics and Industrial Control System) [93] specially configured for the TITAN experiment [94].

6.3 RFA Setup

The RFA is mounted as shown in Figure 6–3. A modified 8 inch flange with three 2.75 inch tapped reducer flange interfaces secures respectively a 5 inch travel linear manipulator and two 2.75 inch four-SHV feedthrough connectors flanges (see Figure 6–4). The modified flange acts

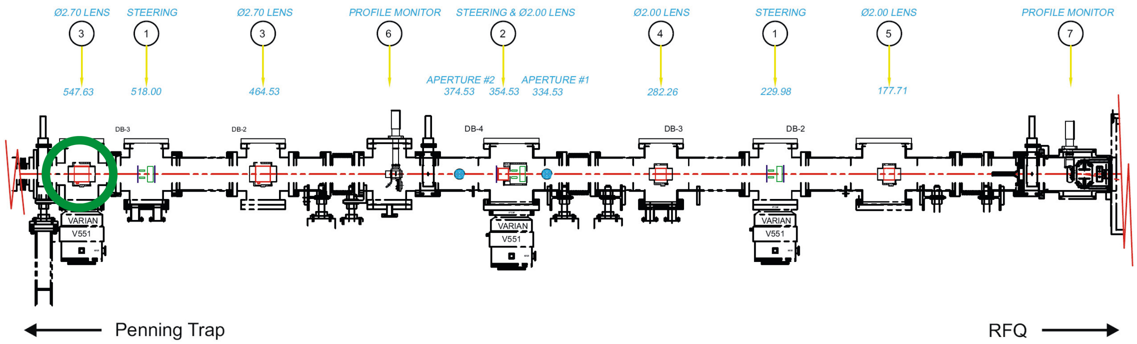

Figure 6–2: Sidecut view of the TITAN beamline horizontal section between the RFQ and Penning Trap. The furthest Einzel Lens to the left (547.63 cm) was removed to permit the RFA insertion into the beamline, marked by the green circle.

as the RFA setup support structure, permitting transferability into any available 8 inch vacuum chamber. When the linear manipulator is fully extended, the RFA axis is aligned with the ion beam and beamline axes (see Figure 6–5). The MCP used is a Photonis APD Model 30 25 MA 12/10/12 D, chosen for its detection qualities with an 25 mm active surface diameter and a minimum 55 % open area.

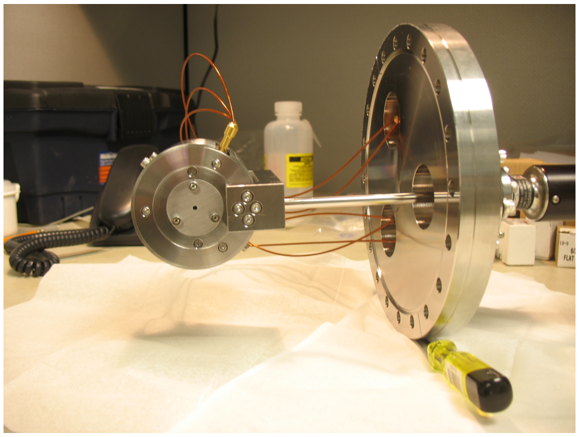

Figure 6–3: TITAN RFA installed on a 5 inch linear manipulator and connected to the modified 8 inch flange. The three meshes and MCP are electrical connected using Kapton wires to two HV feedthroughs flanges on the 8 inch flange

A steerer lens assembly is removed in the first 4-way cross upstream from the Penning trap to allow the RFA assembly be inserted into the TITAN beamline. Before securing the RFA setup

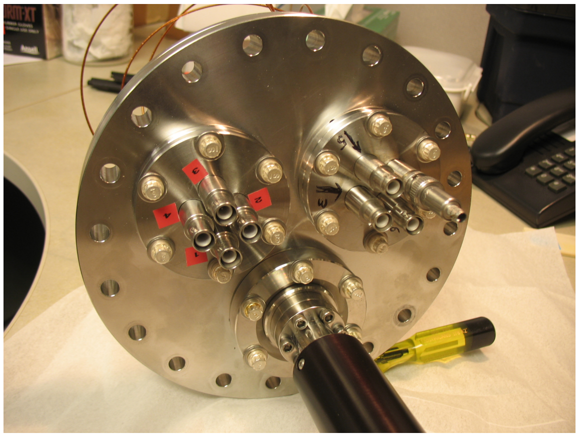

Figure 6–4: Modified 8 inch flange with two 2.75 inch four-SHV feedthrough connector flanges and 5 inch linear manipulator installed.

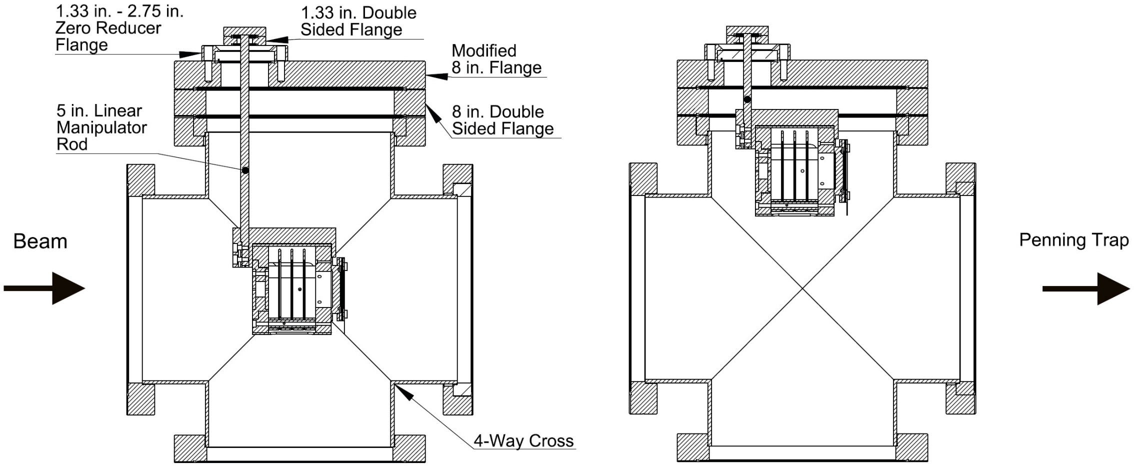

Figure 6–5: Sidecut drawing view of TITAN RFA setup installed in a 8 inch four-way cross. Left: RFA extended into the four-way cross for beam measurements. Right: RFA retracted from beam, enabling an unperturbed flow pass the detector. An 8 inch double sided flange is employed to create sufficient space to fully retract the RFA from view of the incoming ion beam. Electrical connections are not shown.

to the beamline, a current leakage test is performed with the linear manipulator in both retracted and extracted modes.

6.4 Outer Mesh Potentials

From the TITAN ion source available elements (section 6.1), combined with the RFQ beam energy range, the maximum secondary electron kinetic energy can be calculated (section 4.3).

6.4.1 Potential Electron Emission

From the elements provided by the TITAN ion source, the RFQ extracted ion beam energy range and the TITAN RFA material composition, the theoretical maximum secondary electron kinetic energy can be calculated from section 4.3.4 and 4.3.5.

For AN, none of the five elements has a sufficiently high potential energy E_i to overcome the work function of stainless steel ($\phi_{ss} \backsimeq 4.4$ eV) of which the slits and meshes are composed, or Inconel, a nickel-chromium alloy which acts as the electrode connections to the MCP active area ($\phi_{Ni} \cong \phi_{Cr} \backsimeq 4.6$ eV).

For RN-AD, only the lightest three elements can produce secondary electron emission and only if the excited atomic state are above 1s^{2}5s (E_{ex} = 4.75 eV) and 2p^{6}6d (E_{ex} = 4.76 eV) for Li$^+$ and Na$^+$ respectively with respect to their ground atomic states 1s^{2}2s and 2p^{6}3s. Considering the difference between the ground state and the upper atomic state limit for these elements minus the work function, the maximum secondary electron kinetic energy is less than 1 eV.

For PAE, since stainless steel is 50 to 90% iron, the free-electron density of the latter will be employed ($n_{Fe} = 1.7 \times 10^{28}$ m^{-3}) with the resulting plasmon energy $E_{PAE} = 15.3$ eV. However, as in the case of AN, the potential energies E_i of the five elements are insufficient to induce a plasmon excitation.

In conclusion, with perhaps the exception of some weak RN-AD secondary electron emission for Li$^+$ and Na$^+$, the PEE is expected to be suppressed in the TITAN experiment within the energy range delivered by the RFQ and singly charged elements provided by the TITAN ion source.

6.4.2 Kinetic Electron Emission

The maximum kinetic energy transfer T_M from Equation (4.16) to both the stainless steel and Inconel can be obtained from the Fermi velocity of iron $v_f^{Fe} = 0.0066\,c$, of which stainless steel is mostly composed and from nickel $v_f^{Ni} = 0.0062\ c$ and chromium $v_f^{Cr} = 0.0068\ c$ respectively [95]. Due to the proximity of each target element's Fermi velocity, iron will be chosen as a suitable example and the results should be fairly similar for Inconel. In return, the threshold beam energy and ion-stimulated electron emission yield γ_e for each element can be calculated. These are presented in Table 6–1

Table 6–1: Maximum transfer energy T_M, minimum threshold beam energy v_{ion}^{th} and electron yield γ_e for kinetic electron emission on stainless steel target for the elements available from the TITAN ion source with beam energies between 1 and 5 keV.

Element	T_M (eV)	v_{ion}^{th} (keV)	γ_e
$^{6}Li^{+}$	3.8 - 10.8	1.0	0.4 - 1.0
$^{7}Li^{+}$	4.0 - 9.9	1.0	0.4 - 1.0
$^{23}Na^{+}$	2.2 - 5.0	3.8	0.6 - 1.2
$^{39}K^{+}$	1.6 - 3.7	6.5	0.8 - 1.8
$^{41}K^{+}$	1.6 - 3.7	6.5	0.8 - 1.8

As opposed to PEE, the kinetic energy transfer T_M to the valence electrons of the RFA stainless steel structure is sufficiently energetic to overcome its work function ϕ and escape when the beam energy is above the critical threshold value v_{ion}^{th}. As mentioned in section 4.3.5, the actual threshold velocity will be lower than calculated. We can expect to observe KEE for each beam type, regardless of the beam energy employed with perhaps an exception for $^{39}\mathrm{K}^{+}$ and $^{41}\mathrm{K}^{+}$ at low energies (see Table 6–1). The values for γ_e were obtained using Equation (4.18) while assuming $P \approx 0.5$, $J = 0.25$ eV, $\delta = 20$ Å, $C \sim 0.4$ which are typical values for an ion hitting a metal [81]. The electronic energy loss per unit length $(\frac{dE}{dx})_e$ values for the five elements impacting stainless steel at beam energies between 1 and 5 keV were theoretically obtained using TRIM (TRansport of Ions in Matter) [96] which utilizes a quantum mechanical treatment of ion-atom Coulomb collisions. The incident angle $\theta = 0°$ is assumed to be parallel to the target surface, resulting in a lower bound of γ_e [97]. The wires' circular cross-section viewed by the incoming ions will result in higher γ_e values than shown in Table 6–1. After deducting the work function contribution, the freed electrons maximum kinetic energy can reach up to 6.4 eV, with similar results for Inconel while using a 5 keV $^6\mathrm{Li}^+$ beam. The outer meshes' applied negative potentials will then be appropriately matched to repel these electrons.

6.5 Electronic Equipment

A schematic diagram of the TITAN RFA electronic setup is shown in Figure 6–6. The RFA three-mesh disks and the MCP are powered by three ISEG NHQ 205M N24 power supplies. Each power supply has two independent outputs with a 0 - 5 kV range with 1 V steps, selectable polarity and can be remotely controlled via a RS-232 serial port. For high precision measurements of the RFA retarding voltage, an in-house built HV divider box with 1000:1 voltage ratio combined with a Keithley 2700 multimeter/data acquisition were employed. The HV divider provides a low voltage output to the multimeter proportional to the applied high voltage since most multimeters cannot directly measure high voltage. Voltage measurements data can be transmitted via a GPIB (General Purpose Interface Bus) port.

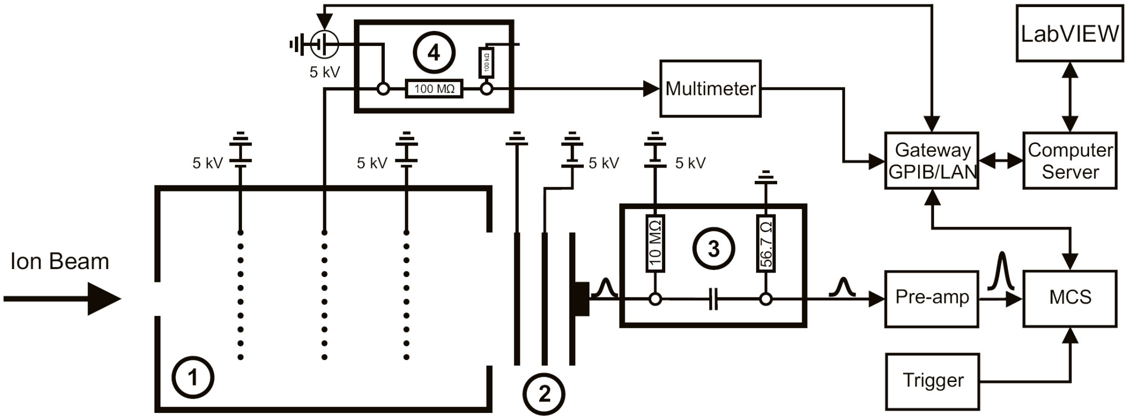

Figure 6–6: Circuit diagram of RFA experimental setup. After the ions pass through the RFA (1) and are detected by the MCP (2), an electrical pulse is sent through a HV junction (3), amplified by a pre-amplifier (Pre-amp) and measured by an multichannel scaler (MCS). The data are sent to a GPIB/LAN gateway before being acquired by the computer server and analyzed by the LabVIEW [98] program. A HV divider box (4) steps down the output voltage to allow the multimeter to measure the voltage.

For each ion impact on the MCP, an electrical pulse is send out from the MCP metal anode towards its power supply. A junction box is placed between the power supply and the MCP to divert the pulses towards a counter at low voltage. Inside, a 10 MΩ resistance between the power supply and the junction redirects the pulse towards the low voltage branch. The pulse subsequently encounters an 0.001 μF HV capacitor where it is transferred through to a low voltage wire before proceeding to an ORTEC 570 fast pre-amplifier for signal gain amplification and finally to a Stanford Research System SR430 multichannel scaler for counting.

To discard dark (false) counts measured by the MCS resulting from thermal noise in the MCP, a 10 mV discriminator voltage level is selected to count only pulses with voltage amplitude above this setting. Approximately 100 dark counts per second are expected from the MCP during normal operations. A LeCroy 222 dual gate generator is used to remotely trigger both the RFQ ion extraction and the MCS data acquisition software. During the data acquisition, the MCS tags each ion with a time stamp and places them into a time bin. The smallest time bin width of 5 ns was selected for good time resolution for TOF analysis and each record has 1k (1024) bins for a total time scan window of 5.12 μs. A short time delay is added to the start of the MCS data acquisition timing due to the ion time of flight between the RFQ ion trap and the MCP and the MCS small time scanning window. The time length is varied manually as a function of the ion mass and beam energy. For each record, the total accumulated ion counts and counts per bin are saved remotely to a computer via a GPIB port for offline analysis.

An Agilent E5810A LAN/GPIB gateway is used to interface the power supply RS-232 serial ports, multimeter and MCS GPIB ports to a remote computer via an Internet Protocol (IP) address on a LAN (Local Area Network) connection. This permits a two-way communication between the computer and each instrument.

6.6 RFA Program

Using the LabVIEW software [98], a RFA data acquisition and control system program was created by Thomas Brunner (see Figure 6–7). A virtual LabVIEW server runs the program, which connects to the LAN/GPIB gateway and communicates to each electronic instrument. From the server IP address, an internet browser on an internet-accessible computer running LabVIEW 8.6.1 and National Instrument VISA 4.3 Run-Time engines can access the server and remotely operate the program. LabVIEW creates a simple graphical user interface (GUI) to allow users to pre-define a set of scanning parameters before running a scan (see Appendix B). The primary parameters of interest are the starting and final retarding voltages, voltage step size, MCS bin width, total bin size and number of records per voltage step.

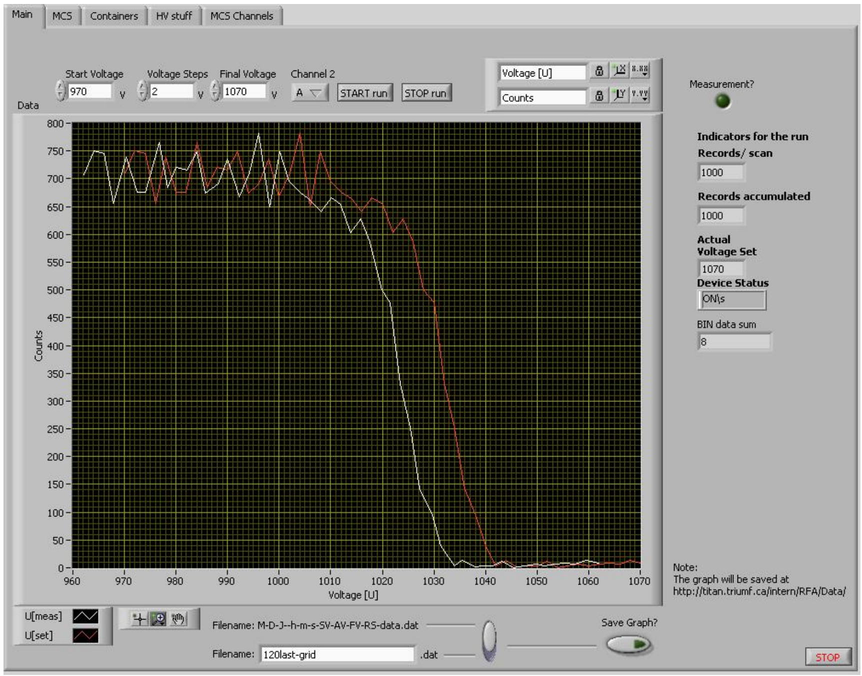

Start Voltage 970 V

Voltage Steps 2 V

Final Voltage 1070 V

Channel 2 A

Indicators for the run

Records/ scan 1000

Records accumulated 1000

Actual Voltage Set 1070

Device Status ON\s

BIN data sum 8

Note:
The graph will be saved at
http://titan.triumf.ca/intern/RFA/Data/

Filename: M-D-J--h-m-s-SV-AV-FV-RS-data.dat

Filename: 120last-grid .dat

Figure 6–7: Sample display of the LabVIEW-designed RFA program. The RFA program allows to pre-set a finite set of scanning parameters and is accessible via an internet-enable computer using an internet browser and LabVIEW and National Instrument VISA Run-Time engines. While acquiring the data, the program plots in real time the ion counts both as a function of the voltage measured by the multimeter and the power supply output.

During a voltage scan, a graphical plot of the ion counts as a function of the retarding voltage is shown in real time. Two piecewise curves represents the retarding voltage setting sent to the power supply and the corrected voltage measurement (see section B.2.1) are plotted. After the scan has been completed, the data is saved in .dat format to a dedicated TITAN server for later analysis. The filename includes a time and parameter settings stamps for easy recovery. The graphical plot can be saved optionally for quick reference.

For offline data analysis of the .dat files, a scientific data analysis software package called Origin [99] is employed. Using Equation (4.24) as the curve template, Origin performs a curve fit for each data file to extract the beam energy V_0 and standard deviation σ to which the longitudinal energy spread $\Delta E_{\|}$ is extracted (Equation (4.23)).

6.7 Electronic Errors

Each electronic equipment used with the RFA has an intrinsic accuracy and resolution error. The HV power supply for the retarding mesh, the HV divider box and the multimeter will impose an error on the measured retarding voltage whereas the error on the ion counts is caused by the multichannel scaler. Each device contribution to either measurement error is discussed below.

6.7.1 Multichannel Scaler

The time accuracy for each ion count timestamp is 1 ns + 20 ppm of bin width and an indeterminacy of 2.5 ns with respect to trigger input. Because the bin width is 5 ns, the time accuracy is 3.5 ns. An insertion delay of 45 ns between the trigger to the first bin is present and any pulse signal arriving 25 ns after the trigger is automatically added to the first bin. The manual time delay added to the MCS for TOF compensation negates this insertion problem by leaving a sufficient time buffer between the first ion counts and the start of the data acquisition.

The discriminator level has a 0.2 mV resolution and an accuracy of 2 mV + 1% with a typical 10 ns pulse pair resolution. Since the discriminator level was manually set to minimize dark counts resulting from thermal noises in the MCP, any lost ions counts will be contained within the errors bars of the ion counts $\sqrt{N}$

6.7.2 HV Power Supply

The ISEG power supplies have a 1 V voltage resolution, a stability $\Delta V_{out}/V_{input} = 5 \times 10^{-5}$ and an accuracy of $\pm(0.05\%\, V_{out} + 0.02\%\, V_{out}^{Max} + 1$ digit). For an input voltage $V_{input} = 24$ V and a maximum output voltage $V_{out}^{Max} = 5$ kV, the resulting stability is $\Delta V_{out} < 1.2$ mV and the accuracy is a function of the output voltage V_{out}, as shown in Table 6–2. The voltage measurements are performed instead by the Keithley multimeter to give a more precise retarding mesh voltage reading than possible with the ISEG power supply.

Table 6–2: Accuracy of ISEG NHQ 205M N24 power supply for different output voltages V_{out} using an input voltage $V_{input} = 24$ V.

V_{out} (kV)	Accuracy (V)
1	2.5
2	3.0
3	3.5
4	4.0
5	4.5

6.7.3 HV Divider box

The HV divider box calibration was performed using a Fluke 83V multimeter in conjunction to the Keithley multimeter. The ISEG power supply, HV divider box and multimeters were allowed to reach a stable operating temperature before performing calibration runs. A scan from 0 - 1 kV with 100 V increments was followed by a scan from 1 - 5 kV with 500 V increments. At each step, the voltage readings were allowed to stabilize before recording the values on the power supply and multimeters. The power supply high voltage output V_{out} was measured using the Fluke multimeter between 0 - 900 V. Values between 1 - 5 kV were obtained from the ISEG power supply display output due to the Fluke multimeter inability to measure above 1 kV. The Keithley multimeter measured the HV divider box low voltage output V_{Div}. A linear fit of the power supply output V_{out} as a function of the HV divider box voltage output V_{Div} was done and is shown in Figure 6–8. A linear fit to the data results in:

$$V_{out} = (991.8 \pm 0.1)\, V_{Div} - (1.3 \pm 0.3)\text{V} \tag{6.1}$$

Equation (6.1) is used to correct the voltage measurements sent from the Keithley multimeter to the RFA program. The error ΔV_{Div} introduced by this step is proportional to V_{out} and a few sample values are shown in Table 6–3.

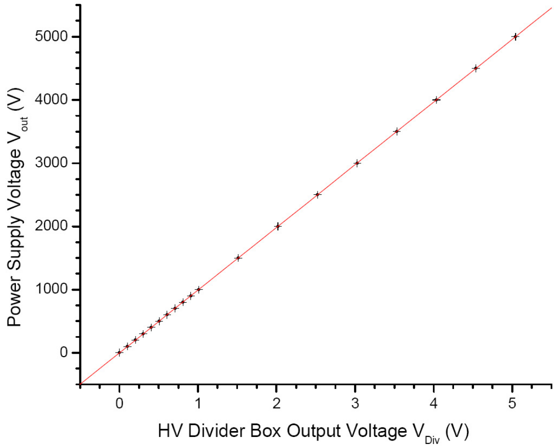

Figure 6–8: Plot for the power supply output V_{out} as a function of the HV divider box voltage output V_{Div}. The solid line is a linear fit to the data.

Table 6–3: Sample data illustrating the HV divider box output voltage V_{Div} accuracy for different power supply output voltages V_{out}.

V_{out} (kV)	ΔV_{Div} (V)
1	0.31
2	0.32
3	0.33
4	0.34
5	0.35

6.7.4 Multimeter

From the HV divider box 1000:1 voltage output, the retarding voltage measured by the Keithley 2700 multimeter will range between 0 - 5 V. Selecting the multimeter 0 - 10 V voltage range, the resulting resolution is 10 μV with an accuracy of $\Delta V_{mm} = 0.35$ mV.

6.7.5 Total Electronic Error

The RFA program acquires the retarding voltage measurements from the Keithley multimeter. In addition to the error introduced by the multimeter itself, the error from the HV divider box must also be considered. The retarding voltage measurement total error ΔV_{tot} will then be the quadratic sum of both. Since $\Delta V_{Div} \gg \Delta V_{mm}$, $\Delta V_{tot} \cong \Delta V_{Div}$ to a very good approximation. Consequently, the rounded up maximum retarding voltage error ΔV_{Div}^{Max} will be 0.4 V for any beam energy below 5 keV. This error will be added with the error obtained from the curve fits performed with Origin and the RFA total energy resolution error to obtain the longitudinal kinetic energy spread error.

CHAPTER 7
Measurements & Analysis

7.1 Experimental Tests with TITAN Ion Source

Two series of experimental runs of the TITAN RFA were performed over two separate sessions. The main objectives were to determine the RFA energy resolution and measure the ion beam longitudinal energy spread under various RFQ settings. The first run consisted mostly of a proof-of-concept and shakedown test for the RFA instrumentation and data acquisition system. After analyzing the first run data and correcting for minor software and hardware technical issues, a second round of testing was conducted. In addition to replicating some previous scans for repeatability purposes, additional RFQ settings were looked at and the resulting longitudinal energy spread were analyzed.

7.2 First Series of Runs (March 14^{th} - March 18^{th}, 2008)

A 50 Hz pulsed 1 keV ^{6}Li^{+} ion beam was sent to the RFA. A series of outer meshes potential optimization scans were first performed, followed by scans at different RFQ buffer gas pressures. The beam energy was subsequently raised to 2, 3 and 4 keV to observe any deviation in the linearity of the RFA energy resolution $\Delta E/E$ by comparing the energy spread ΔE as a function of the beam energy E under the same RFQ parameters.

The double slits were removed during these runs to maximize the incident beam current entering the RFA and reaching the MCP. This resulted in a increase of the RFA energy resolution above the value obtain in Equation (5.4). From the geometric restrictions imposed by the Einzel lens and the frontal RFA opening of radius $r = 17.78$ mm, the new total expected energy resolution error is $\Delta E/E = 5 \times 10^{-3}$.

7.2.1 Optimization of Outer Meshes Potentials

Before proceeding with ion beam longitudinal energy spread measurements, calibration of the RFA outer meshes potentials must be undertaken. From section 6.4, the maximum secondary electron kinetic energy using the TITAN ion source is expected to be 6.4 eV when using a 5 keV $^6\mathrm{Li}^+$ ion beam. The outer meshes applied potentials must be lowered below -6.4 V to ensure that most secondary electrons are properly repelled.

A scan with both outer meshes grounded was first conducted and utilized as a comparison template for later scans under different potential configurations. A minute parasitic current was observed above the expected ion count cutoff retarding voltage V_{max} where $E_{max} = eV_{max}$ is the maximum ion kinetic energy. From section 4.3, the most likely origin of the parasitic current comes from secondary electron emissions from the slits, front and rear meshes reaching the MCP. Further scans with different outer mesh potential configuration are required to validate this hypothesis.

Maintaining the rear mesh grounded, the front mesh was progressively lowered (-7 V, -50 V and -200 V) over three successive scans (Figure 7–1(a)). An inverse relationship between the negative front potential and the parasitic current is observed, cumulating in the independence of ion counts as a function of the retarding potential. This observation can be explained as follows: once the retarding potential V is sufficiently large to stop all incoming ions, these are reflected back towards the front mesh. As in the case during the initial mesh crossing, the mesh effective transparency induces further secondary electron emissions from ion surface impacts. Confined in the potential differential between the front mesh negative and the retarding mesh positive potentials, the electrons quickly accelerate towards the latter with longitudinal kinetic energy e$(V - V_{front})$. Due to the grounded rear mesh and MCP surface, the electrons that pass through the retarding mesh have sufficient kinetic energy to escape the retarding mesh positive potential well and reach the MCP to be counted as ions. As the front mesh negative potential increases, the secondary electron longitudinal kinetic energy will also increase and thus augment the secondary electrons' probability of reaching the MCP in addition to reducing the electron emission transverse dispersal while travelling in the RFA.

The process was repeated with the rear mesh while keeping the front mesh grounded (Figure 7–1(b)). The parasitic current was not visible in any scans with the notable exception of the 0 V / 0 V (front / rear mesh potentials) plot, as described earlier. In this configuration,

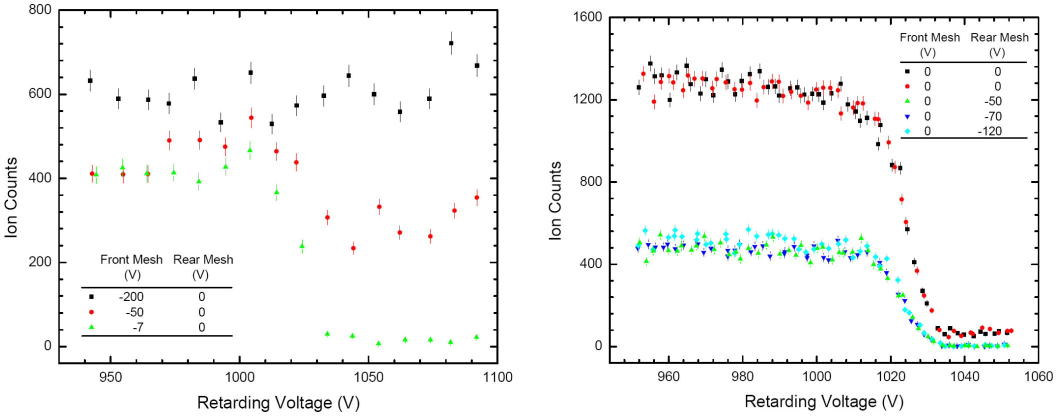

(a) Variable front mesh potential, grounded rear mesh

(b) Grounded front mesh, variable rear mesh potential

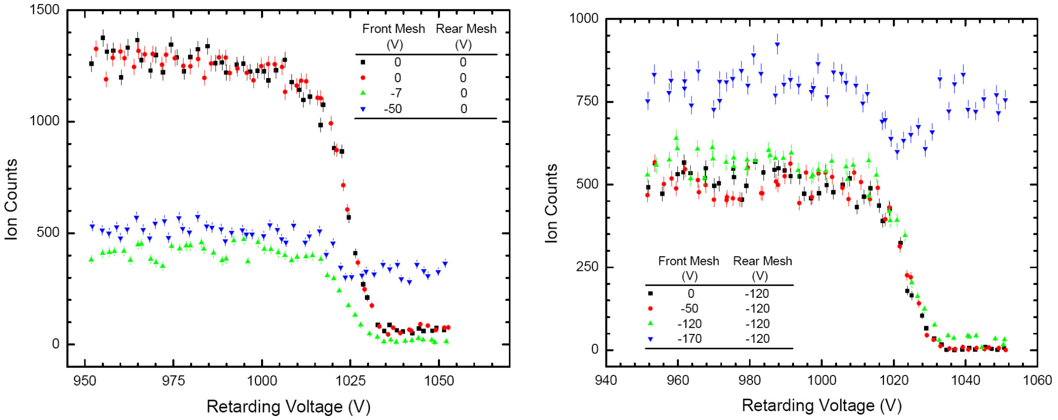

(c) Repeat of (a) with 0V/0V plots.

(d) Variable front mesh potential, rear mesh potential fixed at -120 V

Figure 7–1: Ion counts for a 1 keV $^{6}\text{Li}^{+}$ beam under different outer meshes potentials as a function of the retarding voltage. (a) shows an increase in parasitic current as the front mesh potential is lowered. The 0V/0V plot is missing due to a software glitch which prevented saving the data. (b) Two runs using the 0V/0V configuration were taken with even and odd voltages respectively. The parasitic current is visible in both these runs for $V_{retard} > 1036$ V. The enhanced ion counts in both 0V/0V plots is due to the deactivation of the RFQ beamgate from 1 ms, leaving an unimpeded path for ions entering the RFQ from the TITAN ion source. (c) repeats the scans from (a) with smaller voltages steps. 0V/0V plots are the same as from (b). (d) shows the presence of the parasitic current occurring for front mesh potentials lower that the rear potential.

secondary electrons originating upstream from the retarding mesh cannot reach the MCP due to insufficient kinetic energy to overcome the rear mesh negative potential barrier. Similarly, MCP surface secondary election emissions are suppressed by the same negative potential. Only neutral ionizations and ion-electron neutralizations can thus cause ion count interference in this situation. However from these observations, these last two do not contribute in any detectable amount to the parasitic current under the present experimental conditions, as was theoretically assumed in section 4.3.

Finally, the rear mesh was lowered to -120 V and the front mesh was varied between 0 V, -50 V, -120 V and -170 V (Figure 7–1(d)). For both the 0 V / -120 V and -50 V / -120 V scans, the results were similar to the previous 0 V / -7 V and 0 V / -50 V scans in Figure 7–1(a). The -120 V / -120 V scan was similar to the 0 V / 0 V scan in Figure 7–1(b) and 7–1(c) whereas the -170 V / -120 V scan resulted in a masked ion count as seen earlier by the -50 V / 0 V scan in Figure 7–1(a) and 7–1(c). These observations imply that the outer meshes potential difference contribute to a greater extent than their magnitudes in minimizing the parasitic current, which is easily understood from the required potential difference necessary for the front mesh secondary electrons to reach the MCP. One must also remember that the front mesh potential magnitude invariably affects the lensing effect contribution (Equation (4.10)) to the RFA total energy resolution error. However, as mentioned in section 5.3.3, the effect only becomes problematic for large negative potentials.

From these scans, both meshes must have an applied negative potential, with the rear potential lower, to minimize secondary electron interference with the ion counts, in agreement with previous references [80, 88]. For the remainder of these runs, a conservative -50 V / -120 V configuration was selected.

7.2.2 Longitudinal Energy Spread Dependence on the RFQ Buffer Gas Pressure

During regular operations, the RFQ gas buffer flow is 4 cm^3 per minute (sccm) for an internal pressure of $\sim 4.5 \times 10^{-6}$ Torr. Scans at different gas flows were performed to observe any relationship between the longitudinal energy spread and the buffer gas pressure. The gas flow was varied between 1 and 12 sccm, translating to a buffer gas pressure range between

$\sim 1\times10^{-6} - 1.6\times10^{-5}$ Torr. After analysis, no discernible relationship was observed (Figure 7–2). Without the RFA and HV divider box energy spread error contributions, the average longitudinal energy spread obtained from Origin was 12.0 ± 0.6 eV with all longitudinal energy spread values falling within the error bar. Results including the energy spread error contributions are shown in Table 7–1. These results were expected since the buffer gas pressure variations only effects the ion cooling time to reach thermal equilibrium with the RFQ buffer gas. The TITAN RFQ was designed to have cooling times up to 1 ms, which can successfully cool most of the ion of interest for the TITAN experiment [41]. The cooled ions have a sub 5 eV energy, below the current RFA sensitively, which is then promptly masked by the contributions of the RFQ ion extraction process and various forces along the beamline.

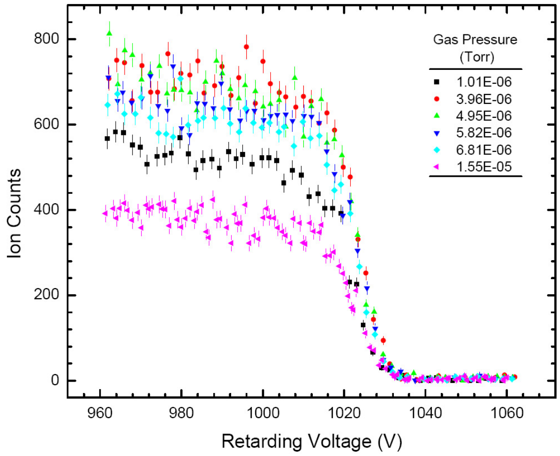

Figure 7–2: Ion counts for a 1 keV $^{6}\mathrm{Li}^{+}$ beam under different RFQ buffer gas pressures as a function of the retarding voltage. Variations in the maximum ion counts for each plot are due to a progressively decreasing beam current exiting the RFA, independently from the buffer gas pressure.

Noted during the scans were a slight steady linear decline in the ion counts along the top plateau where $V_{ion} > V_{mesh}$. When reorganizing the buffer gas pressure scans in the order taken (4, 5, 6, 7, 12 and 1 sccm), the declining trend is noticeable, with the exception of the last scan resulting from a slight increase in the extracted beam current from the TITAN ion source. This was also noticeable at higher beam energy regimes (3 and 4 keV). Postulating that the beam

Table 7–1: Longitudinal energy spreads for a 1 keV $^{6}\mathrm{Li}^{+}$ ion beam as a function of the RFQ buffer gas pressure.

Gas flow (sccm)	Gas pressure ($\times 10^{-6}$ Torr)	Energy spread (eV)
1	1.01	13 ± 5
4	3.96	11 ± 5
5	4.95	12 ± 5
6	5.82	13 ± 5
7	6.81	12 ± 5
12	15.5	13 ± 5

current is decreasing with time and not the result of an ion beam energy distribution with long low energy tail, a long duration (13h) stability scan at 3 keV was undertaken. Figure 7–3 shows that the beam current is indeed decreasing over time approximately at a rate of 2 counts/minute. The source of this problem could not be successfully pinpointed but is believe to originate from the RFQ pulsed drift tube.

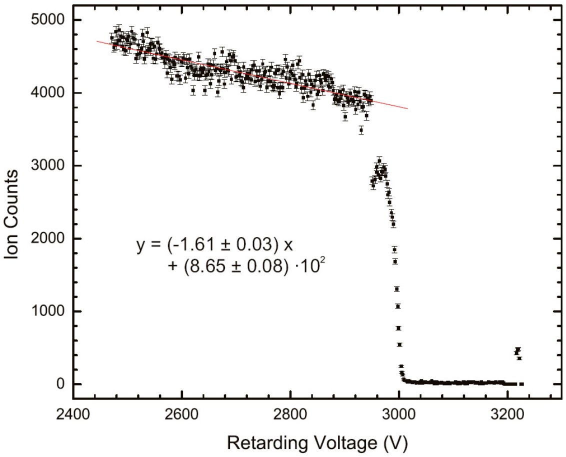

Figure 7–3: Long stability ion count scan of a 3 keV $^{6}\mathrm{Li}^{+}$ beam as a function of the retarding voltage for an approximate rate of one 2 V voltage step per minute. A linear decreasing ion count is clearly visible along the top left plateau. An unidentified error occurred between 2920 V and 2960 V, leading to a sharp drop in count.

The error could stem from two possible sources or a combination of both: unstable pulsed drift tube HV power supply or mistiming of the pulsed drift tube fast switch.

If the pulsed drift tube HV power supply is unstable, the resulting beam energy will also be unstable. Since the electrostatic steerers and Einzel lens potentials along the beam's flightpath are preset for specific fix beam energies, any beam energy deviations from the set value will progressively distort the beam's profile at each element crossing due non-linear transverse forces starting from the beamline geometric center. Eventually, the elements cannot maintain a cohesive beam and some ions are lost, colliding against the beamline internal structures. The magnitude of the loss is approximately proportional to the difference between the actual and preset beam energies.

If the pulsed drift tube fast switch is not properly synchronized to lower the HV when the ion pulse is axially centred within it, the ion pulse would experience a longitudinal potential gradient with the result that the ion final longitudinal kinetic energy is axially dependent with respect to the pulse drift tube axial center. The net effect is an ion pulse longitudinal kinetic energy profile broadening with a deviation of the beam average longitudinal kinetic energy. Depending on the ion longitudinal kinetic energy difference from the preset beam energy, some ions would be lost due to the effects postulated in the first error above, leading to a diminished beam current reaching the RFA. This effect is highly time and energy sensitive due to the ion pulse velocity, pulse drift tube length and HV potential gradient.

7.2.3 Linearity of Longitudinal Energy Spreads under Different Beam Energies

A list of longitudinal energy spreads at different beam energies while preserving the RFQ frequency and gas pressure settings (Table 7–2) and trapping/extraction potentials (Table 7–4) is shown in Table 7–3. Due to the small sampling data for each energy level, a linear relationship of the energy spread as a function of the beam energy is not discernible. The small difference between the energy spreads obtain for 1 and 2 keV shows that the RFA energy resolution error masks the actual energy spread value at 1 keV. At higher energies, the ion beam erratic and steady declining count rate created difficulties in ascertaining the ion beam energy spread, varying broadly between 73 to 88 eV with an uncertainty of 20 eV at 4 keV. From Figure 7–4, the best linear fit for the RFA energy resolution linearity gives $\Delta E/E = (1.4 \pm 0.5) \times 10^{-2}$, which is significantly larger than the initial goal of 10^{-3}.

Table 7–2: RFQ frequency and gas settings employed for longitudinal energy spread measurements as a function of the $^{6}\mathrm{Li}^{+}$ beam energies.

Frequency (Hz)	Gas flow (sccm)	Gas pressure (Torr)
50	4	3.58×10^{-6}

Table 7–3: Longitudinal energy spreads for $^{6}\mathrm{Li}^{+}$ under different beam energies using the RFQ parameters shown in Table 7–2.

Beam energy (keV)	Energy spread (eV)
1	11 ± 5
2	15 ± 10
2	16 ± 10
3	19 ± 15
4	85 ± 20
4	88 ± 20
4	73 ± 20
4	78 ± 20

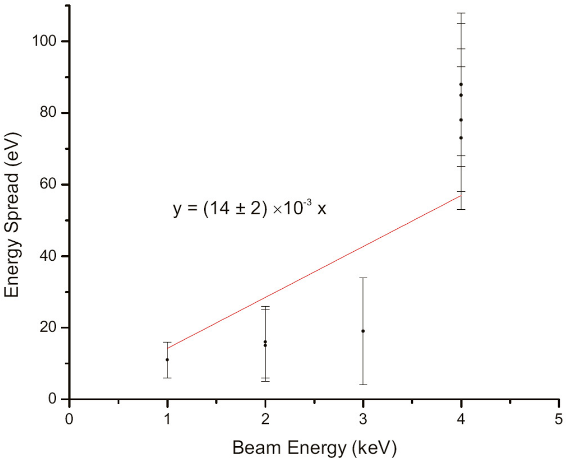

Figure 7–4: Plot for the longitudinal energy spread $\Delta E_{\|}$ as a function of the $^{6}\mathrm{Li}^{+}$ beam energy. The solid red line is the best linear fit to the data, forced through the origin.

7.2.4 Conclusion from First Run

As previously seen in other three mesh RFAs [80, 88], the outer meshes must be negatively biased, with the rear mesh having a slightly lower potential to minimize parasitic current on the

MCP. The primary source of the current is from the front mesh secondary electron emissions, resulting from reflected ion surface impacts, reaching the MCP. Neutral ionizations and ion-electron recombinations contributions are negligible due to the low secondary electron and neutral densities. The contribution of secondary electron emission from neutral-MCP surface impacts remains to be investigated. From these observations, the outer mesh potentials were conservatively selected, with -50 V front and -120 V rear.

The double slit removal resulted in a RFA energy resolution error ($\Delta E/E = 5 \times 10^{-3}$) five times larger than the original designated goal ($\Delta E/E < 10^{-3}$). This effect is visible in both the longitudinal energy spread non-linear relationship at different beam energies (Figure 7–4) and the independence of the longitudinal energy spread as a function for the RFQ buffer gas pressure (Table 7–1). The latter was expected due to the small final ion energy ($<$ 5 eV) resulting from the RFQ buffer gas cooling and the narrow pressure range observed which does not sufficiently alter the cooling time enough to be detectable with the current RFA energy resolution error. As for the former, the beam instability may have also contributed in the large longitudinal energy spread variations observed in addition to the energy resolution error. The reincorporation of the double slit is necessary to resolve the longitudinal energy spread at low beam energies while reducing the RFA total energy resolution error.

The beam stability problem, first observed during the RFQ gas buffer scans, has to be remedied. The large energy spread values obtained at high beam energies could be partly explained by this phenomena (see Table 7–3). The pulsed drift tube HV power supply was subsequently replaced for the next series of runs, in the hope this is the source of the beam instability.

7.3 Second Series of Runs (July 3rd - July 7th, 2008)

In addition of repeating the scans previously done for comparison purposes, a broader set of parameters were looked at; the RFQ extraction potentials and beamgate size, ion beam composition and space charge limit. The RFA double slits were reinstalled, decreasing the total energy resolution error to $\Delta E/E = 2.4 \times 10^{-3}$.

During preparation for the runs, the Belhke fast switch experienced a terminal failure, preventing the usage of the pulsed drift tube. While a temporary 20 kV replacement switch was being prepared, the RFQ HV was lowered to 4.5 kV with the pulsed drift tube matching, thus creating an extracted ion beam of 4.5 keV. This configuration was selected due to the necessity of having a sufficiently high ion extraction potential on the TITAN ion source to inject a steady ion current into the RFQ.

Near the halfway point of the runs, the temporary 20 kV fast switch was installed and the RFQ was floated back to an equivalent voltage. Shortly after, the beam stability problem previously encountered during the first runs became significantly more prominent at low beam energy, to the point where the longitudinal energy spread measurements obtained from the retarding voltage plots became compromised. For security, the pulsed drift tube voltage drop was limited to 16 kV, thus creating a 4 keV beam. Stability scans, by grounding the retarding voltage, were taken when signs of instability appeared. Once the beam was deemed stable, normal scanning operation resumed. From this observation, it can be concluded that the pulsed drift tube timing is de-synchronized with the incoming ion pulses but was only determined after the testing session was completed.

7.3.1 Optimization of Outer Mesh Potentials

A 50 Hz pulsed 3 keV ^{6}Li$^+$ beam was sent to the RFA. Different outer mesh potential configurations were again looked at and variations in the ion counts as a function of the retarding potential were noted. The results are shown in Figure 7–5. The plots reveals results consistent with data observed in section 7.2.1.

A linear proportionality between the ion counts along the top plateau for non-parasitic current plots (-5 V / -10 V, -10 V / -20 V, -50 V / -100 V and -100 V / -400 V) and the outer mesh negative potentials can be observed. However, due to the ongoing problem with the pulsed drift tube affecting the beam current stability, no definite conclusion would be taken from it.

In both the 0 V / 0 V and -10 V / -5 V configuration plots, a parasitic current above the cutoff retarding voltage V_{max} is present, as previously seen in Figures 7–1(a), 7–1(b) and 7–1(c). Furthermore, an overall ion count enhancement in the -10 V / -5 V configuration, independently of the retarding voltage, was also noted. When comparing to the reciprocal -5 V / -10 V configuration, no ion count enhancement nor parasitic current is noted in the latter, although both have similar neutral ionization and ion-electron recombination rates. As previously concluded, front mesh secondary electrons are, by large, the main contributor in the parasitic current observed on the MCP with both the ionization and recombination playing insignificant roles. The ion count enhancement can be accounted by front mesh secondary electron emissions resulting from rearward directed ion grazing impacts along the inner wire surfaces facing the mesh openings. The ion longitudinal kinetic energy impedes a rearward velocity component to the secondary electrons, sufficient to overcome the small longitudinal potential gradient between the point of emission and the wires center. Once in the retarding mesh positive potential well, they have sufficient kinetic energy to then proceed to the MCP. Furthermore, the similar parasitic current between the -10 V / -5 V and -7 V / 0V plots indicate that neutral MCP surface impact secondary electron emission is either not a major factor in the MCP parasitic current or that the emitted electron energy distribution is larger than 5 eV.

The effects from secondary electron emission induced by neutral MCP surface impacts can be analyzed from the +10 V / +20 V configuration plot. Due to the outer mesh positive potentials, the retarding mesh potential well extends to the grounded RFA body and MCP surface while encompassing both outer meshes. In this configuration, all secondary electron emissions from the meshes do not possess sufficient longitudinal kinetic energy to escape the well and reach the MCP. Furthermore, any neutral induced secondary electron emissions from the MCP surface will be attracted to the retarding mesh by the extended potential well. When comparing the average ion count rates when $V_{ret} > V_{beam}$ for the - 5 V / -10 V scan (105 ± 6) and the following +10 V / +20 V scan (117 ± 9) taken on the same day, no difference in the residual counts outside of their error bars is seen. Other scans in Figure 7–5 were taken on a separate day and did not yield any anomalous discrepancies in the residual counts either. As in the case for both neutral ionizations and ion-electron recombinations, neutral induced secondary electron emission from the MCP surface do not contribute in a noticeable way to the ion count enhancement nor the parasitic current seen in the plots.

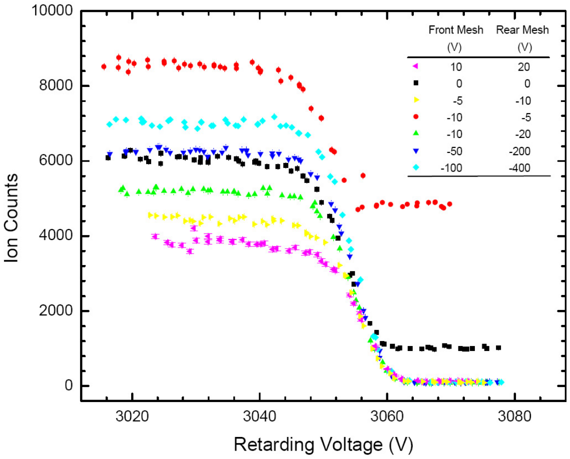

Figure 7–5: Ion counts for a 3 keV $^{6}Li^{+}$ beam under different outer mesh potentials as a function of the retarding voltage. Both the 10 V / 20 V plot (purple) and the -5 V / -10 V plot (yellow) were displaced by +25 V to match the beam energy of the other plots since these two runs where performed on a separate day.

As ascertained in section 6.4, small negative potentials on the outer meshes, with the rear mesh having a lower potential that the front, is required to effectively negate secondary electron emissions from interfering with the MCP ion counting process. This is noticeable from the similar plots for the -50 V / -120 V (Figure 7–1(d)) and -10 V / -20 V configurations (Figure 7–5). From the observations described above, the -10 V / -20 V configuration was selected and employed for the remainder of the runs.

7.3.2 Longitudinal Energy Spread Dependence on the RFQ Extraction Electrodes Potentials

During normal RFQ operations, the ions are axially trapped using a series of 24 electrodes, as shown in Figure 2–5. A timing trigger switches the potential of electrodes #22 and #24 by increasing the former and decreasing the latter below the applied potential of electrode #23, promptly ejecting the ions out of the trap. Depending on the extraction potential magnitude, the resulting extracted ion pulse longitudinal energy spread profile is altered. For instance, extraction computational simulation with the electrode #22 grounded and -30 V potential on electrode #24 (0 V / -30 V) resulted in $\Delta E_{\|} \cong 2.4$ eV whereas a 500 V / -500 V configuration results in a $\Delta E_{\|} \cong 24.0$ eV using a 2.5 keV ion beam [41].

Two series of runs using a 2.5 keV beam of $^{23}\mathrm{Na}^{+}$ and $^{7}\mathrm{Li}^{+}$ respectively were employed to study this effect and simultaneously observe any mass dependence.

In both species, a linear proportionality between the longitudinal energy spread and the extraction potentials magnitude is present, as shown in Figure 7–6(a) and 7–6(b). Since the extraction potentials employed in both species were different (Table 7–5(a) and 7–5(b)), longitudinal energy spread species independence cannot be confirmed. Of worthy mention is the energy spread decrease for $^{23}\mathrm{Na}^{+}$ between the two largest extraction potential difference runs. The low ion counts for the 76.7 V / -74.5 V plot (Figure 7–6(b)) results in Origin underestimates the true energy spread due to the large counting error $\sqrt{N}$ with respect to the ion counts at this level. The diminished ion count result is due to having performed the scan on a separate day then the other three plots, when the beam current density was weaker.

Table 7–4: Default RFQ trapping and extraction potential settings employed in the TITAN experiment.

Trapping Potential (V)			Extraction Potential (V)	
ΔV_{22}	ΔV_{23}	ΔV_{24}	ΔV_{22}	ΔV_{24}
-6.47	-6.91	5.03	12.9	-26.1

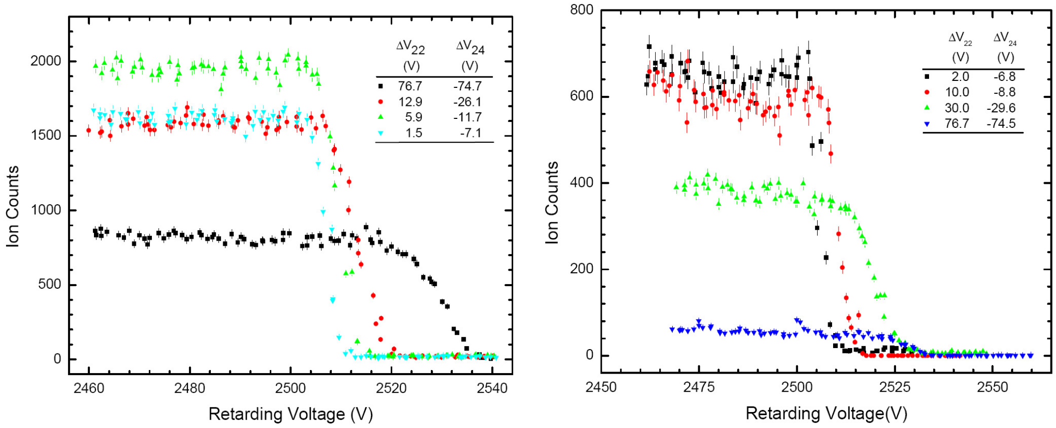

(a) $^{7}\mathrm{Li}^{+}$

(b) $^{23}\mathrm{Na}^{+}$

Figure 7–6: Ion count plots of a 2.5 keV (a) $^{7}\mathrm{Li}^{+}$ and (b) $^{23}\mathrm{Na}^{+}$ beams with different RFQ extraction potentials as a function of the retarding voltage.

Table 7–5: Longitudinal energy spreads for a 2.5 keV ion beam of (a) $^{7}\mathrm{Li}^{+}$ and (b) $^{23}\mathrm{Na}^{+}$ as a function of the RFQ extraction potentials.

(a) $^{7}\mathrm{Li}^{+}$

Extraction Potential (V)		Energy Spread (eV)	Beam Energy (eV)
ΔV_{22}	ΔV_{24}	$\Delta E_{parallel}$	V_0
76.7	-74.7	11 ± 6	2530 ± 6
12.9	-26.1	8 ± 6	2513 ± 6
5.9	-11.7	6 ± 6	2510 ± 6
1.5	-7.1	4 ± 6	2507 ± 6

(b) $^{23}\mathrm{Na}^{+}$

Extraction Potential (V)		Energy Spread (eV)	Beam energy (eV)
ΔV_{22}	ΔV_{24}	$\Delta E_{parallel}$	V_0
76.7	-74.5	10 ± 6	2527 ± 6
30.0	-29.6	12 ± 6	2519 ± 6
10.5	-8.8	6 ± 6	2510 ± 6
2.0	-6.8	5 ± 6	2505 ± 6

A secondary effect is the linear correlation between the average beam energy eV_0 and the extraction potential magnitude (Table 7–5(a) and 7–5(b)). This is due to the extraction process where the ions are simultaneously attracted by the electrode #24 negative potential while being repelled out by the electrode #22 positive potential, imparting some additional kinetic energy to the extracted ions and increasing the ion pulse average longitudinal energy.

Comparing the experimental results in Table 7–5 to the RFQ extraction computation simulations [41], the experimental values are approximately doubled. This difference can be attributed to the locations where both measurements were taken. Whereas the simulated longitudinal energy spread was immediately obtained after the extraction electrodes, the ion beam must travel several metres separating the RFA and the RFQ extraction electrodes before the energy spread can be measured. During this time, two successive 45° benders between the vertical aligned RFQ to the horizontal TITAN beamline (see Figure 2–2) and various steering elements mixes the transverse and longitudinal components due to their non-linear forces on the beam, in addition to longitudinal reheating from the Boersch effect [100] after post acceleration from the pulsed drift tube. A longitudinal energy spread enlargement can thus be expected.

7.3.3 Energy Resolution for Different Ion Beam Compositions

Three isotopically pure (^{6}Li^{+}, ^{7}Li^{+} and ^{23}Na^{+}) and two mixed (^{6,7}Li^{+} and ^{39,41}K^{+}) ion beams from the TITAN ion source were looked at. Refinement of the ^{39,41}K^{+} ion beam into two isotopically separated beams was not attempted due to the low count rate observed. Problems encountered with the pulse drift tube switch, beam stability and time availability prevented us from observing each ion beam at the same beam energy value. In an attempt to alleviate this problem, the beam energy resolution was compared under the same experimental conditions as described in section 7.2.3 using the theoretical linear relationship between the energy spread and beam energy. Since none of the ^{23}Na^{+} scans used the RFQ extraction potentials described in Table 7–4, ^{23}Na^{+} could not be compared with the four other beams.

The resulting energy resolution values obtained are shown in Table 7–6. No correlation between the ion species and the energy resolution is measurable under the current RFA energy resolution error. Preliminary results tend to indicate that the ion beam composition is an irrelevant factor in the longitudinal energy spread, as shown from the mass independence in the RFA longitudinal kinetic energy filtering process (section 4.5). Further refinements of the RFA energy resolution error are required before these assumptions can be confirmed.

Table 7–6: Energy resolution of different ion beam composition under same RFQ extraction potentials.

Ion beam composition	Energy resolution $\Delta E/E$ (10^{-3})
^{6}Li^{+}	2.8 ± 2.2
^{6,7}Li^{+}	3.4 ± 2.2
^{7}Li^{+}	3.3 ± 2.2
^{39,41}K^{+}	3.1 ± 2.2

7.3.4 Longitudinal Energy Spread Dependence on the Space Charge Limit

The space charge limit effect on the ion beam longitudinal energy spread was quickly looked into. Using a 4.5 keV ^{6,7}Li^{+} ion beam, the current density was progressively increased for three scans by reducing the amount of beam deflection between the TITAN ion source and the RFQ. The resulting current density increase is visible by the ion count increase along the top plateau

(Figure 7–7). A minute linear relationship between the longitudinal energy spread and the beam current density was observed (see Table 7–7) but cannot be confirmed due to the large 10 eV energy resolution error at this beam energy.

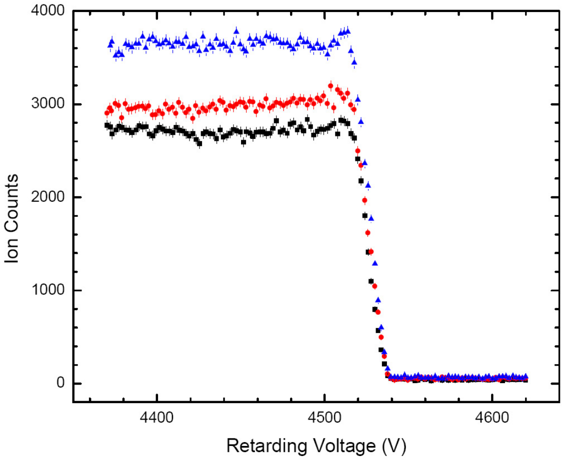

Figure 7–7: Ion count plot of a 4.5 keV ^{6,7}Li^{+} beam with different injection beam currents as a function of the retarding voltage. Higher beam current results in increased ion count but negligible variation in the longitudinal energy spread.

Table 7–7: Longitudinal energy spreads as a function of the injected beam current from the TITAN ion source.

Energy Spread (eV)
13.5 ± 10
13.7 ± 10
14.0 ± 10

7.3.5 Longitudinal Energy Spread Dependence on the Beamgate Size and Extraction Trigger Delay

A 1 keV ^{6}Li^{+} beam was employed to observed the effects of the RFQ beamgate size and extraction trigger delay on the extracted ion longitudinal energy spread. A fast millisecond switch was used to ground the RFQ deflection electrode, situated upstream from the RFQ segmented axial trapping electrodes, for short time lengths at periodic intervals, permitting an uninterrupted ion beam to enter the RFQ. Time windows lengths of 64, 512 and 1024 μs were investigated, in addition to the RFQ extraction trigger delay of 1 and 10 ms for each value. A proportionality correlation between the time window lengths, extraction trigger delay and the number of trapped ions is expected to lead to an increase of the extracted ion pulse longitudinal energy spread. The RFQ extraction potentials ΔV_{22} and ΔV_{24} (Table 7–4) were lowered to 1.5 V and -7.8 V respectively to reduce their contribution on the extracted ion pulse longitudinal energy spread as seen in section 7.3.2.

Figure 7–8 shows a linear correlation between the beamgate size and the ion counts, independently of the extraction trigger delay. Similar, the 10 ms trigger delay results in a smaller ion count compared to 1 ms for a fixed beamgate size. However, the longitudinal energy spreads do not show any correlation with the beamgate size nor the trigger delay outside from the RFA energy resolution error (Table 7–8). The smaller values can mostly be attributed to the reduced RFQ extraction potentials. The RFQ cooling time and final thermal equilibrium energy (sub 5 eV) for most ions results in longitudinal energy spread smaller than the current RFA energy resolution sensitivity. A smaller energy resolution is required in order to resolve any variations due to the effects of beamgate sizes and extraction trigger delay times.

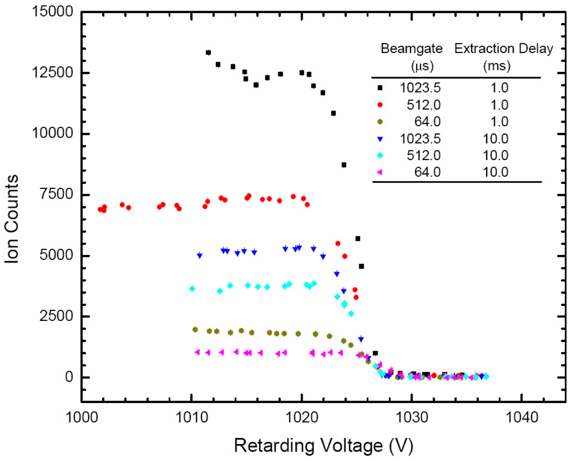

Figure 7–8: Ion count plot of a 1 keV ^{6}Li^{+} beam for different RFQ beamgate times and extraction trigger delays as a function of the retarding voltage. Both 64.0 ms beamgate plots (dark yellow and purple) were displaced laterally by $\sim$ -11 V to match the beam energy of the previous day.

Table 7–8: Longitudinal energy spreads for a 1 keV ^{6}Li$^+$ beam as a function of RFQ beamgate size and extraction trigger delay time.

Beamgate (μs)	Trigger (ms)	Energy Spread (eV)
1023.5	1.0	3 ± 3
512.0	1.0	3 ± 3
64.0	1.0	3 ± 3
1023.5	10.0	3 ± 3
512.0	10.0	3 ± 3
64.0	10.0	3 ± 3

7.3.6 Longitudinal Energy Spread Dependence on the RFQ Buffer Gas Pressure

Following section 7.2.2, the RFQ buffer gas pressure measurements using a 1 keV ^{6}Li$^+$ ion beams was repeated and a second 4.5 keV ^{7}Li$^+$ ion beam was also conducted. The RFQ gas flow range was reduced to between 1 and 8 sccm due to fears of possible electrical discharge between the axial trapping electrodes. Again, the RFQ extraction potentials ΔV_{22} and ΔV_{24} lowered to 1.5 V and -7.8 V respectively to improve the probability of observing variations in the ion pulse longitudinal energy spread. Plots of ^{6}Li$^+$ and ^{7}Li$^+$ under different gas pressures as function of the retarding voltage are shown in Figures 7–9(a) and 7–9(b) with the longitudinal energy spread values shown in Tables 7–9(a) and 7–9(b) respectively.

Table 7–9: Longitudinal energy spreads of (a) 1 keV ^{6}Li$^+$ beam and (b) 4.5 keV ^{7}Li$^+$ as a function of the RFQ buffer gas pressure.

(a) ^{6}Li$^+$

Gas flow (sccm)	Gas Pressure ($\times 10^{-6}$ Torr)	Energy Spread (eV)
1.02	0.67	3 ± 3
2.02	1.60	3 ± 3
4.02	3.58	3 ± 3
5.00	4.66	3 ± 3
6.02	5.65	3 ± 3
7.02	6.62	3 ± 3
8.00	7.80	3 ± 3

(b) ^{7}Li$^+$

Gas flow (sccm)	Gas Pressure ($\times 10^{-6}$ Torr)	Energy Spread (eV)
0.93	0.50	5 ± 10
1.02	0.61	5 ± 10
2.02	1.52	4 ± 10
4.02	3.58	4 ± 10
8.02	7.43	4 ± 10

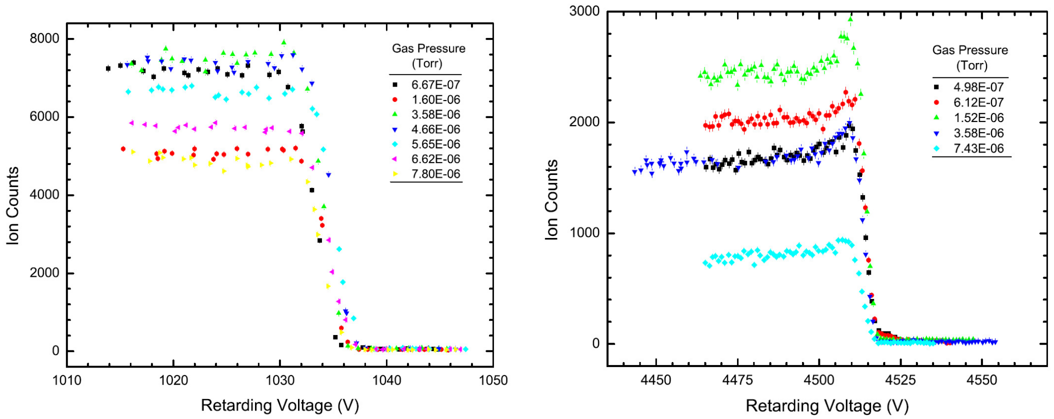

(a) 1 keV ^{6}Li$^+$ beam

(b) 4.5 keV ^{7}Li$^+$ beam

Figure 7–9: Ion counts plots for 1 keV ^{6}Li$^+$ (left) and 4.5 keV ^{7}Li$^+$ (right) ion beam under different RFQ buffer gas pressure as a function of the retarding voltage.

As in section 7.2.2, no correlation is visible between the gas pressure and the longitudinal energy spreads in either beam. It can be concluded that if any longitudinal energy spread variations as a function of the buffer gas pressure is present, they are smaller than the RFA energy resolution sensitivity and cannot be distinguished from the larger RFQ extraction longitudinal energy spread. As seen the previous section, the reduced ion pulse longitudinal energy spread values are mostly attributed to the smaller RFQ extraction potentials. This observation implies that the extraction potential contributes significantly more in the final outcome of the energy spread than the RFQ buffer gas pressure does. Further refinement of the RFA energy resolution is necessary if one hopes to observe some energy spread variations induced by the RFQ buffer gas pressure.

An unforeseen effect from any previous scans was a linear increase and spiking of the ion counts as the retarding voltage neared the average 4.5 keV ^{7}Li$^+$ beam in Figure 7–9(b). This occurrence was also noted for every 4.5 keV ^{7}Li$^+$ scan, regardless of the RFQ buffer gas pressure selected. The ion count spike is caused by the beam focusing around the retarding mesh wires as $V_0 \lessapprox V_{mesh}$ (section 4.2.1). From the calculated focusing effect energy resolution error in Equation (5.2) for the mesh employed, the theoretical error for a 4.5 keV beam is ~ 0.7 eV, smaller than the experimental half width of the peak observed ($\sim$ 4 eV). However, the measured plots match remarkably well to the simulated mesh plots (Figure 5–5) except for a diminished ion count peak over the ion count baseline and larger peak half width than from the simulation ($\sim$ 1 eV). Other unaccounted effects such as beam divergence, energy spread, non-parallel meshes and diminished beam current in the simulations could explain these divergences.

The explanation for the observation of this effect over previous scans arises from having a stable beam current during these runs. For most runs undertaken during the two sessions, the beam current had a small decay, which would smooth out any ion count spiking in the ion count plot. Furthermore, the expected small width combined with its linear dependence to the beam energy makes it difficult to detect over the statistical ion count error $\sqrt{N}$ and the 1 V retarding potential steps.

7.3.7 Conclusion from Second Run

The addition of RFA slits permitted the RFA energy resolution to be reduced by half ($\Delta E/E = 2.4 \times 10^{-3}$) compared to the previous series of runs ($\Delta E/E = 5 \times 10^{-3}$). The negative potential of the outer meshes were reduced to a front/rear configuration of -10 V / -20 V from the previous setting of -50 V / -200 V while still minimizing ion count interference from secondary electrons. From the scans, it was found that the source of the parasitic current comes mainly from secondary electron emissions originating from the slits and front mesh reaching the MCP. Secondary electron emissions from ion MCP surface impacts, neutral-electron ionizations and ion-electron recombinations are themselves insignificant contributors in the parasitic current within the scope of this experiment.

A linear correlation between the RFQ extraction electrode potentials, the longitudinal energy spread and average beam energy is noticeable for both 2.5 keV ^{23}Na^{+} and ^{7}Li^{+} beams. Independence of the ion composition cannot be fully ascertained due to the use of different extraction potentials for either beams. The energy resolution of four different ion beam composition (^{6}Li^{+}, ^{6,7}Li^{+}, ^{7}Li^{+} and ^{39,41}K^{+}) with varying beam energies did not reveal any correlation within the RFA energy resolution error. This is expected due to the mass independence of the RFA high-pass filtering process.

No correlation between the RFQ buffer gas pressure and longitudinal energy spread was again noticed when using a 1 keV $^{6}Li^{+}$ beam, even with improved RFA energy resolution. The large cooling time, ion low final thermal equilibrium energy and large energy spread during the RFQ extraction process mask any variations below the RFA energy sensitivity. These effects also resulted in no correlation between the RFQ beamgate size and the longitudinal energy spread. In both instances, the RFQ extraction potentials were lowered to reduced their contribution to the total ion pulse longitudinal energy spread and increase the probability of observing variations in the energy spread. From these observations, it can be concluded that the RFQ extraction potentials affect the longitudinal energy spread to a larger extent than the RFQ buffer gas pressure, beamgate size or extraction delay under any of the preset settings used in the TITAN experiment.

Further energy resolution error reduction to the 10^{-4} level would be beneficial in resolving any energy spread variations induced by the parameters cited above. An entirely new double slit system would thus need to be installed within the beamline or a significant RFA assembly modification in order to achieve this new requirement. Such changes will be further discussed in section 8.2.

CHAPTER 8
Summary & Outlook

8.1 Summary

The goal of this thesis was to design, construct and test a Retarding Field energy Analyzer (RFA) to measure the pulsed ion beam longitudinal energy spread used in the TITAN experiment. This information can subsequently be employed to establish its contribution to the error analysis for high-precision mass measurements with the Penning trap and to fine-tune the ion pulse extraction process of the ion traps in the TITAN experiment to minimize the energy spread. After initially proceeding through an elimination process to ascertain the best suitable method to perform this task under the physical constraints imposed by the TITAN experiment, a retarding field energy analyzer (RFA) was selected. The RFA small footprint allows for easy and simple installation in any available access port of a 4-way 8 inch cross along any of the TITAN beamlines. When offline, the RFA can be retracted from the ion beam into the access port using a linear manipulator, thus permitting the ion beam to pass the RFA. From these fundamental constraints and a minimum energy resolution $\Delta E/E < 0.001$, the RFA design was undertaken using specialized software for the physical design (SolidWorks) and numerically simulations (SIMION) to satisfy all the physical requirements and goals placed.

After insuring that all RFA components satisfied design specifications, the RFA was installed into the main TITAN beamline, adjacent but upstream from the Penning trap. Using the TITAN ion source, in conjunction with the RFQ, five different ion beam compositions (^{6}Li^{+}, ^{7}Li^{+}, ^{6,7}Li^{+}, ^{23}Na^{+} and ^{39,41}K^{+}) with variable energy outputs (1-5 keV) were made available for testing. The experimental testing was conducted over two distinct week-long sessions. The first session was primarily devoted as a shakedown test for the RFA's electronic and data acquisition systems using a ^{6}Li^{+} beam at various energies. To maximize the incoming beam detection probability, the RFA slits were removed, resulting in the RFA's energy resolution error increase to $\Delta E/E = 5 \times 10^{-3}$ (section 7.2).

The outer mesh potential optimization was first conducted and a very conservative front/rear configuration of -50 V / -120 V was selected to minimize any parasitic current resulting from secondary electron emissions due to ion or neutral impacts with the meshes or MCP surface. Preliminary results indicate that the parasitic current is mostly the result of secondary electron emitted from the slits and first mesh reaching the MCP, with ion-electron recombination and neutral-electron ionization contributing in no detectable fashion. The contribution of secondary electron emissions from the MCP surface was not investigated.

Longitudinal energy spread measurements at 1 keV did not display any correlation with the RFQ buffer gas pressure between 1.01×10^{-6} and 1.55×10^{-5} Torr, with an average value of 12 ± 5 eV. This is expected due to the RFQ cooling time and low thermal equilibrium energy (below 5 eV).

The relation between the energy spread ΔE and the beam energy E, while keeping the RFQ settings constant, was not linear and had an average energy resolution of $\Delta E/E = (1.4 \pm 0.5) \times 10^{-2}$. This large deviation from the expected theoretical RFA energy resolution $\Delta E/E = 5 \times 10^{-3}$ was believed to be the result of an unstable RFQ HV drift tube, which yielded exceptionally large energy spread (~ 80 eV) at 4 keV. As a precaution, the RFQ HV drift tube power supply was subsequently replaced before the start of the second run of experimental testing with the RFA.

After analyzing the first session data, some minor corrections to the software system and RFA design were carried out. The slits were reinstalled, lowering the energy resolution to $\Delta E/E = 2.4 \times 10^{-3}$.

Re-optimization of the outer mesh potentials was first performed, permitting a decrease in the front/rear potential configuration to -10 V / -20 V while still minimizing the parasitic current. The scans yielded similar results as first observed during the first session. Contribution from secondary electron emission from ion MCP surface impacts to the parasitic current were found to be negligible.

Using two separate 2.5 keV beams of $^{7}\mathrm{Li}^{+}$ and $^{23}\mathrm{Na}^{+}$, the RFQ extraction electrode potentials were varied and the resulting energy spreads were measured. On both occasions, the energy spread and average beam energy are proportional to the extraction potential magnitude and there is no definitive evidence pointing to a species dependence.

Longitudinal energy spread variations as a function of the RFQ buffer gas pressure was repeated using two beams of 1 keV $^{6}\mathrm{Li}^{+}$ and 4.5 keV $^{7}\mathrm{Li}^{+}$ respectively. In both cases, no perceptible correlation was observed, as expected from the RFQ long cooling time and low thermal equilibrium energy (< 5 eV), implying that such changes are smaller than the RFA energy sensitivity. The RFQ's beamgate size and extraction trigger delay were looked at using a 1 keV $^{6}\mathrm{Li}^{+}$ beam. A proportionality between the beamgate size and ion count is easily noticeable, as with the trigger delay. Again due to the RFA energy resolution, no correlation between the energy spread and beamgate size is noticeable, dismissing any pertinent conclusion.

Since the RFQ extraction potentials were lowered during the RFQ buffer gas pressure, beamgate size and extraction trigger delay scans, the resulting energy spread values were smaller than any previously seen during the experiment. Combined with the linear relationship observed between the extraction potentials and energy spreads, it can be concluded that the RFQ extraction potentials contribute more to the final energy spread that the RFQ buffer gas pressure, beamgate size or the extraction delay trigger within the settings employed in the TITAN experiment.

8.2 Outlook

In principle, the RFA energy resolution can be decreased below the 10^{-3} level through the installation of a new slit assembly to further diminish the maximum beam divergence angle θ (Equation 4.7). However, since reducing the slits diameter any further will significantly truncate the beam current entering the RFA, expanding the slits separation becomes the only valid option. This may be prove to be difficult due to the limited spacing inside an 8 inch diameter access port in a 4-way cross. By replacing the current bracket holding the RFA by a modified version which displaces the RFA approximately 25 mm rearward, sufficient space is created in front of the RFA to install a modified front plate with a slit separation $d \sim 60$ mm. For this new configuration, the RFA energy resolution would decrease by two-thirds to 7×10^{-4}. Additional separation can be gained by extending the inner slit closer to the first mesh without compromising the energy resolution caused by the lensing effect. For instance, by moving the inner slit 5 mm closer to the first outer mesh, the slit separation is increased to 65 mm and the total energy resolution error is reduced to 6×10^{-4}. The resulting lensing energy resolution error (Equation 4.10) at the inner slit using a singly charged 1 keV beam and an -10 V applied potential on the mesh is then 1×10^{-7}, still negligible in the RFA total energy resolution error.

The inclusion of a fourth mesh within the RFA can be beneficial in reducing the mesh errors (section 4.2.1) components in the total energy resolution (section 5.3.3). Similar to the 3-mesh configuration, the 4-mesh design differs by the usage of the two central meshes as the high-pass kinetic energy filter as opposed to one. This arrangement creates an equipotential space between the two meshes that diminishes the field penetration caused by the outer mesh potentials and matches closely to the central meshes' potential [88]. Since previous theoretical RFA energy resolution analysis involved a 3-mesh configuration [63, 64], computational simulation of the 4-mesh design and experimental testing using a monoenergetic beam is necessary to determine the energy resolution error of this design. However, the total transparency would be further reduced and would necessitate higher beam currents to compensate for the difference. For low intensity beams, the resulting low ion counts would introduce a larger energy spread error when using the curve fit from Origin, as previously witnessed by the 2.5 keV $^{23}\mathrm{Na}^{+}$ beam in section 7.3.2.

Currently, it is envisioned that the RFA assembly will be incorporated to the EBIT beamline and be used to measure the EBIT extracted ion pulse longitudinal energy spread profile. Up to now, there is no known in-depth detailed analysis of the relationship between the extracted ion longitudinal energy spread and the EBIT trapping and extraction processes. Two previous studies performed a brief look at the energy spread using an HCI beam directed onto a target. A reverse field bias method is applied on the target and the resulting current on the target as a function of the applied positive bias was obtained. In the first case, a 7 kV extracted neon-like Xe^{44+} beam resulted in an 15 eV spread [101] whereas the second case obtained an 22 qV energy spread for a 5.35 kV extracted H-like Ar^{17+} beam [102] where q is the ion charged state.

The principal origin of the energy spread inside an EBIT arises from the trapped ion thermal energies as they are bombarded by a steady electron current. A study conducted at the Lawrence Livermore National Laboratory shows that the EBIT trapped ion thermal energies are principally determined by the applied trapping potentials V_{trap} [103].

$$k_B T_{ion} \approx 0.1 q V_{trap} \tag{8.1}$$

where k_B is the Boltzmann's constant, q and T_{ion} are the trapped ion charge state and temperature respectively. Further observations show [104, 105] that Equation (8.1) can vary by up to a factor of 4 due to the trapped ion space-charge effects, electron beam current and others sources [106]. More accurate measurements and their dependence on these parameters would be practical in obtaining a clearer image. These results would hence be used to determine the optimal parameter settings to minimize the ion temperature while obtaining the desired charged state before the extraction process. As observed during the RFQ extraction process (section 7.3.2), the EBIT extraction potential magnitude can further increase the longitudinal energy spread. Optimizing both the trapping and extraction processes without compromising the overall extracted beam quality will thus be vital in minimizing the extracted ion bunch overall longitudinal energy spread.

APPENDIX A
Concept of Energy Spread and Longitudinal Emittance

A.1 Emittance

Inside an ion beam, each ion has an unique position (x, y, z) and velocity (v_x, v_y, v_z) profile. As the beam propagates along the beamline, various forces (beam space charge, electric and magnetic fields from electrodes, etc.) will alter the ion's path, resulting in a new series of coordinates and velocities. To determine how these forces affect the beam, the emittance ϵ is employed to quantitatively measure the beam quality. The emittance is defined as the product of the beam width and divergence, where the divergence relates to the ion pulse velocity spread. Assuming that the moving ion electric and magnetic fields can be represented as average scalar $\psi(x, y, z)$ and vector potential $\mathbf{A}(x, y, z)$ respectively, the ion beam obeys Liouville's theorem, which states that the density of particle, n or equivalently, the volume V occupied by a given number of particles in a six-dimensional hyperspace (x, p_x, y, p_y, z, p_z) called phase space remains invariant [100] even if the shape of the phase space changes with time. If there is no coupling between momenta of different coordinates, the phase space can be separated into three invariant position-momentum spaces $(x, p_x), (y, p_y)$ and (z, p_z) [100]. For a beam travelling in the z-direction, the transverse emittance $\epsilon_\perp$ will be the areas in spaces (x, p_x) and (y, p_y) and the longitudinal emittance $\epsilon_\|$ is the area in space (z, p_z). For transverse emittance measurements in the non-relativistic regime, the position-velocity spaces (x, x') and (y, y') called trace-space are preferred (see Figure A–1). The conversion of momentum into velocity is

$$x' = \frac{dx}{dz} = \frac{\dot{x}}{\dot{z}} = \frac{p_x}{p_z} \simeq \frac{p_x}{p} \tag{A.1}$$

where $p = (p_x^2 + p_z^2)^{1/2}$ is the total momentum in the $x - z$ plane. The conversion procedure is repeated for the $y - z$ plane.

However, since the velocities x', y' are inversely proportional to the beam momentum p (see Equation (A.1)), the resulting emittances (x, x'),(y, y') scale with the beam energy. An emittance normalization is required to eliminate this dependence. The result is an energy-independent emittance, allowing for emittances at different beam energies to be compared unimpeded. Before proceeding, a more thorough definition of emittance is necessary.

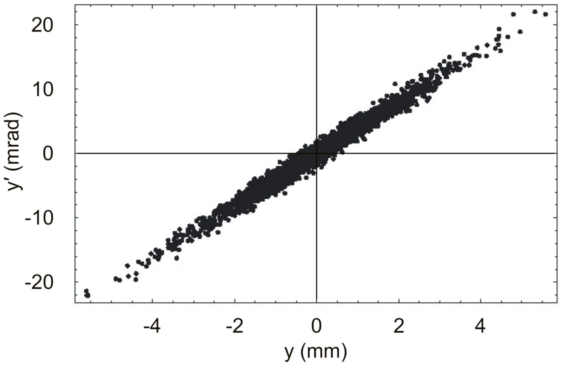

Figure A–1: Example of transverse emittance plot. Transverse emittance of an ion beam extracted from the TITAN RFQ with a ± 500 V pulse along the y-axis. The transverse emittance can be represented by an elliptical boundary surrounding the data and has units of π-mm-mrad. Taken from [41]

A.1.1 RMS Emittance

Lapostolle [107] and Sacherer [108] defined the rms (root-mean-squared) quantities (width, divergence, emittance, etc.) in order to observe differences in particle distributions. Assuming a particle distribution $n(x, y, x', y')$, two beams having the same particle composition, kinetic energy and current are said to be equivalent if the second moments (Equation (A.3)) of each distribution are the same [100]. In terms of rms quantities, the rms beam widths and rms transverse emittances are identical, assuming that both beams are compared at the same location within a beamline.

The rms beam width along the x-direction is defined as

$$x_{rms} = \langle x \rangle = \left(\langle x^2 \rangle \right)^{1/2} \tag{A.2}$$

where the second moment of the particle along the x-direction is defined as

$$\langle x^2 \rangle = \frac{\iiint \int x^2(x,y,x',y')dx\, dy\, dx'\, dy'}{\iiint \int n(x,y,x',y')dx\, dy\, dx'\, dy'} \tag{A.3}$$

This process can be repeated with each term ($\langle x' \rangle, \langle y' \rangle$, etc.). The rms emittance is then defined as

$$\langle \epsilon_x \rangle = \left(\langle x^2 \rangle \langle x^{'2} \rangle - \langle xx' \rangle^2 \right)^{1/2} \tag{A.4}$$

where $\langle xx' \rangle^2$ can be represented as the correlation between x and x' when the beam is focusing or diverging. In nomenclature, the emittance is expressed in units of $\pi - mm - mrad$ since the area enclosed by the beam in phase-space has an elliptical shape.

At this moment, the rms emittance can be normalized by introducing the factor $\beta\gamma$

$$\langle \epsilon_{nx} \rangle = \beta\gamma \langle \epsilon_x \rangle \tag{A.5}$$

where $\beta = v_z/c$ and $\gamma = 1/\sqrt{1-\beta^2}$.

The emittance does not remains constant along the beam's flightpath. The various non-conservative forces applied on the beam will break Liouville's theorem and lead to emittance growth. A primordial goal of experimentalists is to minimize and, if possible, negate any emittance growth. A smaller emittance translates to a better quality beam where the beam behaviour approaches that of a small finite diameter beam with no divergence.

A.2 Longitudinal Emittance

In a pulsed ion beam, where proper timing of ions pulses is vital to synchronize various instruments along a beamline, longitudinal emittance plays a crucial role. The longitudinal emittance is determined from the individual pulse profile in a similar fashion as the transverse emittance. In the momentum-position space (z, p_z), the rms longitudinal emittance $\langle \epsilon_z \rangle$ is defined as the product of the ion pulse longitudinal width $\langle \Delta z \rangle$ and longitudinal momentum spread $\langle \Delta p_z \rangle$ [100]

$$\langle \epsilon_z \rangle = \langle \Delta z \rangle \frac{\langle \Delta p_z \rangle}{p_0} \tag{A.6}$$

where $\Delta p_z = p_z - p_0$ and p_0 is the ion bunch average longitudinal momentum.

The normalized rms longitudinal emittance is expressed as [100]

$$\langle \epsilon_{nz} \rangle = \langle \Delta z \rangle \frac{\langle \Delta p_z \rangle}{mc} \tag{A.7}$$

In accelerator physics, the longitudinal emittance is commonly expressed as a function of the energy E and time t in lieu of the momentum p_z and position z (see Figure A–2). Using $z = v_0 \Delta t = \beta_0 c \Delta t$ and $\Delta p_z \simeq \Delta p = \Delta\gamma mc/\beta_0 = \Delta E/\beta_0 c$ where Δt and ΔE are the time and energy spreads respectively, the equivalent rms emittance $\langle \epsilon^*_{nz} \rangle$ is then [100]

$$\langle \epsilon^*_{nz} \rangle = \langle \Delta E \rangle \langle \Delta t \rangle \tag{A.8}$$

where $\langle \epsilon^*_{nz} \rangle$ and $\langle \epsilon_{nz} \rangle$ are related as

$$\langle \epsilon^*_{nz} \rangle = \langle \epsilon_{nz} \rangle mc \tag{A.9}$$

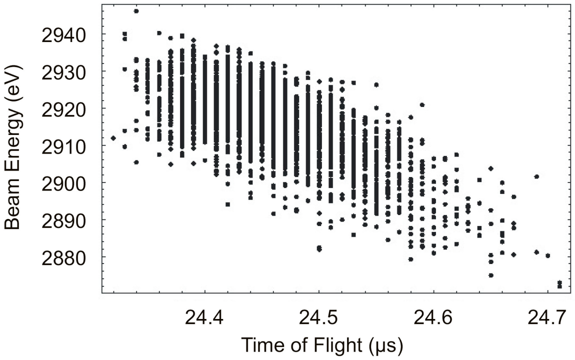

Figure A–2: Example of longitudinal emittance plot. Longitudinal emittance of an ion beam extracted from the TITAN RFQ with a ± 500 V pulse. Taken from [41].

A.3 Energy Spread

At the ion source, the ions are initially in a three-dimensional thermal equilibrium, $T_s = T_x = T_y = T_z$, where T_s corresponds to the single-temperature value at the source. The thermal energy is related to the energy spread as [100]

$$\langle \Delta E \rangle = m\langle v^2 \rangle = k_B T_s \tag{A.10}$$

where $\langle v \rangle$ is the rms thermal velocity and k_B is the Boltzmann constant. Ion extraction and acceleration from the ion source to high energies will break the thermal equilibrium due to a longitudinal cooling effect [109]. From the ion beam cylindrical symmetric, the temperature can be subdivided into a longitudinal $T_{\parallel}$ and a transversal $T_{\perp}$ component. The resulting longitudinal and transverse energy spreads are [100]

$$\langle \Delta E_{\perp} \rangle = k_B T_{\perp} = k_B T_x = m\langle v_x^2 \rangle = k_B T_y = m\langle v_y^2 \rangle \tag{A.11}$$

$$\langle \Delta E_{\parallel} \rangle = k_B T_{\parallel} = k_B T_z = m\langle \Delta v_z^2 \rangle \tag{A.12}$$

where $\Delta v_z = v_z - v_0$ is the difference between the ion longitudinal velocity v_z and the average ion pulse velocity v_0.

APPENDIX B
RFA Program

To synchronize all the necessary electronic equipment (see section 6.5) to perform an automated scan with the RFA and save the resulting data, a program was developed using LabVIEW software. From a set of initial scanning parameters, the RFA program will automatically configure the retarding mesh's ISEG power supply and MCS during the scan and save the resulting data to an remote server after the scan is completed.

B.1 RFA Web Server

Before running the RFA program, the software LabVIEW 8.6.1 (or higher) and National Instrument VISA 4.3 (or higher) Run-Time engines must be first installed on a dedicated internet enabled computer. The NI VISA Run-Time engine enables the LabVIEW software to work in conjunction with the Agilent LAN/GPIB gateway whereas the LabVIEW Run-Time engine is necessary to run the RFA program code. This computer serves as the RFA web server, permitting bi-directionality communication between the RFA's electronic and data acquisition systems, the RFA program and other computers by remote access to the program via a network connection.

B.1.1 Remote Access

The RFA web server and program can be remotely accessed from an internet enabled computer using an internet browser connected to the server's Internet Protocol (IP) address. As in the previous case, LabVIEW 8.6.1 (or higher) Run-Time engine must be installed on the remote computer to run the LabVIEW code. In addition, LabVIEW 8.5 Local VI execution browser plug-in must be installed to allow the browser to properly recognize and run the LabVIEW code imbedded in the webpage. When accessing the RFA program remotely, access privileges are automatically transferred from the server to the remote computer, preventing accidental simultaneous input from both computers. The server has access priority over the remote computer and can revoke it if necessary.

B.2 Software GUI

When using the RFA program or accessing it through an internet browser, an identical RFA graphical user interface (GUI) is presented, as shown in Figure B–1. The GUI is divided into five distinct tabs (Main, MCS, Containers, HV Stuff and MCS Channel), each controlling a different operational aspect.

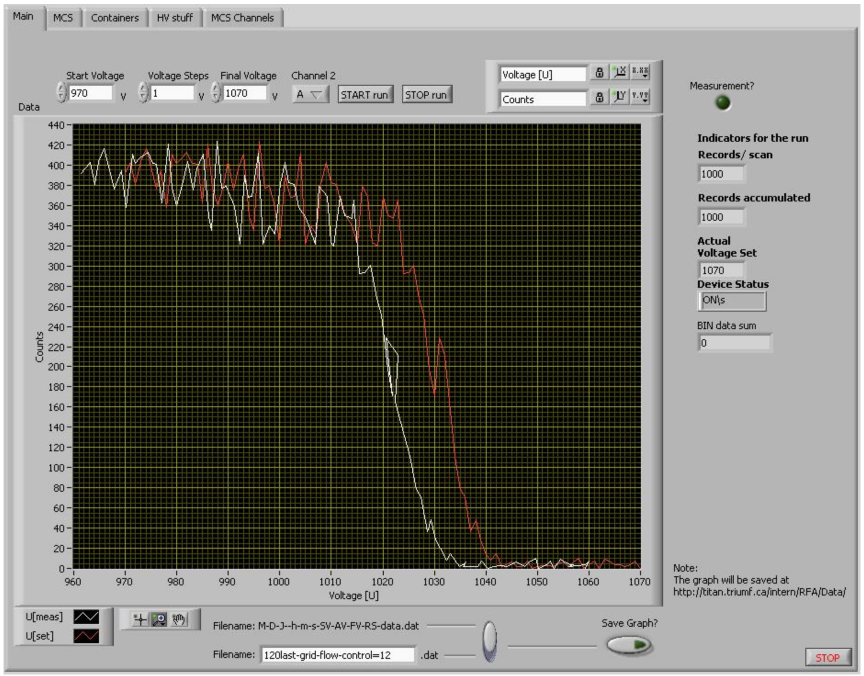

Start Voltage 970 V
Voltage Steps 1 V
Final Voltage 1070 V
Channel 2 A

Indicators for the run
Records/ scan 1000
Records accumulated 1000
Actual Voltage Set 1070
Device Status ON\s
BIN data sum 0

Note:
The graph will be saved at
http://titan.triumf.ca/intern/RFA/Data/

Filename: M-D-J--h-m-s-SV-AV-FV-RS-data.dat
Filename: 120last-grid-flow-control=12 .dat

Figure B–1: RFA Graphical User Interface (GUI). The RFA program is subdivided into five distinct tabs, controlling different aspects of the RFA electronic and data acquisition systems. The Main tab displays the overall status of the scan, including a plot of the ion counts (Counts) versus the retarding voltage (Voltage [U]).

B.2.1 Main

The Main tab is the primary tab that is used during a scan. The tab consists of a large graphical plot displaying the ion counts (Counts) along the y-axis and the retarding voltage

(Voltage [U]) along the x-axis surrounded by various scanning information, shown by the five different red boxes in Figure B–2.

In box 1, the initial voltage, final voltage and voltage steps for a scan are selected using the Start Voltage, Final Voltage and Voltage Steps boxes respectively. Channel 2 selects the retarding voltage output channel (A or B) on the ISEG power supply. The ”START run” button initiates the scan whereas the ”STOP run” button stops the scan before completion.

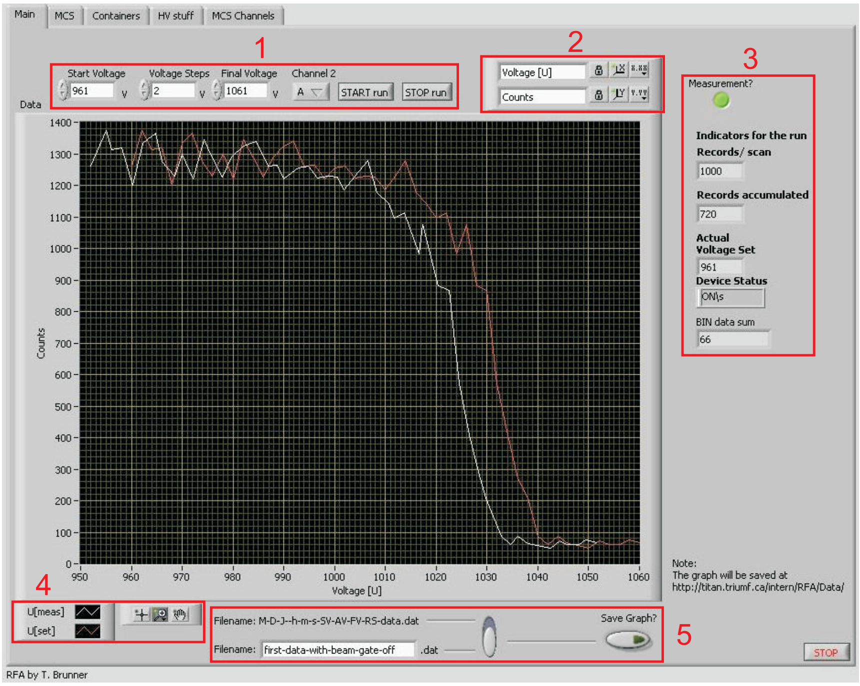

Start Voltage: 961 V
Voltage Steps: 2 V
Final Voltage: 1061 V
Channel 2: A
Voltage [U]
Counts
Measurement?
Indicators for the run
Records/ scan: 1000
Records accumulated: 720
Actual Voltage Set: 961
Device Status: ON\s
BIN data sum: 66
Note:
The graph will be saved at
http://titan.triumf.ca/intern/RFA/Data/
Filename: M-D-J--h-m-s-SV-AV-FV-RS-data.dat
Filename: first-data-with-beam-gate-off .dat
RFA by T. Brunner

Figure B–2: Example of an ongoing scan on the RFA’s Main Tab. The Main tab is surrounded by five separate control or information areas that are used during a scan. These included (1) scanning parameters, (2) graph options, (3) scan status, (4) plotting options and (5) filename options.

In box 2 are the graphing options. The top and bottom layers control the parameters along the x-axis and y-axis respectively. These parameters are respectively the axis label, autoscale (lock icon) with indicator (3D Cartesian plot with axis icon) and other parameters (X.XX icon) with format, precision, mapping mode and grid colour options. The graph ranges (x and y axes) can be manually changed by clicking on the end values of the axis of interest and inputting a new value manually. The lock icon must be in "unlocked mode" first before proceeding.

Box 3 shows the status for an ongoing scan. A running scan will illuminate the green circular icon underneath "Measurement?". Below this, the "Records/Scan" indicate the preset Records/Scan value selected on the MCS tab (see section B.2.2). The "Record accumulated" shows the current number of records acquired during one voltage step scan. For each voltage step, the record will begin at zero and increase until reaching the preset value in "Records/Scan" before resetting to zero and repeat the procedure with a new voltage step value. The "Actual Voltage Set" is the current retarding voltage setting sent from the RFA program to the ISEG power supply. The "Device Status" presents the status of the retarding mesh ISEG power supply; these vary between "ON/s", "H2L" and "L2H" for online, voltage decreasing and increasing respectively. The "BIN data sum" represents the accumulating number of ion counts measured during the voltage step scan.

In box 4 are the data plot options for "U[meas]" and "U[set]" which are the corrected retarding voltage V_{out} calculated from the Keithley multimeter voltage measurements V_{Div} (see section) and retarding voltage setting sent to the ISEG power supply by the RFA program respectively. Some options include the line width, style and colour. Further options such as a count/voltage reader, zoom and graph scrolling displacement can be selected by the crosshair, loop and hand icons respectively to the right.

In box 5 are two save filename format options to save the data after a scan is complete or stopped prematurely by the user. The top option format "M-D-J–h-m-s-SV-AV-FV-RS-data.dat" is interpreted as Month-Day-Year–hour-minute-second-Starting Voltage-Stopping Voltage-Final Voltage-Records/Scan-data.dat which is obtained from the computer's internal clock and the current scanning. The stopping voltage is the last voltage step taken before the scan is manually stopped or automatically completed. The lower option allows for a user-defined filename to be inputted and is save in .dat format. Either option is selected by the scrolling button to the right. The .dat file and a jpeg picture of the graph are saved by clicking "Save Graph?" button to the right. The .dat file includes the ISEG input (ISEG set) and corrected measured (2700 read) retarding voltages and the accumulated ion count (integrated counts) for each voltage step.

B.2.2 MCS

The MCS tab controls the necessary sections of the Mode (data acquisition parameters) and Levels (trigger and discriminator settings) menus on the multichannel scaler to perform voltage scans with the RFA. Starting from the left on Figure B–3, the ”Bin width” controls the time width of the bins, the ”Bins/Record” sets the number of bins available for a record. The time window for one record is the product of the bin width and bins/record and is shown in ”Measuring Time”. The MCS can only acquire data during this time window. The ”Records/Scan” is the number of records which are accumulated before the data acquisition is completed or in this case, one voltage step scan. The ”Tr. Offset” is the trigger offset which determines the number of bins that are skipped at the beginning of the record before data acquisition starts. The timing offset is the product of the bin width and the trigger offset. The ”Accum. Mode” is the accumulation mode of the MCS. For this experiment, the ”add” mode is selected to accumulate ion counts for each record during one voltage step scan.

The trigger and discriminator levels select the minimum voltage pulse amplitude to trigger the start of a record and count of an ion pulse respectively. The latter is used to filter out lower voltage pulse signals originating as thermal noise from the MCP. The trigger and discriminator slopes select the direction of the pulse (raising or falling) depending on the signal pulse polarity (positive or negative). In this experiment, both raising slopes are selected.

To set the parameters on the MCS tab, input all the necessary values for each parameter and select ”SET” below each parameter title. Press the rectangular green button below ”GO” to save these new settings on the MCS. Return all ”SET” buttons to ”READ” and click the green button again to confirm the new settings.

B.2.3 Containers

The Containers tab contains the status information of the various electronic hardware connected to the RFA program via the Agilent GPIB/IP interface. No modifications of any

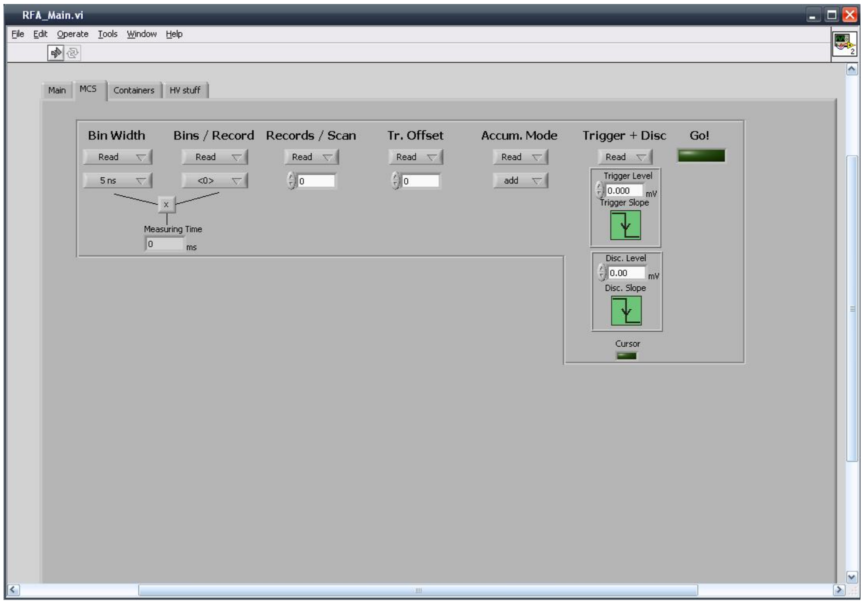

Bin Width: 5 ns
Bins / Record: <0>
Records / Scan: 0
Tr. Offset: 0
Accum. Mode: add
Measuring Time: 0 ms
Trigger Level: 0.000 mV
Disc. Level: 0.00 mV

Figure B–3: The MCS Tab. A select group of MCS parameters are remotely controlled from this tab, necessary for the operation of the RFA scan.

options presented here are necessary during the experiment. All green circular icons beside the electronic hardware must be illuminated before a scan can proceed.

B.2.4 HV Stuff

The HV Stuff tab controls a select number of parameters on the retarding mesh's ISEG power supply necessary for the proper operation of the scanning process (see Figure B–4). These include the voltage ramp speed (V/s), the retarding voltage output channel (A or B) and the applied voltage on the retarding mesh. To set either the voltage ramp speed or the voltage set, select the value on "Voltage Ramp SET" and "Voltage SET" respectively. To the right of these boxes, select "SET" then "READ" to set and confirm the new setting on the power supply. The new values should appear to the left of the input boxes, with the "Voltage SET" value requiring some time to reach its set value due to the voltage ramp speed.

The voltage and current as a function of the percentage of the maximum voltage and current respectively can be viewed by selecting "READ" on the "Maximum Voltage" and "Maximum Current" boxes. Similarly, the current in amperes can be viewed in the "Actual Current" box.

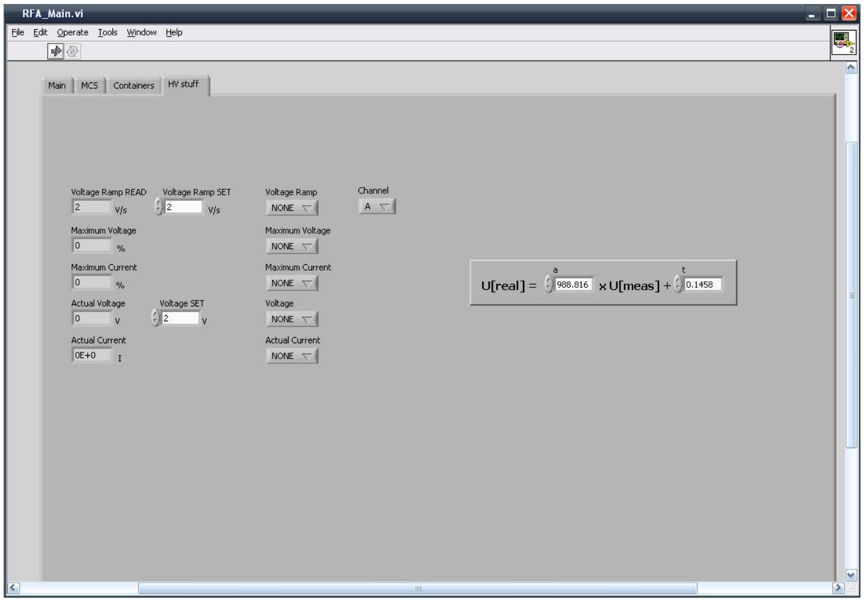

Voltage Ramp READ: 2 V/s
Voltage Ramp SET: 2 V/s
Voltage Ramp: NONE
Channel: A
Maximum Voltage: 0 %
Maximum Voltage: NONE
Maximum Current: 0 %
Maximum Current: NONE
Actual Voltage: 0 V
Voltage SET: 2 V
Voltage: NONE
Actual Current: 0E+0 I
Actual Current: NONE

U[real] = a 988.816 x U[meas] + t 0.1458

Figure B–4: The HV Stuff Tab controls a few key parameters on the retarding mesh ISEG power supply. The slope and y-intercept values obtained from the linear curve fit performed on the HV divider box (see section B.2.1) are incorporated here to calculate the real voltage (U[real]) from the measured voltage (U[meas]).

On the right, the slope and y-intercept of the linear calibration curve for the HV divider box (see section B.2.1) are input here to calculate the real retarding voltage ”U[real]” from the measured retarding voltage ”U[meas]” from the Keithley multimeter. It is to note that the ”U[meas]” seen in the Main tab (see section B.2.1) is actually ”U[real]”, the result of a typographical error during programming.

B.2.5 MCS Channels

The MCS Channels tab presents a plot of the ion counts as a function of the bin number as physically displayed on the MCS (see Figure B–5). The accumulated TOF spectra for each voltage step during a scan can be reviewed by selecting the run number, starting from zero and increasing. The adjoining retarding voltage is shown beside in ”Voltage 2” for reference purposes. Graphing options are available and identical to those found in the Main tab. The tab is primarily used to visually ensure that the trigger offset is properly set to acquire the ion pulses within the narrow data acquisition time window of the MCS.

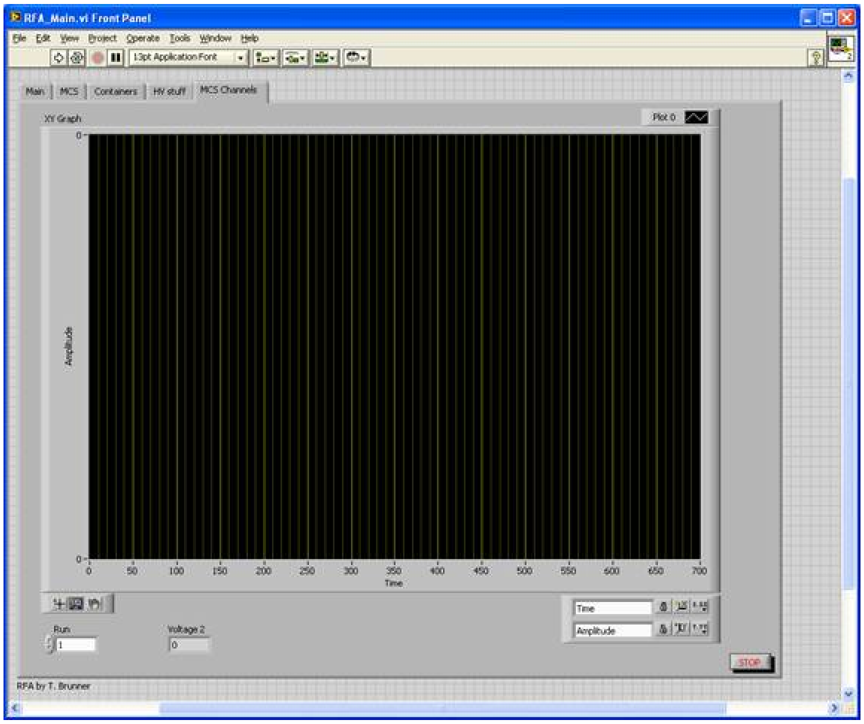

Run: 1

Voltage 2: 0

Figure B–5: The MCS Channel Tab displays the TOF spectra of each voltage step during a scan. The associated retarding voltage is also shown for reference.

B.3 Scanning Procedure

1. After all electrical connections are properly attached and secured, as shown by the RFA circuit diagram (Figure 6–6), turn on the Stanford Research System SR430 multichannel scaler, the Agilent E5810A LAN/GPIB gateway and the Keithley 2700 multimeter/data acquisition. The order that this task is performed is unimportant.
2. Assure that the gateway is connected to the Ethernet and that a designated IP address is present on the front display.
3. Before turning on the ISEG power supplies for the RFA and MCP, ensure that all 10-turn potentiometers are set to 0 V and the Control toggle switch (CONTR) is set up. Note the output channels (A or B) employed on the retarding mesh and MCP power supplies.
4. Once the pressure in the vacuum chamber where the RFA is located drops below 10^{-6} Torr, slowly raise the applied potential on the middle and rear plates of the MCP from ground to

1,800 V and 2,000 V respectively. Make sure that the potential different between the plates is always kept below 300 V while raising and lowering the potentials, with the rear potential always higher than the middle potential, to avoid possible damage on the active surface due to electrical discharge.

5. On the MCS, set the parameters to the values shown in Table B–1. Most of these values can be subsequently adjusted via the MCS tab on the RFA program if required.

Table B–1: MCS initial parameter settings

Bin width	5 ns
Records/scan	1000
Bins/record	1k (1024 bits)
Trigger level	1.000 V
Trigger slope	Rising
Discriminator slope	Rising

6. Set the discriminator level on the MCS (see section B.3.1).
7. After lowering the RFA into the beamline, set the trigger offset (see section B.3.2) on the MCS. If the ion counts are too low or high, adjust ”Records/scan” value and/or the beam current to compensate.
8. Set manually the applied potentials on the RFA's outer meshes using the corresponding ISEG power supplies.
9. Start the RFA program by double-click on the ”RFA-V1.0” icon on the RFA web server. A window called ”RFA_Main.vi” should appear shortly afterwards. This program must be running on the server to enable remote access from other computer to control the RFA.
10. Make sure that the RFA web server is logged into the TITAN web server since all scan data are saved on the latter.

The following steps can be performed either on the RFA program itself or using the RFA GUI on an internet browser on a remote computer connected to the RFA web server.

11. Check that all electronic hardware are online in the Containers tab.

12. Check that all parameters on the MCS tab to confirm initial manual input settings (Table B–1).
13. On the HV Stuff tab, input slope and y-intercept values obtained from linear curve fit calibration on HV divider box from section B.2.1.
14. Select the retarding voltage output channel found earlier in "Channel" on the HV Stuff tab.
15. Toggle the Control switch on the retarding mesh's ISEG power supply to DAC for remote control.
16. Set the "Voltage SET" value slightly below the beam energy used in the scan and select an appropriate voltage ramp speed to reduce the necessary time to reach the "Voltage SET" value on the retarding mesh.
17. Read the maximum current on the HV Stuff tab to check if no short circuit are present on the retarding mesh.
18. Returning to the Main tab, select the Start Voltage, Voltage Steps, Final Voltage and the same output channel as in the HV Stuff tab.
19. Select the preferred filename option.
20. Start the scan by clicking "START run" button
21. After scan is completed, click "Save Graph?" to insure a graph and data file are saved.
22. Repeat items 16 - 21 for each new scan using the same element and beam energy and item 7 if the beam energy and/or composition changes.

B.3.1 MCS Discriminator Level

To remove dark counts coming from the MCP due to thermal noise, assure that no ion beam is on the RFA and that the HV is applied on the MCP. After setting the discriminator level to 0 mV on the MCS, press "Start" on the front keypad to start the scan. After a few seconds, the scan should terminate at 1,000 records. If not, simply press the "Stop/Reset" button once. To determine the number of dark counts during the scan, press the "Math" button followed by "Stats" and "Do stats" on the soft keys. The total counts will be shown on the bottom of the display beside "Total". If the total is significantly larger than 0, repeat the preceding steps while slightly increasing the discriminator level by a few mV. To reset the MCS for the next scan, press ”Stop/Reset” a second time. Repeat this procedure until the total reaches 0.

B.3.2 MCS Trigger Offset

To set up the timing delay of the MCS to compensate for the time difference between the RFQ extraction trigger signal and the impact signal from the MCP, first ensure that the RFA is extended into the beamline and an ion beam is directed on the RFA. Lower the retarding potential if not previously done to allow ions to reach the MCP. Disconnect both the LeCroy 222 Dual gate generator and the MCP cables from the Trigger and the Signal input BNC connectors respectively on the MCS and reconnect them to two separate channels on a digital oscilloscope. After adjusting the scale settings on the oscilloscope, measure the time difference between the two pulses. Return to the MCS and press the ”Mode” button followed by the ”Trigger Offset” soft key to enter the timing delay found on the oscilloscope using the spin knob. Reconnect the cables to the MCS and perform a short scan by pressing ”Start”. The ion count distribution from the MCP should approximately be centred on the display screen. If not, return to the ”Trigger Offset” mode and readjust the input value slightly for more or less delay and re-scan to confirm centering. This procedure is required for each alteration of the beam energy and composition to a previously unmeasured configuration due to changes in the TOF of the pulsed ions. However, once the time delay value is acquired, only minute changes are subsequently needed from this value when returning to a previous beam configuration.

APPENDIX C
Technical Drawings

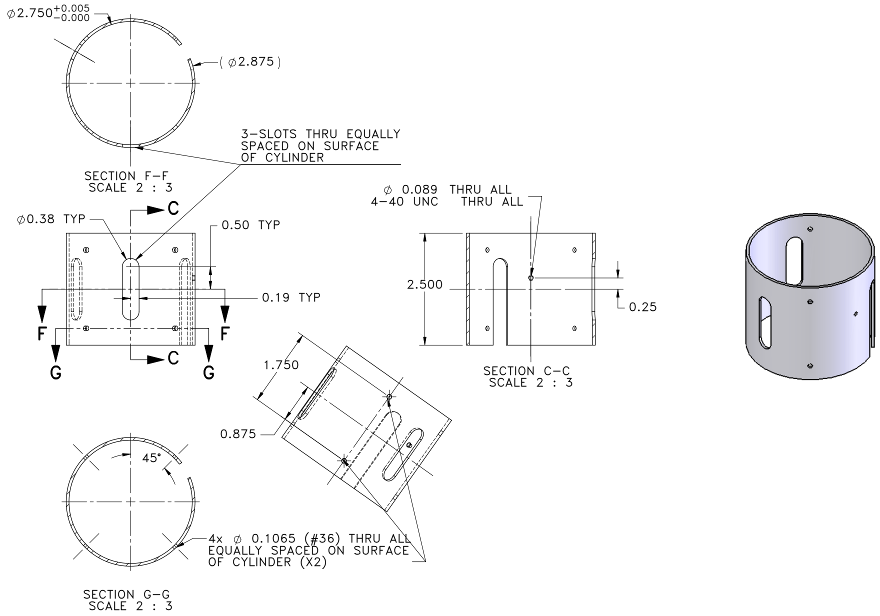

Figure C–1: Technical drawing of the RFA cylindrical shell. All measurements are in inches

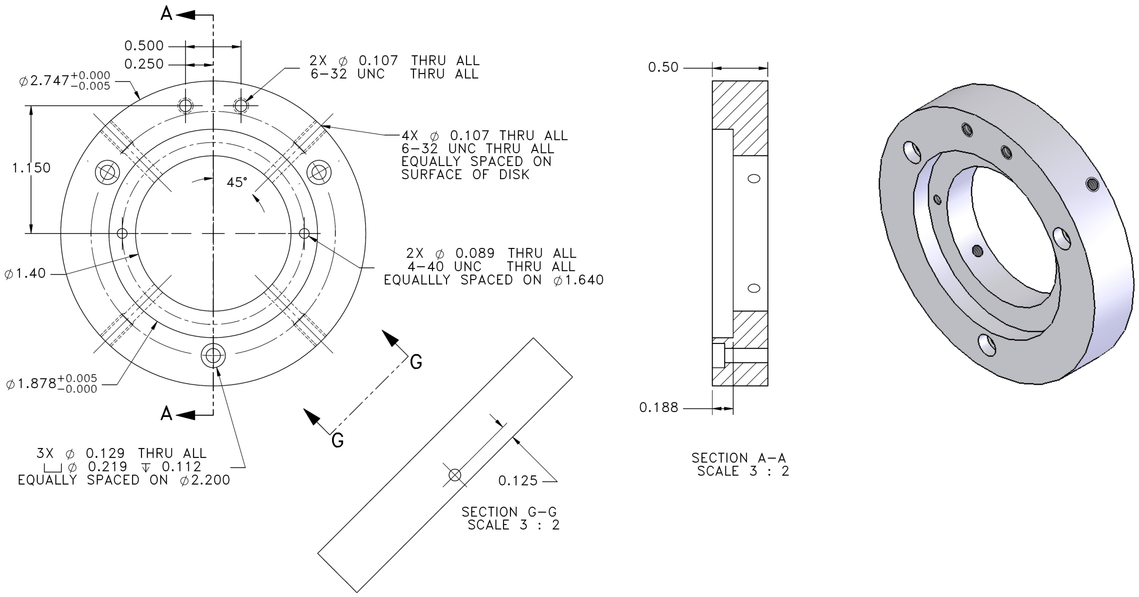

Figure C–2: Technical drawing of the RFA front disk. All measurements are in inches

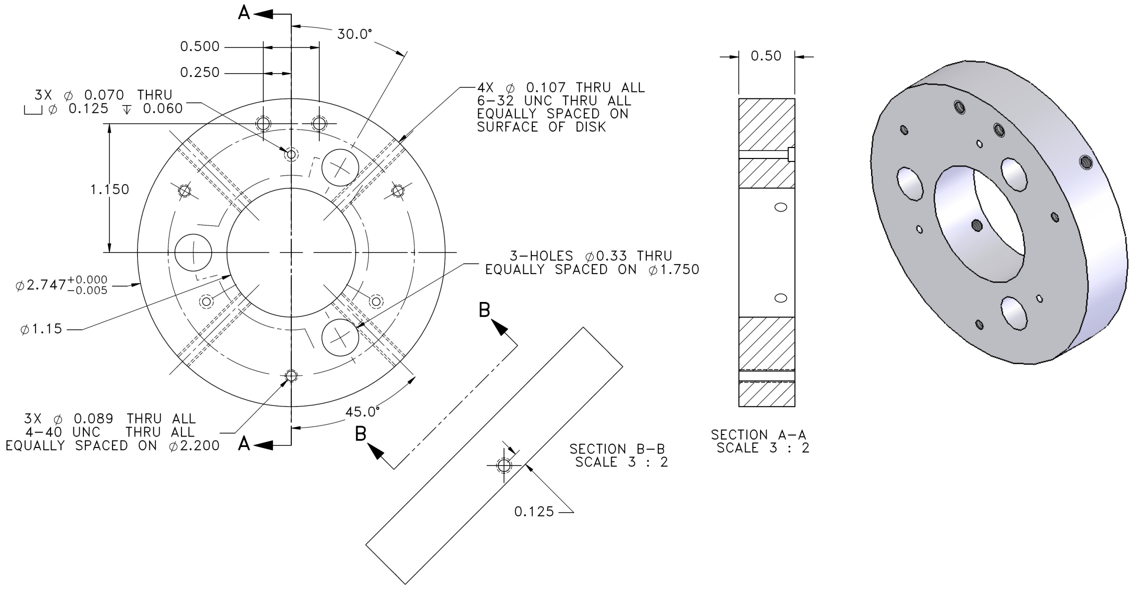

Figure C–3: Technical drawing of the RFA rear disk. All measurements are in inches

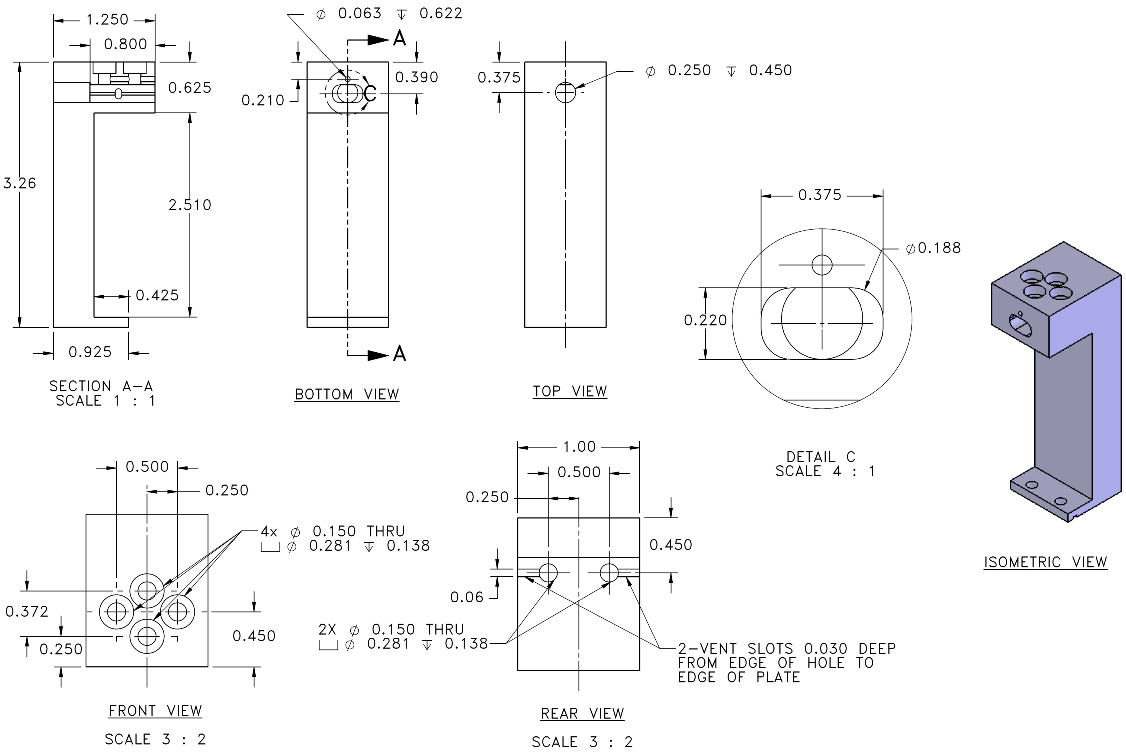

Figure C–4: Technical drawing of the RFA bracket. All measurements are in inches

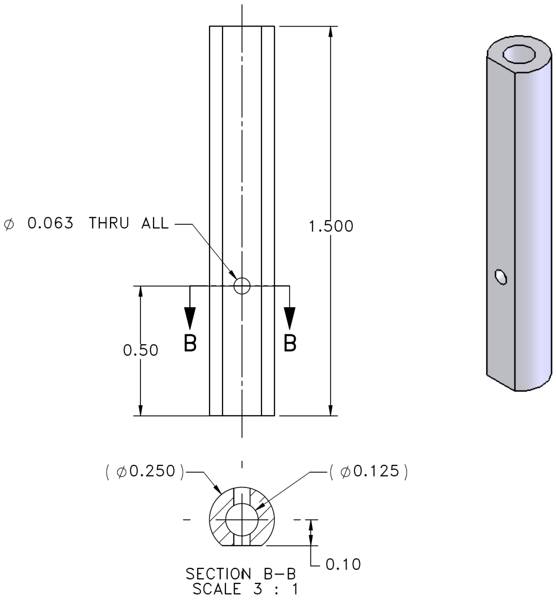

Figure C–5: Technical drawing of one of the three RFA ceramic tubes. All measurements are in inches

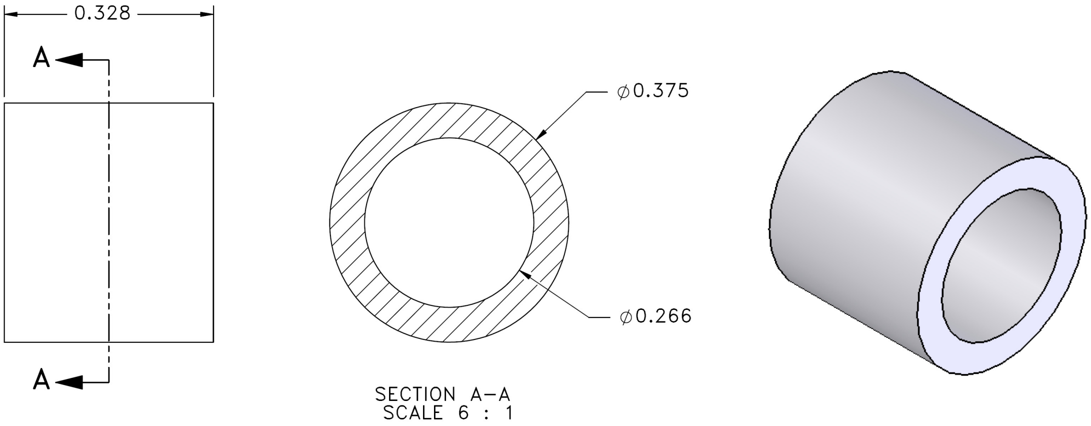

Figure C–6: Technical drawing of one of the twelve RFA MACOR spacers. All measurements are in inches

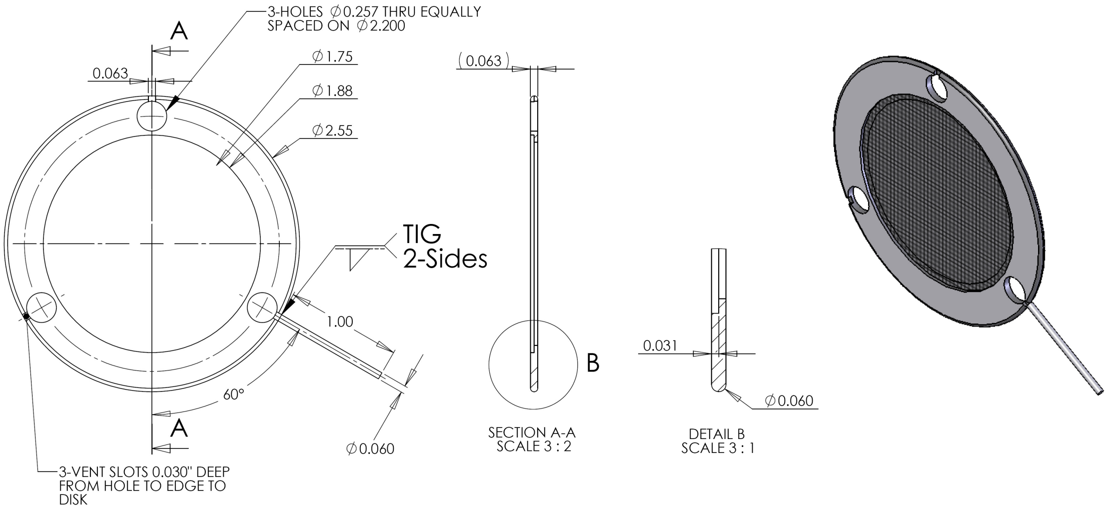

Figure C–7: Technical drawing of one of the three RFA mesh disks with electrode stub. All measurements are in inches

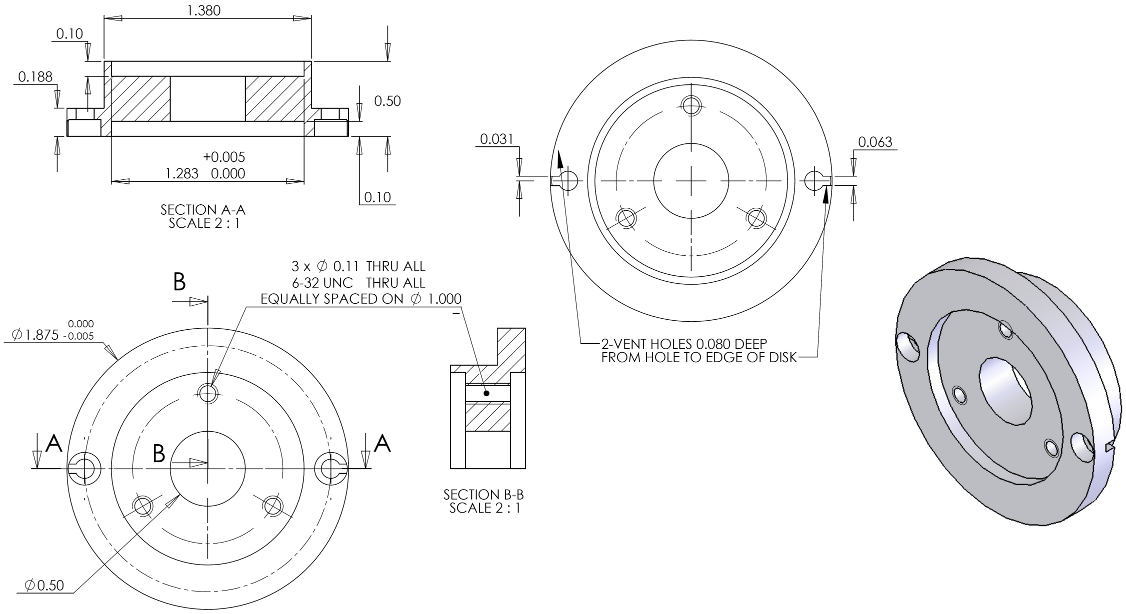

Figure C–8: Technical drawing of the RFA removable front plate. All measurements are in inches

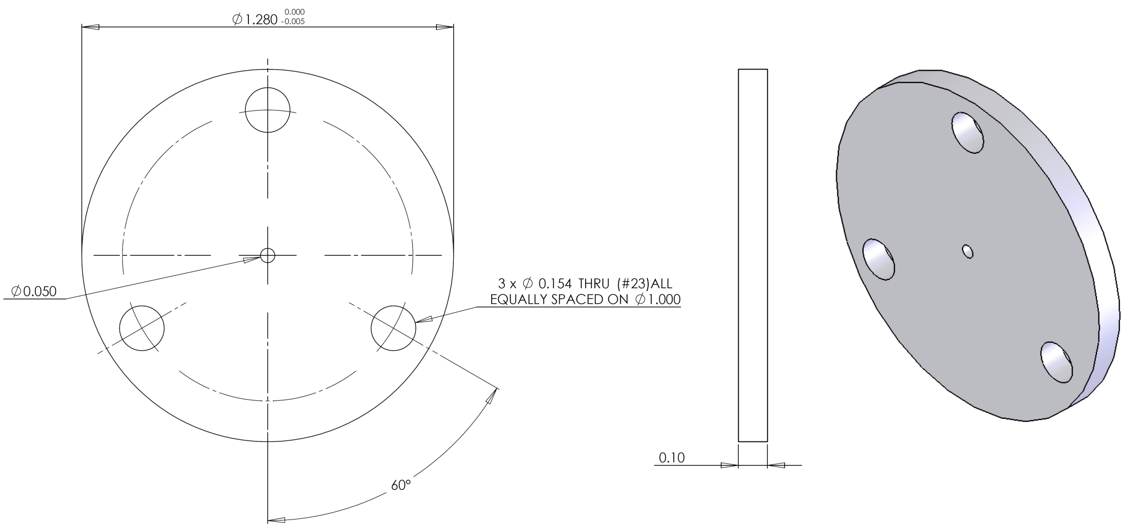

Figure C–9: Technical drawing of one of the two RFA removable slit plates. All measurements are in inches

REFERENCES

[1] E. Comay, I. Kelson, and A. Zidon.

[2] The TITAN beamline. `http://titan.triumf.ca/equipment/Beamline-schematic.jpg`.

[3] January 2007 - small jpg - 3d of isac. `http://legacyweb.triumf.ca/isac/2007-01-24/is-24jan2007-t.jpg`.

[4] TITAN EBIT schematics. `https://titan.triumf.ca/intern/archive/EBIT/schematicsEBITwithPotential.jpg`.

[5] J. Dilling. The ISAC facility at TRIUMF and mass measurements with TITAN. `https://titan.triumf.ca/intern/archive/talks/JDilling_ISOLDE2006pic.ppt`, 2006.

[6] J. Dilling, R. Baartman, P. Bricault, M. Brodeur, L. Blomeley, F. Buchinger, J. Crawford, J.R. Crespo López-Urrutia, P. Delheij, M. Froese, G.P. Gwinner, Z. Ke, J.K.P. Lee, R.B. Moore, V. Ryjkov, G. Sikler, M. Smith, J. Ullrich, and J. Vaz. Mass measurements on highly charged radioactive ions, a new approach to high precision with TITAN. *Inter. J. Mass Spec.*, 251:198–203, 2006.

[7] K. S. Krane. *Introductory Nuclear Physics.* John Wiley & Sons, Inc., 1988.

[8] K. Heyde. *Basic Ideas and Concepts in Nuclear Physics: An Introduction Approach.* Series in Fundamental and Applied Nuclear Physics. CRC Press, 3 edition, 2004.

[9] D. Lunney, J. M. Pearson, and C. Thibault. Recent trends in the determination of nuclear masses. *Rev. Mod. Phys.*, 75:1021–1082, 2003.

[10] G. Audi, A. H. Wapstra, and C. Thibault. The AME 2003 atomic mass evaluation: (II). tables, graphs and references. *Nucl. Phys. A*, 729:337–676, 2003.

[11] M. J. Smith. *A mass measurement of the short-lived halo nucleus* ^{11}*Li with the TITAN Penning trap spectrometer.* PhD thesis, University of British Columbia, 2008.

[12] P. G. Hansen, A. S. Jensen, and B. Jonson. Nuclear halos. *Ann. Rev. Nul. Part. Sci.*, 45:591–634, 1995.

[13] W. Geithner, S. Kappertz, M. Keim, P. Lievens, R. Neugart, L. Vermeeren, S. Wilbert, V. N. Fedoseyev, U. Köster, V. I. Mishin, V. Sebastian, and ISOLDE Collaboration. Measurement of the magnetic moment of the one-neutron halo nucleus ^{11}Be. *Phys. Rev. Lett.*, 83:3792–3795, 1999.

[14] I. Tanihata, D. Hirata, T. Kobayashi, S. Shimoura, K. Sugimoto, and H. Toki. Revelation of thick neutron skins in nuclei. *Phys. Lett. B*, 289:261–266, 1989.

[15] I. Tanihata, T. Kobayashi, O. Yamakawa, S. Shimoura, K. Ekuni, K. Sugimoto, N. Takahashi, T. Shimoda, and H. Sato. Measurement of interaction cross sections using isotope beams of Be and B and isospin dependence of the nuclear radii. *Phys. Lett. B*, 206:592–596, 1988.

[16] V. L. Ryjkov, M. Brodeur, T. Brunner, M. Smith, R. Ringle, A. Lapierre, F. Ames, P. Bricault, M. Dombsky, P. Delheij, D. Lunney, M. R. Pearson, and J. Dilling. Direct mass measurement of the four-neutron halo nuclide ^{8}He. *Phys. Rev. Lett.*, 101:012501, 2008.

[17] I. Tanihata. Neutron halo nuclei. *J. Phys. G: Part. Phys.*, 22:157–198, 1996.

[18] D. J. Griffiths. *Introduction to Quantum Mechanics.* Prentice Hall, 2 edition, 2004.

[19] E.M. Burbidge, G.R. Burbidge, W.A. Fowler, and F. Hoyle. Synthesis of the elements in stars. *Rev. Mod. Phys.*, 29:547–650, 1957.

[20] M. S. Smith and K. E. Rehm. Nuclear astrophysics measurements with radioactive beams. *Ann. Rev. Nul. Part. Sci.*, 51:91–130, 2001.

[21] K. Langanhke and M. Wiescher. Nuclear reactions and stellar processes. *Rep. Prog. Phys.*, 64:1657 – 1701, 2001.

[22] N. Cabibbo. Unitary symmetry and leptonic decays. *Phys. Rev. Lett.*, 10:531–533, 1963.

[23] M. Kobayashi and T. Maskawa. CP-violation in the renormalizable theory of weak interaction. *Progress of Theoretical Physics*, 49:652–657, 1973.

[24] I. S. Towner and J. C. Hardy. The evaluation of V_{ud}, experiment and theory. *J. Phys. G: Nucl. Part. Phys.*, 29:197–211(15), 2003.

[25] S. Eidelman et al. Review of particle physics. *Phys. Lett. B*, 592:1 – 5, 2004.

[26] J. C. Hardy and I. S. Towner. New limits on fundamental weak-interaction parameters from superallowed beta decay. *Phys. Rev. Lett.*, 94:092502, 2005.

[27] I. S. Towner and J. C. Hardy. Improved calculation of the isospin-symmetry-breaking corrections to superallowed Fermi beta decay. *Phys Rev. C.*, 77:025501, 2008.

[28] W-M Yao *et al.* Review of particle physics. *J. Phys. G: Nul. Part. Phys.*, 33:1–1232, 2006.

[29] The Canadian Penning] Trap Spectrometer at Argonne, author = G. Savard and R.C. Barber and C. Boudreau and F. Buchinger and J. Caggiano and J. Clark and J.E. Crawford and H. Fukutani and S. Gulick and J.C. Hardy and A. Heinz and J.K.P. Lee and R.B. Moore and K.S. Sharma and J. Schwartz and D. Seweryniak and G.D. Sprouse and J. Vaz, journal = Hyper. Inter., volume = 132, pages = 221-228, year = 2001.

[30] G. Savard, F. Buchinger, J. A. Clark, J. E. Crawford, S. Gulick, J. C. Hardy, A. A. Hecht, J. K. P. Lee, A. F. Levand, N. D. Scielzo, H. Sharma, K. S. Sharma, I. Tanihata, A. C. C. Villari, and Y. Wang. Q value of the superallowed decay of ^{46}V and its influence on V_{ud} and the unitarity of the Cabibbo-Kobayashi-Maskawa matrix. *Phys. Rev. Lett.*, 95:102501, 2005.

[31] J. Dilling, P. Bricault, M. Smith, and H. J. Kluge. The proposed TITAN facility at ISAC for very precise mass measurements on highly charged short-lived isotopes. *Nul. Instr. and Meth. in Phys. Res. B*, 204:492–496, 2003.

[32] G. Bollen. Mass measurements of short-lived nuclides with ion traps. *Nucl. Phys. A*, 693:3–18, 2001.

[33] K. Blaum and F. Herfurth. *Trapped Charged Particles and Fundamental Interactions*, volume 749 of *Lecture Notes in Physics*, chapter 5, pages 1–36. Springer Berlin / Heidelberg, 2008.

[34] J. M. Poutissou. The new radioactive beam facility at TRIUMF. pages 99–53. World Scientific Publishing, 2000.

[35] D. A. Hutcheon, S. Bishop, L. Buchmann, M. L. Chatterjee, A. A. Chen, J. M. D'Auria, S. Engel, D. Gigliotti, U. Greife, D. Hunter, A. Hussein, C. C. Jewett, N. Khan, M. Lamey,

A. M. Laird, W. Liu, A. Olin, D. Ottewell, J. G. Rogers, G. Roy, H. Sprenger, and C. Wrede. The DRAGON facility for nuclear astrophysics at TRIUMF-ISAC: design, construction and operation. *Nul. Instr. and Meth. in Phys. Res. A*, 498:190–210, 2003.

[36] C. Ruiz, F. Sarazin, L. Buchmann, T. Davinson, R. E. Azuma, A. A. Chen, B. R. Fulton, D. Groombridge, L. Ling, A. Murphy, J. Pearson, I. Roberts, A. Robinson, A. C. Shotter, P. Walden, and P. J. Woods. Strong resonances in elastic scattering of radioactive ^{21}Na on protons. 65:042801, 2002.

[37] R. E. Laxdal, W. Andersson, P. Bricault, I. Bylinskii, K. Fong, M. Marchetto, A. K. Mitra, R. L. Poirier, W. R. Rawnsley, P. Schmor, I. Sekachev, G. Stanford, G. Stinson, and V. Zviagintsev. Status of the ISAC-II accelerator at TRIUMF. pages 2003–2005. IEEE, 2005.

[38] B. Davids and C. N. Davids. EMMA: A recoil mass spectrometer for ISAC-II at TRIUMF. *Nucl. Instr. and Meth. in Phys. Res. A*, 544:565–576, 2005.

[39] C. E. Svensson, P. Amaudruz, C. Andreoiu, A. Andreyev, R. A. E. Austin, G. C. Ball, D. Bandyopadhyay, A. J. Boston, R. S. Chakrawarthy, A. A. Chen, R. Churchman, T. E. Drake, P. Finlay, P. E. Garrett, G. F. Grinyer, G. Hackman, B. Hyland, B. Jones, R. Kanungo, R. Maharaj, J. P. Martin, D. Morris, A. C. Morton, C. J. Pearson, A. A. Phillips, J. J. Ressler, R. Roy, F. Sarazin, M. A. Schumaker, H. C. Scraggs, M. B. Smith, N. Starinsky, J. J. Valiente-Dobon, J. C. Waddington, and L. M. Watters. TIGRESS: TRIUMF-ISAC gamma-ray escape-suppressed spectrometer. *J. Phys. G: Nucl. Part. Phys.*, 31:S1663–S1668, 2005.

[40] P. G. Bricault, M. Dombsky, P. W. Schmor, and G. Stanford. Radioactive ion beams facility at TRIUMF. *Nul. Instr. and Meth. in Phys. Res. B*, 126:231–235, 1997.

[41] M. J. Smith. A square-wave-driven radiofrequency quadrupole cooler and buncher for TITAN. Master's thesis, University of British Columbia, 2005.

[42] M. Brodeur. Towards high precision mass measurement of short-lived exotic isotopes using highly charged ions at the TITAN Penning trap system. Master's thesis, University of British Columbia, 2006.

[43] G. Sikler, J. R. Crespo López-Urrutia, J. Dilling, S. Epp, C. J. Osborne, and J. Ullrich. A high-current EBIT for charge-breeding of radionuclides for the TITAN spectrometer. *Eur. Phys. J. A*, 25:63–64, 2005.

[44] M. A. Levine, R. E. Marrs, J. N. Bardsley, P. Beiersdorfer, C. L. Bennett, M. H. Chen, T. Cowan, D. Dietrich, J. R. Henderson, D. A. Knapp, A. Osterheld, B. M. Penetrante, M. B. Schneider, and J. H. Scofield. The use of an electron beam ion trap in the study of highly charged ions. *Nucl. Instr. and Meth. in Phys. Res. B*, 43:431, 1989.

[45] B. M. Penetrante, J. N. Bardsley, M. A. Levine, D. A. Knapp, and R. E. Marrs. Evaporative cooling of highly charged dysprosium ions in an enhanced electron-beam ion trap. *Phys. Rev. A*, 43:4873–4882, 1991.

[46] M. Froese. The TITAN electron beam ion trap: Assembly, characterization, and first tests. Master's thesis, University of Manitoba, 2006.

[47] J. Bernard, J. Alonso, T. Beier, M. Block, S. Djekic, H. J. Kluge, C. Kozhuharov, W. Quint, S. Stahl, T. Valenzuela, J. Verdú, M. Vogel, and G. Werth. Electron and positron cooling of highly charged ions in a cooler Penning trap. *Nucl. Instr. and Meth. in Phys. Res. A*, 532:224–228, 2004.

[48] V. L. Ryjkov, L. Blomeley, M. Brodeur, P. Grothkopp, M. Smith, P. Bricault, F. Buchinger, J. Crawford, G. Gwinner, J. Lee, J. Vaz, G. Werth, J. Dilling, and the TITAN Collaboration. TITAN project status report and a proposal for a new cooling method of highly charged ions. *Eur. Phys. J. A*, 25:53–56, 2005.

[49] Z. Ke, W. Shi, G. Gwinner, K. Sharma, S. Toews, J. Dilling, V. L. Ryjkov, and the TITAN Collaboration. A cooler ion trap for the TITAN on-line trapping facility at TRIUMF. *Hyper. Inter.*, 173:103–111, 2006.

[50] G. Gwinner. The TITAN ion trap facility at TRIUMF. `http://www.physics.umanitoba.ca/~gwinner/pmwiki/pmwiki.php?n=Main.Titan`, 2007.

[51] G. Savard and G. Werth. Precision nuclear measurements with ion traps. *Annu. Rev. Nucl. Part. Sci.*, 50:119–152, 2000.

[52] J. L. Wiza. Microchannel plate detectors. *Nuc. Instr. Meth.*, 162:587 – 601, 1979.

[53] M. Smith, M. Brodeur, T. Brunner, S. Ettenauer, A Lapierre, R. Ringle, V. L. Ryjkov, F. Ames, P. Bricault, G. W. F. Drake, P. Delheij, D. Lunney, F. Sarazin, and J. Dilling. First Penning-trap mass measurement of the exotic halo nucleus ^{11}Li. *Phys. Rev. Lett.*, 101:202501, 2008.

[54] H. J. Kluge T. Otto M. König, G. Bollen and J. Szerypo. Quadrupole excitation of stored ion motion at the true cyclotron frequency. *Int. J. Mass. Spectr. Ion. Proc.*, 142:95, 1995.

[55] D. A. Bromley. *Treatise on heavy-ion science, high-energy atomic physics*, volume 5. Plenum Press New York, 1985.

[56] G. Bollen, S. Becker, H. J. Kluge, M. König, R. B. Moore, T. Otto, H. Raimbault-Hartmann, G. Savard, L. Schweikhard, and H. Stolzenberg. ISOLTRAP: A tandem Penning trap system for accurate on-line mass determination of short-lived isotopes. *Nucl. Instr. and Meth. in Phys. Res. A*, 368:675–697, 1996.

[57] E. W. Otten. *Treatise on Heavy-Ion Science*, volume 8, page 517. New York : Plenum, 1989.

[58] W. Demtröder. *Laser Spectroscopy*, volume 2. Springer-Verlag Berlin Heidelberg, 4 edition, 2008.

[59] S.L. Kaufman. High-resolution laser spectroscopy in fast beams. *Opt. Commun.*, 17:309, 1976.

[60] W. H. Wing, G. A. Ruff, W. E. Lamb Jr., and J. J. Spezewski. Observation of the infrared spectrum of the hydrogen molecular ion HD^{+}.

[61] J. R. Lakowicz. *Principles of Fluorescence Spectroscopy.* Springer, 3 edition, 2006.

[62] W. B. Hanson, D. R. Frame, and J. E. Midgley. Errors in retarding potential analyzers caused by nonuniformity of the grid-plane potential. *J. Geophys. Res.*, 77:1914–1922, 1972.

[63] Y. Sakai and I. Katsumata. An energy resolution formula of a three plane grids retarding field energy analyzer. *J. Phys. Soc. Jpn.*, 24:337–341, 1985.

[64] J. A. Simpson. Design of retarding field energy analyzers. *Rev. Sci. Instr.*, 32:1283–1293, 1961.

[65] H. Wollnik. *Optics of Charged Particles.* Academic Press Inc., 1987.

[66] M. Smith, L. Blomeley, P. Delheij, and J. Dilling. First tests of the TITAN digital RFQ beam cooler and buncher. *Hyperfine Inter.*, 173:171–180, 2006.

[67] H. D. Hagstrum. Theory of Auger ejection of electrons from metals by ions. *Phys. Rev.*, 96:336–365, 1954.

[68] H.P. Winter and J. Burgdörfer, editors. *Slow Heavy-Particle Induced Electron Emission from Solid Surfaces*, volume 225 of *Springer Tracts in Modern Physics*. Springer, 12 edition, 2007.

[69] A. Arnau, F. Aumayr, P. M. Echenique, M. Grether, W. Heiland, J. Limburg, R. Morgenstern, P. Roncin, S. Schippers, R. Schuch, N. Stolterfoht, P. Varga, T. J. M. Zouros, and H. P. Winter. Interaction of slow multicharged ions with solid surfaces. *Surface Science Reports*, 27:113 – 239, 1997.

[70] F. Aumayr. Ion-surface-interaction. `http://www.iap.tuwien.ac.at/www/atomic/surface/index`, 2009.

[71] G.W.F. Drake, editor. *Springer Handbook of Atomic, Molecular and Optical Physics*. Springer New York, 2006.

[72] L. H. Andersen. Dielectronic and radiative recombination with highly charged ions. *Z.Phys. D - Atoms, Molecules and Clusters*, 21:S29–33, 1991.

[73] D.A. Verner and G.J. Ferland. Atomic data for astrophysics. i. radiative recombination rates for H-like, He-like, Li-like, and Na-like ions over a broad range of temperature. *Astrophys. J. Suppl. Ser.*, 103:467, 1996.

[74] P. Mazzotta, G. Mazzitelli, S. Colafrancesco, and N. Vittorio. Ionization balance for optically thin plasmas: Rate coefficients for all atoms and ions of the elements H to Ni. *Astron. Astrophys. Suppl. Ser.*, 133:403–409, 1998.

[75] N. R. Badnell. Radiative recombination data for modeling dynamic finite-density plasmas. *Astrophys. J. Suppl. Ser.*, 167:334–342, 2006.

[76] T.A. Cool. *Recombination, Ionization, and Nonequilibrium Electricial Conductivity in Seeded Plasmas.* PhD thesis, California Institute of Technology, 1965.

[77] Yong-Ki Kim and M. Eugene Rudd. Binary-encounter-dipole model for electron-impact ionization. *Phys. Rev. A*, 50:3954–3967, 1994.

[78] D. Hasselkamp, H. Rothard, K.-O. Groeneveld, J. Kemmeler, P. Varga, and H. Winter, editors. *Particle Induced Electron Emission II*, volume 123 of *Springer Tracts in Modern Physics*, chapter 2, pages 43–60. Springer-Verlag, 1991.

[79] P. Riccardi, P. Barone, A. Bananno, and A. Oliva. Angular studies of potential electron emission in the interaction of slow ions with al surfaces. *Phys. Rev. Lett.*, 84, 2000.

[80] M. Kireeff Covo, A. W. Molvik, A. Friedman, J. J. Barnard, P. A. Seidl, B. G. Logan, D. Baca, and J. L. Vujic. Beam interaction measurements with a retarding field analyzer in a high-current high-vacuum positively charged particle accelerator. *Nucl. Instr. and Meth. in Phys. Res. A*, 577:139–145, 2007.

[81] M. Kireeff Covo, A. W. Molvik, A. Friedman, G. Westenskow, J. J. Barnard, R. Cohen, P. A. Seidl, J. W. Kwan, G. Logan, D. Baca, F. Bieniosek, C. M. Celata, J. L. Vay, and J. L. Vujic. Beam energy scaling of ion-induced electron yield from K^+ impact on stainless steel. *Phys. Rev. ST AB*, 9:063201, 2006.

[82] D. Hasselkamp, H. Rothard, K.-O. Groeneveld, J. Kemmeler, P. Varga, and H. Winter, editors. *Particle Induced Electron Emission II*, volume 123 of *Springer Tracts in Modern Physics*, chapter 1, pages 1–81. Springer-Verlag, 1991.

[83] H. Brenten, H. Müller, K.H. Knorr, D. Kruse, H. Schall, and V. Kempter. The role of Auger processes in slow collisions of Li^+ ions with cesiated W(110) surfaces. *Surf. Sci.*, 243:309 – 316, 1991.

[84] D.B. Williams and C.B. Carter. *Transmission Electron Microscopy A Textbook for Materials Science*. Springer, 1 edition, 2004.

[85] P. H. Stoltz, S. Veitzer, R. Cohen, A. W. Molvik, and J. L. Vay. Simulation of heavy ion induced electron yield at grazing incidence. *Phys. Rev. ST AB*, 7:103201, 2004.

[86] D. A. Dahl. SIMION for the personal computer in reflection. *Int. J. Mass. Spectr.*, 200:3–25, 2000.

[87] R. Baartman. TITAN beamline emittance. private communication, 2008.

[88] C. Böhm and J. Perrin. Retarding-field analyzer for measurements of ion energy distributions and secondary electron emission coefficients in low-pressure radio frequency discharges. *Rev. Sci. Instr.*, 64:31–44, 1993.

[89] I. Langmuir. The effect of space charge and residual gases on thermionic currents in high vacuum. *Phys. Rev.*, 2:450–486, 1913.

[90] M. Dombsky. ISAC yield measurements. `http://www.triumf.info/facility/research_fac/yield.php`.

[91] HeatWave Labs Inc., 195 Aviation Way, Suite 100, Watsonville, CA 95076, USA. *TB-188 Aluminosilicate Ion Sources.* `http://www.cathode.com/pdf/tb-118.pdf`.

[92] J. P. Blewett. Filament sources of positive ions. *Phys. Rev.*, 50:464–468, 1936.

[93] L. R. Dalesioa, J. O. Hilla, M. Kraimerb, S. Lewisc, D. Murray, S. Hunt, W. Watsone, M. Clausenf, and J. Dalesiog. The experimental physics and industrial control system architecture: past, present, and future. *Nucl. Instr. and Meth. in Phys. Res. A*, 352:179–184, 1994.

[94] D. Dale, R. Nussbaumer, T. Howland, H. Hui, R. Keitel, K. Langton, M. Leross, K. Pelzer, J. Richards, W. Roberts, and E. Tikhomolov. The control system for the TITAN experiment at ISAC. In *Proceedings of ICALEPCS07*, 2007. `http://accelconf.web.cern.ch/AccelConf/ica07/PAPERS/TPPB35.PDF`.

[95] S. Halas and T. Durakiewicz. Work functions of elements expressed in terms of the Fermi energy and the density of free electrons. *J. Phys: Condens. Matter*, 10:10815–10826, 1998.

[96] J. F. Ziegler, J. P. Biersack, and M. D. Ziegler. *SRIM: The Stopping and Range of Ions in Matter.* Lulu, 2008.

[97] B.A. Brusilovsky. Kinetic ion-induced electron emission from the surface of random solids. *Appl. Phys. A*, 50:111–129, 1990.

[98] G. Johnson and R. Jennings. *LabVIEW Graphical Programming.* McGraw-Hill Professional, 4 edition, 2007.

[99] OriginLab Corporation, One Roundhouse Plaza, Suite 303, Northampton, MA 01060, USA. *Origin 7.5 User's Manual.* `http://www.originlab.com/pdfs/Origin_V75_Users_Manual.`

`ZIP`.

[100] M. Reiser. *Theory and Design of Charged Particle Beams*. Wiley-VCH, 2008.

[101] T. Schenkel, A. Persaud, A. Kraemer, J. W. McDonald, J. P. Holder, A. V. Hamza, and D. H. Schneider. Extraction of highly charged ions from the electron beam ion trap at LBNL for applications in surface analysis and materials science. *Rev. Sci. Instr.*, 73:663–666, 2002.

[102] F. I. Allen, C. Biedermann, R. Radtke, and G. Fussmann. Extraction of highly charged ions from the Berlin Electron Beam Ion Trap for interactions with a gas target. *Rev. Sci. Instr.*, 77:03B903, 2006.

[103] J. W. McDonald, R. W. Bauer, and D. H. G. Schneider. Extraction of highly charged ions (up to 90+) from a high-energy electron-beam ion trap. *Rev. Sci. Instr.*, 73:30–35, 2002.

[104] B. M. Penetrante, J. N. Bardsley, D. DeWitt, M. Clark, and D. Schneider. Evolution of ion-charge-state distributions in an electron-beam ion trap. *Phys. Rev. A*, 43:4861, 1991.

[105] A. Lapierre, U. D. Jentschura, J. R. Crespo López-Urrutia, J. Braun, G. Brenner, H. Bruhns, D. Fischer, A. J. González Martínez, Z. Harman, W. R. Johnson, C. H. Keitel, V. Mironov, C. J. Osborne, G. Sikler, R. Soria Orts, V. Shabaev, H. Tawara, I. I. Tupitsyn, J. Ullrich, and A. Volotka. Relativistic electron correlation, quantum electrodynamics, and the lifetime of the $1s^22s^22p^2P^o_{3/2}$ level in boronlike argon. *Phys. Rev. Lett.*, 95:183001, 2005.

[106] R. E. Marrs, D. H. Schneider, and J. W. McDonald. Projection x-ray microscope powered by highly charged ions. *Rev. Sci. Instru.*, 69:204, 1998.

[107] P. M. Lapostolle. Possible emittance increase through filamentation due to space charge in continuous beam. *IEEE Trans. Nucl. Sci.*, 18:1101–1104, 1971.

[108] F. J. Sacherer. RMS envelope equations with space charge. *IEEE Trans. Nucl. Sci.*, 18:1105–1107, 1971.

[109] H. Boersch. *Z. Phys.*, 139:115, 1954.